Using the force: Applications and implications of turbulence forcing terms in direct numerical simulations

Thesis by
Chandru Dhandapani

In Partial Fulfillment of the Requirements for the
Degree of
Doctor of Philosophy

CALIFORNIA INSTITUTE OF TECHNOLOGY
Pasadena, California

2019
Defended May 17, 2019

Chandru Dhandapani
ORCID: 0000-0002-7319-557X

ACKNOWLEDGEMENTS

I would like to thank everyone who has helped me in the past five years, while I was working on and writing my thesis. I would like to thank my advisor Guillaume Blanquart for all the scientific discussions, improving my research quality, and helping me negotiate academic life. I want to thank my thesis committee: Dale Pullin, Dan Meiron, and Tim Colonius, for all the productive discussions about my thesis and the constructive feedback. Thanks to my past members of TheFORCE at Caltech: Simon, Bruno, Brock, Jason, and Nick for all helping me learn the ropes in the group, the code, and the research. Thanks to the present members, Jeff, Rachel, Guillaume, and Joe for the helpful conversations. Thanks to all of you for being my Mind stone.

I would like to thank my Power stone, the Resnick Sustainability Institute and Air Force Office of Scientific Research for financially supporting my research. The GALCIT and MCE staff, the graduate office at Caltech, Laura and Daniel at ISP, Caltech Center for Diversity, and the Caltech Counseling Center also helped me tackle graduate student life in general.

I would like to thank my Space stone, my friends from Indian Institute of Technology, Madras, and Caltech community members from the Indian Subcontinent. You helped me teleport to India figuratively, and I always look forward to our road trips and conversations.

Thanks to my Time stone, the Caltech Glee club, Caltech Dhamaka, TACIT, and IMPLICIT, for enabling my extra-curricular escapades, and helping me feel like an undergraduate student again.

Thanks to my Reality stone, my class of GALCIT engineers that joined in 2014 (and its honorary members), my roommates, GSC, CCA, and GHC. Thanks for keeping me grounded in reality.

And finally, thanks to my Soul stone, to my family: my parents, my siblings, my brother-in-law, and my nephew, Linga, for the joy and support they bring to my life, and the unconditional love they shower me with.

With all these stones helping me, I could snap any time and half my problems will dust away.

ABSTRACT

Most energy requirements of modern life can be fulfilled by renewable energy sources, but it is impossible in the near future to provide an alternative energy source to combustion for airplanes. That being said, combustion in aviation can be made more sustainable by using alternative jet fuels, which are made from renewable sources like agricultural wastes, solid wastes, oils, and sugars. These alternative fuels can be used in commercial flights only after a long certification process by the Federal Aviation Agency (FAA) and ASTM International. Unfortunately, in over 50 years of fuel research, only five fuels have been certified. This research project aims to speed up the certification process with quicker testing of alternative fuels. Engine testing and even laboratory testing require large amounts of time and fuel. Simulations can make the process much more efficient, but accurately simulating highly turbulent flames in such complex geometries would need large amounts of computational resources. The goal of this thesis is to create an efficient computational framework, that can replicate different engine-like turbulent flow conditions in simple geometries with numerical tractability.

The central idea is to decompose the flow field into ensemble mean and fluctuating quantities. The simulations then resolve only the fluctuations using simple computational domains, while emulating the effect of the mean flow using "forcing" terms. These forcing terms are calculated first for incompressible turbulence, and this method is later extended to turbulent reacting flows. In incompressible turbulence, Direct Numerical Simulations (DNS) performed on simple triply periodic cubic domains reasonably capture the statistically stationary shear turbulence, that is observed in free shear flows. The simulations are also performed in cuboidal domains, that are longer in one direction and with an inflow/outflow along it. Both changes are observed to not have a significant impact on the turbulence statistics. Finally, shear convection is applied to the turbulence simulations with inflow/outflow, which has a significant impact on the turbulence. These simulations accurately capture the turbulence anisotropy in free-shear flows.

The study is extended to DNS of highly turbulent *n*-heptane-air flames performed under different flow conditions. Turbulent flames involve two-way coupling between fluid mechanics and combustion. The effects of the flame on the turbulence and the impact of the turbulent flow conditions on the flame behavior are analyzed. The focus is placed on the effects of turbulence production, shear convection, and

pressure gradients. The anisotropy produced in the turbulence due to the different flow conditions and the flame are also compared and contrasted. While the global behavior and flow anisotropy were affected by these conditions, the local chemistry effects were unaffected, and depend only on the laminar flame properties and turbulence intensity. These findings can help predict turbulent flame behavior, and can expedite the search and testing of sustainable alternatives to conventional jet fuels.

PUBLISHED CONTENT AND CONTRIBUTIONS

[1] C. Dhandapani, K. J. Rah, and G. Blanquart. “Effective forcing for direct numerical simulations of the shear layer of turbulent free shear flows”. In: *Physical review fluids (accepted for publication)* (2019).
The author of this thesis derived the forcing terms, performed all the simulations, analyzed the data, made the figures, and wrote the manuscript.

TABLE OF CONTENTS

LIST OF ILLUSTRATIONS

Number *Page*

LIST OF TABLES

Chapter 1

INTRODUCTION

1.1 Background

Humanity as a whole has been moving away from fossil-fuels and towards renewable energy sources such as solar, wind, and water energy. These renewable sources of energy can be used for power generation, land transport, heating etc. Electric cars and trains are already in commercial use and electricity generation has been relying less on fossil fuels. In fact, most energy requirements of modern life can be fulfilled by clean energy sources, but not all of them. The high energy density required for air transport can only be met by combustion. In other words, we are "stuck with combustion" for airplanes. The question then becomes can we make combustion in airplanes more sustainable?

Commercial airplanes use petroleum-based jet fuel for combustion, which leads to high CO_2 emissions. Aviation industry accounts for 12% of CO_2 emissions from transportation. As Fig. 1.1 shows, if left unchecked, CO_2 emissions from aviation will be doubled by 2050. Reductions in CO_2 emissions could be made by changes in technology, operation and infrastructure, but that still will not be enough to decrease emissions. The only way to reduce CO_2 emissions to the point of carbon-neutral growth, or even further reduction by 50% of today's quantity is through a change in aviation fuel. Various organizations have recommended alternative jet fuels, that are not only sourced from renewable sources, but also produce lower CO_2 emissions. These alternative fuels could reduce the carbon-footprint of aviation by up to 80% over the full lifecycle (production, refining, transportation and combustion).

Fuels like hydrogen and Compressed Natural Gas (CNG) could be used as alternatives, but these would involve drastic changes in the propulsion system, including new engines, fuel tanks, etc. and raise concerns about cost, safety, operations, efficiency, etc. The shift to alternative fuels would be more economically feasible and impactful if the fuels could be used as "drop-in" fuels, i.e. in the same propulsion system as for conventional jet fuels. Viable alternative jet fuels are ones that behave similar to Aviation Turbine Fuel (ATF) under turbulent combustion in jet engines. Any alternative fuel, regardless of its origin, needs to be certified by the Federal Aviation Administration (FAA) and ASTM International before commercial use. So

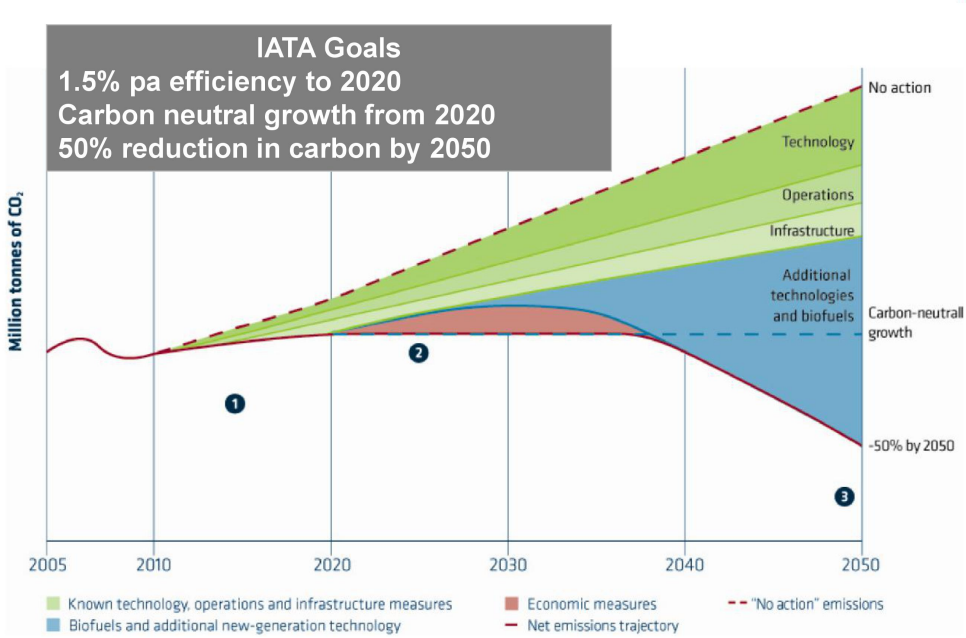

Figure 1.1: CO_2 emissions reduction roadmap of International Air Transport Association (IATA). Major contribution to CO_2 reduction is from alternative fuel technology, and more effective than improvement in Operations, Infrastructure and Technology. Source : International Air Transport Association (IATA)

far, five alternative jet fuels have been approved by the FAA:

1. Alcohol to Jet Synthetic Paraffinic Kerosene (ATJ-SPK) synthesized from alcohols obtained from fermentation of biomass,
2. Synthesized Iso-Paraffins (SIP) produced from sugars,
3. Hydro-processed Esters and Fatty Acids Synthetic Paraffinic Kerosene (HEFA-SPK) made from hydrotreating virgin or waste oils,
4. Fischer-Tropsch Synthetic Paraffinic Kerosene (FT-SPK), and
5. Fischer-Tropsch Synthetic Kerosene with Aromatics (FT-SKA). FT-SPK and FT-SKA are obtained by pyrolysis/gasification and processing of biological wastes.

Alternative jet fuels have been studied since the 1970s. Yet, in almost half a century, only five have been approved. This is a direct result of the long and strenuous certification procedure. The process consists of multiple steps including rig testing and full engine testing, all of which takes a lot of time, effort, fuel, and resources.

The procedure involves testing fuels in engine-scale tests, completely oblivious to the dependence or independence of turbulent combustion on fuel-specific properties. The certification process fails to utilize existing knowledge of turbulent combustion, and the inherent connections between turbulent and laminar flames.

Combustion in engines depends on engine-specific physics and engine-independent characteristics that are common to all turbulent flames. In turn, turbulent flame properties can be further classified into fuel-specific chemistry and fuel-independent properties. Of these fuel-specific properties, engine combustion would only depend on a small subset of laminar flame parameters of the fuel [48]. The goal is to identify these laminar flame properties that significantly affect turbulent flame behavior, and test new fuels for only this small set of parameters to make sure that the alternative fuel behaves like ATF in engines.

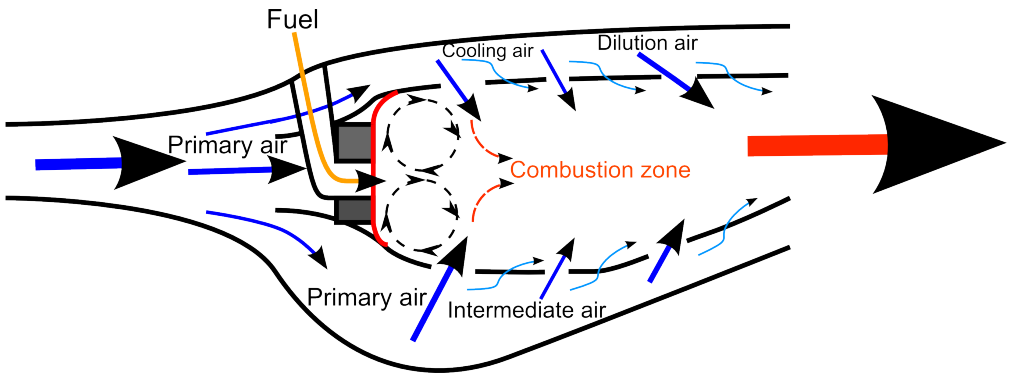

Figure 1.2: Combustion chamber of a turbojet engine

1.2 From engine experiments to direct numerical simulations

Full engine tests: Commercial aircraft engines are either turbojet, turboprop, or turbofan engines, which all contain a compressor stage, a combustion chamber, and a turbine stage in that sequence. The fuel is premixed with compressed air and introduced into the chamber in jets and ignited (see Fig. 1.2). Engine combustion occurs in strongly turbulent conditions, which enhance both mixing and combustion and improve the energy efficiency. These highly turbulent flows can be easily replicated in engine tests, but the tests would consume large amounts of fuel (0.5 to 3 kg/s). Acquiring or processing such large amounts of fuel might not be feasible for alternative jet fuels at the testing/certification stage.

Lab-scale turbulent flame experiments: Multiple researchers have scaled down the turbulent combustion problem and designed experimental setups that mimic

the high shear turbulent combustion found in jet engines (see Fig. 1.3a). These laboratory setups include reacting jets [55, 54, 5, 61], nozzle type burners [46], reacting shear layers [56], turbulent V-flames, swirl burners [6], backwards facing step, jets in cross flow [43], and bluff-body stabilized flames [4]. These experiments use smaller amounts of fuel (0.1 to 1.5 g/s) and are ideal for testing commonly available fuels. Researchers have studied such turbulent flames, with different fuels, over a wide range of equivalence ratios and turbulence intensities. But the fuel requirement may still be too high for potential alternative jet fuels which are not in the phase of mass-production.

Laminar combustion experiments: Aviation turbine fuel and sustainable alternatives to it are all long chain carbon fuels, the combustion of which involves tens of different species and hundreds of elementary chemical reactions. The exact chemical composition and the laminar combustion behavior of the fuel can be easily measured with very small amounts of fuel in simple laboratory settings [33, 39, 42, 83, 91].

Full geometry direct numerical simulations (DNS): Several studies have focused on capturing the entire spatially developing domain of experimental setups. Unfortunately, DNS of the entire domain of a jet engine or an experimental setup are prohibitively expensive. For instance, Yoo *et al.* use around 900 million grid points to simulate a hydrogen-air jet flame (9 species, 21 elementary reactions), at a turbulent Reynolds number of 340 ($Re_J = 11000$) [92, 24]. Hawkes *et al.* [37] performed DNS of temporally evolving plane CO/H_2 jet flames up to $Re_J = 9000$ using 500 million grid points, while Karami *et al.* [44] used 250 million grid points to simulate turbulent lifted slot-jet flame at a Reynolds number of 5280. These are extremely expensive simulations which require a lot of computational resources, and simulating long chain fuels with these methods is not feasible. That is why, researchers have tried to reduce the computational cost by performing flame simulations at lower turbulence intensities [84, 25, 30]. For example, Bell *et al.* use 16 million grid points to study a methane V-flame at a low Reynolds number ($Re_t \simeq 40$) [7], and Sankaran *et al.* use only 93,000 grid points to simulate a methane-air bunsen flame at an even lower Reynolds number ($Re_t \simeq 26$) [74]. Unfortunately, these simulations do not accurately capture the physics of turbulent flame behavior in engines, as turbulent combustion is strongly dependent on Reynolds number.

LES and RANS: Computational costs can also be reduced by performing large eddy simulations (LES) which use coarse grids to capture large scale flow effects [82, 8], and use sub-grid scale models for the unresolved small scales [63, 26, 62]. While these simulations can capture the large scale behavior of the reacting flow with reasonable accuracy, fuel-specific chemical reactions and their interactions with turbulence occur at small scales, that are not fully captured by these simulations [11]. Reynolds Averaged Navier Stokes (RANS) methods work in a similar fashion, where the ensemble mean velocity field is solved for, while the Reynolds stress and scalar flux terms are estimated using different RANS models [12, 87]. Despite recent developments [47, 85], there is still a need for extensive research and higher fidelity in closure models for reacting flows for both LES and RANS.

Small region DNS: Some computational studies cut down on computational domains by performing fully resolved DNS of turbulent flames in simple geometries. However, most of these simulations are not statistically stationary, which is not ideal for steady state observations. For instance, Rutland and Trouve performed simulations of outward propagating flames in triply periodic cubic domains, containing decaying isotropic turbulence [73]. Gruber *et al.* observed turbulent flame-wall interactions in decaying channel flow turbulence [34]. Hamlington *et al.* performed turbulent flame simulations using isotropic turbulence, with the turbulence sustained by introducing random perturbations in the largest scale of the flow. Multiple studies from TheFORCE lab at Caltech have simulated statistically stationary turbulent flames, using linear isotropic forcing to sustain turbulence [75, 76, 49, 9, 48, 79, 78]. The velocity fields in these simulations either contain decaying turbulence, or maintain constant turbulence using artificial numerical methods. This status quo comes from the fact that the large scale flow effects observed in larger domains are missing in such simulations, and one of the effects of the large scale flow is maintaining constant turbulence statistics over time. Ideally, one would like statistically stationary simulations which can accurately reflect the turbulence and can capture the large scale flow effects observed in different experimental setups for turbulent reacting flows.

These observations underline a need for a new framework for simulating turbulent flames which satisfies all the requirements mentioned above. Such method should focus on a small portion of the spatially evolving turbulent reacting flows, and fully resolve all turbulent and chemical scales. While LES/RANS solves for the large-scale/mean flow and introduces models for the small-scales/fluctuations that are not

captured, the targeted method should do the opposite. The small-scales/fluctuations are fully resolved in the simulations, while "forcing" terms are introduced to emulate the impact of the large-scale/mean flow.

These frameworks need to be tested for both incompressible turbulence and turbulent flame simulations.

1.3 Incompressible turbulence

Turbulent free shear flows are found in a multitude of industrial applications and in nature, and their analysis gives a lot of insight into turbulence and its structure. However, owing to the range of scales and the stochastic and unsteady nature of turbulence, even simulating such incompressible flows has proven to be quite challenging. Various configurations have been used to simulate turbulent flows using DNS, that are resolved down to the smallest turbulent length scales. The different DNS methodologies can be broadly classified into three major configurations.

The most obvious configuration is to use the entire domain to solve the spatially evolving flow [86, 10, 88]. In this configuration, the turbulence statistics reach a stationary state after a transient period, and hence the results are ultimately independent from the initial conditions. Unfortunately, the overall flow field depends strongly on the boundary conditions. These simulations typically include a near-field region where the turbulence is not fully developed, and so this configuration is not computationally efficient. Since the entire flow field needs to be solved, these simulations are usually performed at lower Reynolds numbers to reduce the computational costs.

Another configuration is to perform temporally evolving turbulent flow simulations. A perfect example is the mixing layer simulation by Rogers and Moser [70], which introduces homogeneity in the streamwise direction. The extra periodic direction increases the computational efficiency, but does so at the expense of physics. It also aids in calculating the energy spectra, which can be used to observe the different scales of turbulence. Unfortunately, the statistics never reach a stationary state, and hence the results still depend heavily on the initial conditions.

The third configuration is that of a triply periodic domain where the turbulence statistics are homogeneous and there are no boundary conditions to implement because of the triple periodicity. A good example is the numerical simulation of isotropic turbulence by Orszag and Patterson [57]. The computational efficiency is much higher as the flow is fully turbulent throughout. However, in the absence of mean shear, the turbulent kinetic energy in the domain decays over time due to

viscous dissipation [38]. Hence, to keep the turbulent kinetic energy stationary over time, the missing mean shear needs to be emulated through a method of forcing the turbulence. Turbulence in the past has been forced by different techniques, including spectral forcing [28, 32, 17, 23] and linear forcing [53, 72, 20]. While these techniques are required to generate turbulence in the domain, these numerical forcing techniques have been mostly arbitrary, and do not capture the physics of the large scale flows accurately.

Recently, Rah *et al.* [67] combined the numerical tractability of the third configuration with the physical accuracy of the first configuration. They used a triply periodic computational domain, with the forcing calculated from the flow physics at a small region at the centerline of a turbulent round jet, and forced turbulence in a mathematically consistent way. The current study extends this work by considering a small region in the self-similar shear layer of multiple statistically stationary free-shear flows and using a triply periodic computational domain to simulate this shear-dominated flow.

Several homogeneous shear turbulence (HST) simulations have been performed in the literature using similar techniques [69, 31, 50, 14, 41, 45, 80]. While a shear production term was included in each study, considering an idealized homogeneous shear flow, the forcing terms were not derived for practical turbulent flows, and ultimately lacked the mathematical background to be compared to realistic turbulent flows. Most of these simulations used shear periodic boundary conditions, but simulate idealized homogeneous shear flow, and the turbulence statistics grow exponentially in time [31, 50, 14, 41, 45]. Other simulations include a wall boundary in the cross-stream direction, and are not homogeneous [80].

It is also important to remember that these simulations aim to capture the velocity fluctuations observed in statistically stationary free-shear flows. As a consequence, these simulations *need* to have stationary statistics, and be stable enough for simulations over long periods of time.

1.4 From incompressible to flame simulations

Incompressible turbulence simulations can be performed in triply periodic cubic domains, but stationary simulations of turbulent flames cannot be performed in such a configuration. In turbulent flames, the fuel and oxidizer are consumed and combustion products are created constantly. In order to maintain stationary statistics, one needs to constantly introduce more reactants and remove products

from the domain at a steady rate. This can accomplished by foregoing periodic boundary conditions in the flame normal direction, and introducing an inflow on the reactants side and a convective outflow on the side of the products. These boundary conditions create non-homogeneity in the flame-normal direction, and can also have an impact on the flow near the inflow/outflow.

In addition, when introducing an inflow/outflow, the domain width needs to be higher in the direction of the inflow/outflow, so that the boundary conditions do not affect the turbulence statistics in the domain, away from the inlet/outlet. Furthermore, it is desirable for the turbulence to be fully developed before reaching the flame front. Hence, the computational domains for these simulations need to be much longer along one direction. Changing the aspect ratio of the computational domain may affect the simulation results, and these effects need to be studied in detail. As an added benefit, the non-homogeneous direction in the simulation with inflow/outflow allows for studying the effects of shear convection, which is present in free-shear flows of both incompressible and reacting turbulence.

All these impacts need to studied using incompressible flows, before chemistry can be included in the simulations. Once these large scale effects are accurately understood and quantified in incompressible simulations, turbulent flame simulations can be performed using a similar methodology.

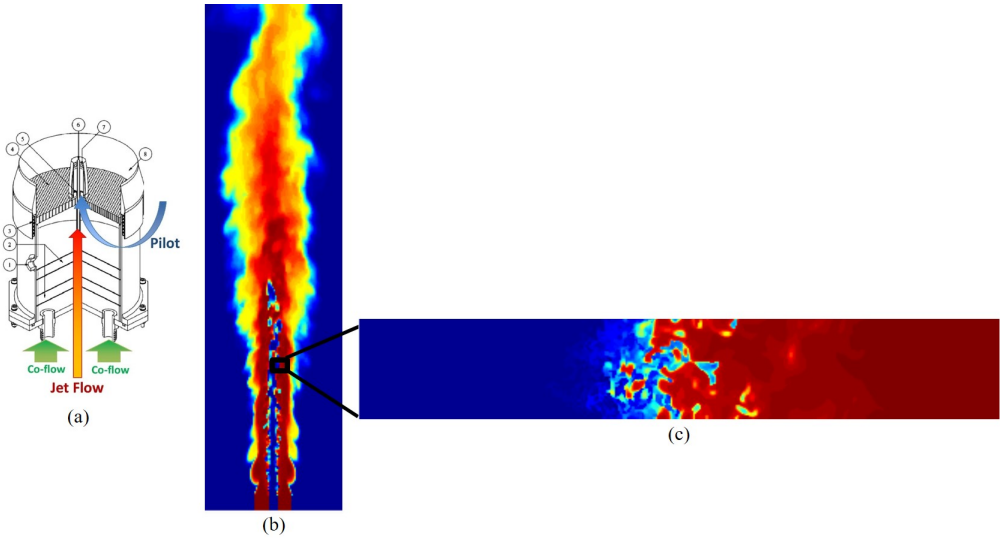

Figure 1.3: a) Experimental setup of a turbulent reacting jet at the CFRL in USC b) LES results of a turbulent reacting jet – Temperature Contours c) DNS results of a turbulent flame – Temperature contours.

1.5 Turbulent flames

One should be careful in extending these turbulence simulation techniques to reacting flames, as turbulent flames involve the complex interaction between two nonlinear processes: turbulence and combustion. The mean flow is affected both by the flow geometry and the chemical reactions. Despite these difficulties, turbulent flame simulations focusing on velocity fluctuations can be found in the literature. Several studies have reduced the computational cost by considering a small region of the turbulent flame and performing DNS with the same turbulence parameters [3, 76, 49, 36]. These simulations consider canonical three-dimensional domains that are often periodic in two directions with the flame progressing along the non-periodic direction, as seen in Fig. 1.3c. This approach offers high-fidelity simulations at low computational costs, and the periodic boundaries help in eliminating boundary condition effects on the simulations.

The disadvantage to these simulations is that the large scale flow effects are not captured. One of the missing effects is the mean shear that generates turbulence, and hence the turbulent kinetic energy decays over time due to viscous dissipation [18, 19]. This is tackled by implementing numerical turbulence forcing in the simulation [36, 2], to keep the turbulent kinetic energy statistically stationary over time.

Several forcing methodologies have been used [36, 2, 64, 75, 49, 76, 72] in past studies. Some turbulence forcing techniques are applied only to low wavenumbers and some are implemented over all scales. Some studies use forcing techniques that are in correlation with the velocity and some forcing methods are not correlated with the velocity field. The forcing term can be applied in spectral space or in physical space, linear with velocity. However, one common factor across all all these numerical forcing schemes is that they have been mostly arbitrary. Most forcing methods generate isotropic turbulence and they do not reflect the flow physics observed in turbulent reacting flows.

The current study aims at mathematically deriving the exact turbulence forcing technique that is physically consistent and compatible with the large scale flow physics and reflects the turbulence observed in turbulent flames. The forcing term comes directly from the turbulence production, that is calculated from the gradients of the large scale velocity. This turbulence production technique will be compared against the isotropic forcing scheme suggested by Lundgren [53].

As mentioned earlier, one main drawback to the small region DNS is that the large

scale flow effects are missing. The turbulence production term is often the source of inspiration for the forcing terms, while the other impacts of the large scale flow can be emulated in the DNS using such similar forcing terms calculated from the large scale flow. The large scale effects like the impact of a mean pressure gradient and shear convection on the turbulent flame behavior are also studied.

Researchers in the past have studied turbulent behavior and their dependence on different factors: fuel type [48], equivalence ratio [48], differential diffusion [49], thermal diffusion [78], turbulence intensity [76, 51], combustion models [79], etc, and most of these studies have been performed with isotropic simulations, with no other large scale effects reflected in the simulations. The impact of the anisotropy of the turbulence and the different flow conditions on the turbulent flame behavior needs to be observed, so one can know if it is reasonable to compare experiments of turbulent flames with different configurations against each other, and against idealized isotropic turbulence simulations.

1.6 Outline

The goal of this thesis is to study the effects of different turbulent flow conditions on the velocity and scalar statistics of turbulent flames. This is achieved by following the research plan given below:

1. Develop a mathematical framework to simulate portions of the incompressible turbulent flow field by using a RANS-inspired velocity decomposition and simulating only the fluctuating quantities.

2. Recreate the statistically stationary shear turbulence observed in free shear flows in homogeneous domains.

3. Extend the simulations to other computational domains to study the impact of aspect ratio, non-homogeneity, and boundary conditions on isotropic and shear turbulence

4. Analyze the effects of shear convection on shear turbulence and its anisotropy.

5. Extend the mathematical framework to variable density flows with chemistry effects and scalar transport.

6. Analyze the impact of the turbulence production term on the global and local flame properties and turbulence statistics.

7. Analyze the impact of favorable pressure gradients and shear convection on the turbulent flames.

The mathematical framework for incompressible turbulence and the simulations in homogeneous cubic domains are presented in Chapter 2. The impact of aspect ratio, non-homogeneity, boundary conditions, and shear convection on incompressible turbulence is analyzed in Chapter 3. Chapter 4 extends the mathematical framework to turbulent flames with variable density. The effects of the turbulence production, favorable pressure gradients, and shear convection on turbulent flames are discussed in Chapter 5. Chapter 6 makes concluding remarks and gives potential directions for future work.

Chapter 2

EFFECTIVE FORCING FOR DIRECT NUMERICAL SIMULATIONS OF THE SHEAR LAYER OF TURBULENT FREE SHEAR FLOWS

[1] C. Dhandapani, K. J. Rah, and G. Blanquart. "Effective forcing for direct numerical simulations of the shear layer of turbulent free shear flows". In: *Physical review fluids (accepted for publication)* (2019).

2.1 Introduction

A numerically efficient configuration to simulate turbulent flows is to use triply periodic domains, with numerical forcing techniques to sustain turbulence. Previous homogeneous shear turbulence simulations considered only idealized homogeneous shear flows, and not the statistically stationary shear turbulence observed in practical free shear flows. In contrast, the current study mathematically derives the complete forcing technique from the large scales of the turbulent free shear flows. Different statistically stationary free shear flows are considered in this study, namely a nearly homogeneous shear turbulent flow, turbulent mixing layer, a turbulent planar jet, and a turbulent round jet. The simulations are performed on triply periodic, statistically homogeneous cubic domains in the vicinity of the shear layer in the self-similar region. An *a priori* analysis is performed to calculate the effects of the different forcing terms and to predict the expected turbulence quantities. The tailored forcing technique is then used to perform direct numerical simulations at different Reynolds numbers. Numerical results for the different cases are discussed, and compared with results from experiments and other simulations of free shear turbulent flows.

In section 2.2, the forcing technique will be mathematically derived, and then calculated, from locations in the shear layers of four different turbulent flows shown in Fig. 2.1. An *a priori* analysis will be performed for the forcing technique in section 2.3 to observe the effects of the different forcing terms. Section 2.4 describes the simulations, and contains a discussion of the numerical results and comparison with experiments and other simulations. Section 2.5 includes additional simulations including linear diagonal terms, non-linear terms, and mean advection terms. Section 2.6 makes concluding remarks about the observations from the study.

2.2 Mathematical derivation

We start by reviewing Lundgren's mathematical approach, which uses a Reynolds decomposition to identify the effects of the large turbulent scales on the small scales. Then, four canonical flows are considered (see Fig. 2.1), and the forcing matrix is calculated for each of them. A forcing technique, common to the self-similar shear layer of these four flows, is discussed after.

2.2.1 Methodology : Review of Lundgren's approach

First, we consider the Navier-Stokes (NS) equations for the velocity field $\boldsymbol{u}$ for a fluid flow with constant density ρ, where p is the pressure and ν is the kinematic viscosity,

$$\frac{\partial \boldsymbol{u}}{\partial t} + \boldsymbol{u} \cdot \nabla \boldsymbol{u} = -\frac{1}{\rho}\nabla p + \nu \nabla^2 \boldsymbol{u}. \tag{2.1}$$

For any turbulent flow phenomenon, the instantaneous velocity field can be decomposed into mean and fluctuating velocity fields (i.e., Reynolds decomposition), $\boldsymbol{u} = \overline{\boldsymbol{u}} + \boldsymbol{u}'$, where $\overline{\cdot}$ represents the ensemble average. Transport equations for the fluctuations are obtained by calculating the difference between the NS equations for the full velocity field and the transport equations for the mean velocity field, namely

$$NS\,(\overline{\boldsymbol{u}} + \boldsymbol{u}') - \overline{NS\,(\overline{\boldsymbol{u}} + \boldsymbol{u}')}. \tag{2.2}$$

This leads to

$$\frac{\partial \boldsymbol{u}'}{\partial t} + (\overline{\boldsymbol{u}} + \boldsymbol{u}') \cdot \nabla \boldsymbol{u}' = -\frac{1}{\rho}\nabla p' + \nu \nabla^2 \boldsymbol{u}' + \nabla \cdot \overline{\boldsymbol{u}'\boldsymbol{u}'} - \boldsymbol{u}' \cdot \nabla \overline{\boldsymbol{u}}. \tag{2.3}$$

The extra terms in the transport equations for the fluctuating velocity, when compared with Eq. (2.1), are the mean-flow advection term ($\overline{\boldsymbol{u}} \cdot \nabla \boldsymbol{u}'$), the divergence of the Reynolds stress term ($\nabla \cdot \overline{\boldsymbol{u}'\boldsymbol{u}'}$), and the production term ($-\boldsymbol{u}' \cdot \nabla \overline{\boldsymbol{u}}$). Lundgren focused on the production term as the only contributor to turbulent kinetic energy production [53], but this is not the case as will be seen later in section C. The major contribution to the turbulent kinetic energy comes from the production term, which is rewritten as a forcing term $\mathbf{A} \cdot \boldsymbol{u}'$,

$$\frac{\partial \boldsymbol{u}'}{\partial t} + \boldsymbol{u}' \cdot \nabla \boldsymbol{u}' = -\frac{1}{\rho}\nabla p' + \nu \nabla^2 \boldsymbol{u}' + \mathbf{A} \cdot \boldsymbol{u}', \tag{2.4}$$

where $\mathbf{A}$ is the forcing matrix, given by $\mathbf{A} = -\nabla \overline{\boldsymbol{u}}$. The source term is linear in $\boldsymbol{u}'$, forces velocity along all scales, and keeps the turbulent kinetic energy from decaying due to viscous dissipation.

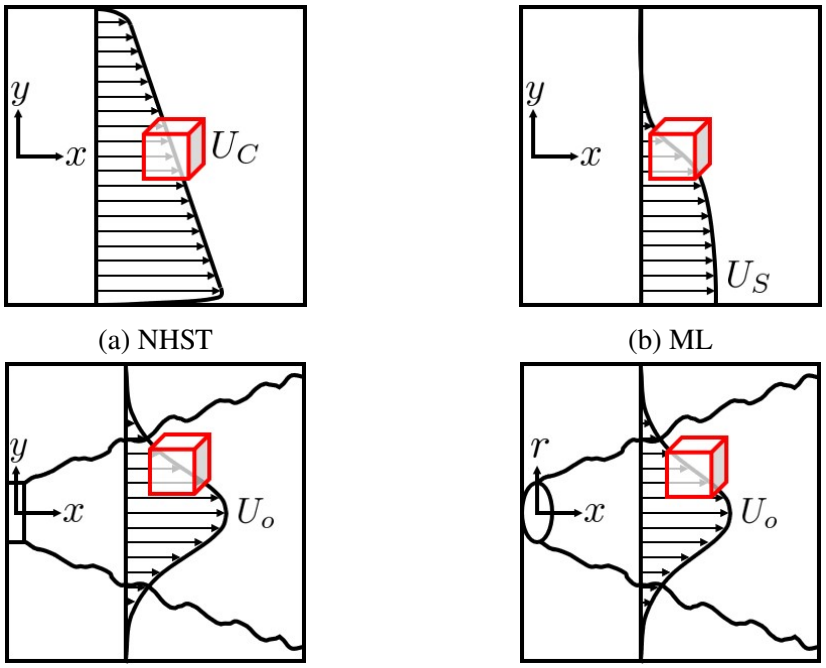

(a) NHST (b) ML

(c) PJ (d) RJ

Figure 2.1: Different turbulent free shear flows considered for the current study with the computational domain chosen (red cube): a) nearly homogeneous shear turbulence (NHST) b) mixing layer (ML) c) planar jet (PJ) d) round jet (RJ).

Lundgren [53] further assumed that the forcing matrix, **A** is a diagonal matrix that generates isotropic turbulence,

$$\mathbf{A}_{\text{Lundgren}} = \begin{bmatrix} A & 0 & 0 \\ 0 & A & 0 \\ 0 & 0 & A \end{bmatrix}. \tag{2.5}$$

This isotropic forcing term was implemented as $A\boldsymbol{u}'$, where A is an arbitrary forcing constant, calculated based on the required turbulent Reynolds number [20]. In practice, the forcing matrix depends on the gradients of the mean velocity.

2.2.2 Mean velocity gradients

Different free shear flows are considered in this study, namely a nearly homogeneous shear turbulence (NHST) flow, a turbulent mixing layer (ML), a turbulent planar jet (PJ), and a turbulent round jet (RJ). The mean velocity gradients can be calculated from the mean velocity profiles obtained from experiments, for each free shear flow. Once again, the intent is to perform simulations on triply periodic, statistically

homogeneous cubic domains in the vicinity of the shear layer in their respective self-similar region as shown in Fig. 2.1.

2.2.2.1 Nearly Homogeneous Shear Turbulence

For a homogeneous shear turbulence flow, the mean flow is in the streamwise direction (x). The free-stream velocity is constant along x and varies linearly in y, away from the walls located at $y = -h/2$ and $y = h/2$. The mean streamwise velocity at the center of the wind tunnel, $y = 0$ is U_C. Far downstream, the quantities are self-similar and are homogeneous in the y direction away from the walls. However, the integral length scale ℓ increases linearly with x [21], and consequently, the Reynolds stresses and the velocity fluctuation magnitudes increase with x, hence the name “nearly" homogeneous shear turbulence. Equation (2.3) for the HST flow in the center of the wind tunnel becomes,

$$\frac{\partial \boldsymbol{u}'}{\partial t} + \boldsymbol{u}' \cdot \nabla \boldsymbol{u}' = -\frac{1}{\rho}\nabla p' + \nu \nabla^2 \boldsymbol{u}' - \frac{\partial \overline{u}_x}{\partial y} u'_y \boldsymbol{e_x} - \overline{u}_x \frac{\partial \boldsymbol{u}'}{\partial x} + \frac{\partial \overline{u'_x u'_x}}{\partial x}\boldsymbol{e_x} + \frac{\partial \overline{u'_x u'_y}}{\partial x}\boldsymbol{e_y}. \quad (2.6)$$

Most simulations of homogeneous shear turbulence use periodic boundary conditions in the x direction without rescaling the velocity, and choose to neglect the divergence of the Reynolds stress terms. The forcing matrix for NHST at $y = 0$ is

$$A_{NHST} = -\begin{bmatrix} 0 & \frac{\partial \overline{u}_x}{\partial y} & 0 \\ 0 & 0 & 0 \\ 0 & 0 & 0 \end{bmatrix} = B_{NHST} \begin{bmatrix} 0 & 1 & 0 \\ 0 & 0 & 0 \\ 0 & 0 & 0 \end{bmatrix}. \quad (2.7)$$

The only element of the forcing matrix is due to the shear strain rate $\frac{\partial \overline{u}_x}{\partial y}$, and the matrix is normalized by that quantity.

2.2.2.2 Mixing Layer

For a spatial mixing layer, the mean flow is primarily in the streamwise direction (x). The freestream velocity is constant along x, and is 0 for $y \to +\infty$ and U_S for $y \to -\infty$. The center of the shear layer is at $y_{1/2}$, where the mean streamwise velocity is $U_S/2$. Far downstream, the mixing layer quantities are self-similar and are only a function of the similarity variable, $\eta \equiv (y - y_{1/2}(x))/\delta(x)$. The mixing layer

thickness δ increases linearly with x, and $y_{1/2}$ is linear in x [22]. There is no mean flow in the spanwise direction ($\overline{u}_z = 0$) and the flow is statistically homogeneous in the spanwise direction ($\frac{\partial \overline{u}_x}{\partial z} = 0$ and $\frac{\partial \overline{u}_y}{\partial z} = 0$).

Equation (2.3) at the center of the mixing layer becomes,

$$\begin{aligned}\frac{\partial \boldsymbol{u}'}{\partial t} + \boldsymbol{u}' \cdot \nabla \boldsymbol{u}' = -\frac{1}{\rho}\nabla p' + \nu \nabla^2 \boldsymbol{u}' - \frac{\partial \overline{u}_x}{\partial x} u'_x \boldsymbol{e_x} \\ - \frac{\partial \overline{u}_x}{\partial y} u'_y \boldsymbol{e_x} - \frac{\partial \overline{u}_y}{\partial x} u'_x \boldsymbol{e_y} - \frac{\partial \overline{u}_y}{\partial y} u'_y \boldsymbol{e_y} - \overline{u}_x \frac{\partial \boldsymbol{u}'}{\partial x} - \overline{u}_y \frac{\partial \boldsymbol{u}'}{\partial y} \\ + \frac{\partial \overline{u'_x u'_x}}{\partial x} \boldsymbol{e_x} + \frac{\partial \overline{u'_x u'_y}}{\partial x} \boldsymbol{e_y}. \quad (2.8)\end{aligned}$$

The forcing matrix for the spatial mixing layer at $y = y_{1/2}$ is

$$A_{ML} = -\begin{bmatrix} \frac{\partial \overline{u}_x}{\partial x} & \frac{\partial \overline{u}_x}{\partial y} & 0 \\ \frac{\partial \overline{u}_y}{\partial x} & \frac{\partial \overline{u}_y}{\partial y} & 0 \\ 0 & 0 & 0 \end{bmatrix} = B_{ML} \begin{bmatrix} -0.035 & 1 & 0 \\ -0.001 & 0.035 & 0 \\ 0 & 0 & 0 \end{bmatrix}, \quad (2.9)$$

calculated from the mean velocity profile given by Lumley [52]. The largest element of the forcing matrix is due to the shear strain rate $\frac{\partial \overline{u}_x}{\partial y}$, and the matrix is normalized by $B_{ML} = -\frac{\partial \overline{u}_x}{\partial y}(y_{1/2}) = 1.022\frac{U_S}{\delta}$.

2.2.2.3 Planar Jet

In a planar jet, the mean flow is primarily in the streamwise direction (x), and the centerline mean velocity at the jet axis, $U_o(x)$, decays along x as $1/\sqrt{x}$ [13, 35, 65, 86]. The mean velocities are self-similar far from the jet exit, and when normalized by the centerline velocity, are only functions of the similarity variable, $\eta \equiv y/y_{1/2}(x)$, where $y_{1/2}$ is the half-width of the jet defined by $\overline{u}_x(x, y_{1/2}(x)) = U_o(x)/2$.

The jet has no mean flow in the spanwise coordinate (z), and no mean gradients along z. The forcing matrix for the planar jet in the middle of the shear layer at $y = y_{1/2}$ is calculated from mean velocity profiles given by Bradbury [13],

$$A_{PJ} = -\begin{bmatrix} \frac{\partial \overline{u}_x}{\partial x} & \frac{\partial \overline{u}_x}{\partial y} & 0 \\ \frac{\partial \overline{u}_y}{\partial x} & \frac{\partial \overline{u}_y}{\partial y} & 0 \\ 0 & 0 & 0 \end{bmatrix} = B_{PJ} \begin{bmatrix} -0.071 & 1 & 0 \\ -0.007 & 0.071 & 0 \\ 0 & 0 & 0 \end{bmatrix}, \quad (2.10)$$

where $B_{PJ} = 0.730\frac{U_o}{y_{1/2}}$. Once again, the largest contribution to the forcing matrix comes from the off-diagonal shear strain term. The forcing matrix is comparable to the mixing layer forcing matrix in Eq. (2.9).

2.2.2.4 Round Jet

For a round jet, Eq. (2.3) is rewritten in cylindrical coordinates for simplicity. The mean flow is primarily in the streamwise direction (x), and the mean centerline velocity $U_o(x)$ has a $1/x$ dependence [15, 59, 1, 10, 40]. We recall the flow is self-similar and the jet quantities, when normalized by the centerline velocity, are only functions of the similarity variable $\eta \equiv r/r_{1/2}(x)$, where $r_{1/2}$ is the half-width of the jet.

There is no mean flow in the azimuthal direction (θ), and no mean gradients along θ. Hence, the forcing matrix for the round jet in the middle of the shear layer at $r = r_{1/2}$ as shown in Fig. 2.1d is calculated from mean velocity profiles taken from Schlichting [77],

$$A_{RJ} = -\begin{bmatrix} \frac{\partial \overline{u}_x}{\partial x} & \frac{\partial \overline{u}_x}{\partial r} & 0 \\ \frac{\partial \overline{u}_r}{\partial x} & \frac{\partial \overline{u}_r}{\partial r} & 0 \\ 0 & 0 & \frac{\overline{u}_r}{r} \end{bmatrix} = B_{RJ}\begin{bmatrix} -0.014 & 1 & 0 \\ -0.001 & 0.037 & 0 \\ 0 & 0 & -0.023 \end{bmatrix}, \tag{2.11}$$

where $B_{RJ} = 0.586\frac{U_o}{r^o_{1/2}}$. Once again, the largest element in the matrix is the off-diagonal shear strain $\frac{\partial \overline{u}_x}{\partial r}$. The matrix is comparable to the velocity gradient matrix for planar jets from Eq. (2.10).

2.2.3 Additional source terms

In addition to the mean velocity gradients, there are source terms that arise from enforcing periodic boundary conditions in the simulation domain [67]. The velocity fluctuations are appropriately normalized to ensure that their second order statistics are homogeneous, so periodic boundary conditions can be used, and these normalizations result in additional source terms. Although these source terms can be calculated for any of the canonical flows mentioned before, the turbulent round jet case is considered for the following calculations, as it has been researched in literature in greater detail.

2.2.3.1 Periodicity in x

As mentioned earlier, in a round jet, the centerline velocity $U_o(x)$ decreases with x as $1/x$. Since the velocity fluctuations are proportional to the centerline velocity, they also decay along x as $1/x$. Under these conditions, the flow is not statistically homogeneous in the x direction, and it would be inappropriate to assume periodic boundaries. To lift this limitation, the velocity fluctuations are rescaled by the $1/x$ dependence as

$$\begin{aligned} u'_x &= u_x^{(x)} \ \frac{x_o}{x} \\ u'_y &= u_y^{(x)} \ \frac{x_o}{x} \\ u'_z &= u_z^{(x)} \ \frac{x_o}{x}, \end{aligned} \tag{2.12}$$

where $\boldsymbol{u}^{(x)}$ is the velocity fluctuation that is statistically homogeneous along x in the vicinity of $x = x_o$. This rescaling produces extra elements in the forcing matrix from the $\overline{\boldsymbol{u}} \cdot \nabla \boldsymbol{u}'$ term. At $x = x_o$, the forcing matrix due to the periodicity correction in x is given by

$$A_x = \begin{bmatrix} \frac{\overline{u}_x}{x_o} & 0 & 0 \\ 0 & \frac{\overline{u}_x}{x_o} & 0 \\ 0 & 0 & \frac{\overline{u}_x}{x_o} \end{bmatrix}. \tag{2.13}$$

2.2.3.2 Periodicity in r

The simulation assumes periodicity along r as well, but the velocity fluctuations depend on the radial distance. In order to maintain statistical homogeneity along r, the velocity fluctuations are rescaled by their individual r dependences.

$$\begin{aligned} u_x^{(x)} &= u_x^{(r)} \ f(\eta) \\ u_r^{(x)} &= u_r^{(r)} \ g(\eta) \\ u_\theta^{(x)} &= u_\theta^{(r)} \ h(\eta), \end{aligned} \tag{2.14}$$

where $\boldsymbol{u}^{(r)}$ is the velocity fluctuation that is statistically homogeneous along r in the vicinity of $r = r^o_{1/2} = r_{1/2}(x_o)$. The forcing matrix due to $\overline{\boldsymbol{u}} \cdot \nabla \boldsymbol{u}'$ applied on Eq. (2.14) is then

$$A_r = \frac{\overline{u}_r - S\overline{u}_x}{r^o_{1/2}} \begin{bmatrix} C_1 & 0 & 0 \\ 0 & C_2 & 0 \\ 0 & 0 & C_3 \end{bmatrix}, \tag{2.15}$$

where $S = dr_{1/2}/dx$ is the spreading rate, $C_1 = -\frac{df}{d\eta}(1)$, $C_2 = -\frac{dg}{d\eta}(1)$ and $C_3 = -\frac{dh}{d\eta}(1)$. From the velocity fluctuations profiles from Hussein *et al.* [40], we have at $r = r_{1/2}$,

$$\begin{aligned} \overline{u}_x &= 0.5U_o \\ \overline{u}_r &= 0.014U_o \\ S &= 0.0935 \\ C_1 &= 0.517 \\ C_2 &= 0.398 \\ C_3 &= 0.345. \end{aligned} \tag{2.16}$$

2.2.3.3 Continuity

The original continuity equation for $\boldsymbol{u}'$ is

$$\frac{\partial u'_x}{\partial x} + \frac{1}{r}\frac{\partial\,(ru'_r)}{\partial r} + \frac{1}{r}\frac{\partial u'_\theta}{\partial \theta} = 0. \tag{2.17}$$

After the normalization in x and r for periodicity (Eqs. (2.12) and (2.14)), the continuity equation for $u^{(r)}$ becomes:

$$\frac{\partial u^{(r)}_x}{\partial x} + \frac{1}{r}\frac{\partial (ru^{(r)}_r)}{\partial r} + \frac{1}{r}\frac{\partial u^{(r)}_\theta}{\partial \theta} = (1 - C_1)\frac{u^{(r)}_x}{x_o} + C_2\frac{u^{(r)}_r}{r_{1/2}}. \tag{2.18}$$

The continuity equation for $\boldsymbol{u}^{(r)}$ has two extra terms. While it is possible to solve the NS equations with additional terms in the continuity equation, it is preferable to have no source terms. That is why $\boldsymbol{u}^{(r)}$ is rewritten in terms of $\boldsymbol{u}''$, under the conditions that $\boldsymbol{u}'' = \boldsymbol{u}^{(r)}$ at $\{x_o, r_{1/2}\}$ and $\boldsymbol{u}''$ is divergence free:

$$\begin{aligned} u^{(r)}_x &= u''_x \exp\left[(1 - C_1)(x/x_o - 1)\right] \\ u^{(r)}_r &= u''_r \exp\left[C_2(r/r^o_{1/2} - 1)\right] \\ u^{(r)}_\theta &= u''_\theta. \end{aligned} \tag{2.19}$$

The forcing matrix due to the continuity correction is

$$A_C = \begin{bmatrix} -\frac{\overline{u}_x}{x_o}(1-C_1) & 0 & 0 \\ 0 & \frac{S\overline{u}_x - \overline{u}_r}{r^o_{1/2}} C_2 & 0 \\ 0 & 0 & 0 \end{bmatrix}. \tag{2.20}$$

The complete transformation from the original velocity fluctuation $\boldsymbol{u'}$ to the statistically homogeneous, divergence-free velocity fluctuation $\boldsymbol{u''}$ is given by

$$\begin{aligned} u'_x &= u''_x \frac{x_o}{x}\ f(\eta)\ \exp\left[(1-C_1)(x/x_o - 1)\right] \\ u'_r &= u''_r \frac{x_o}{x}\ g(\eta)\ \exp\left[C_2(r/r^o_{1/2} - 1)\right] \\ u'_\theta &= u''_\theta \frac{x_o}{x}\ h(\eta), \end{aligned} \tag{2.21}$$

and the transport equation for $\boldsymbol{u''}$ at $\{x_o, r_{1/2}\}$ is calculated as

$$\begin{aligned} \frac{\partial \boldsymbol{u''}}{\partial t} + \boldsymbol{u''}\cdot\nabla\boldsymbol{u''} = -\frac{1}{\rho}\nabla p' + \nu\nabla^2\boldsymbol{u''} + \mathbf{A_{RJ}}\cdot\boldsymbol{u''} - \overline{\boldsymbol{u}}\cdot\nabla\boldsymbol{u''} \\ + \nabla\cdot\overline{\boldsymbol{u''u''}} + \left[\frac{C_1\overline{u_r}}{r^o_{1/2}}u''_x + \frac{C_1}{r^o_{1/2}}\left(u''_x u''_r - \overline{u''_x u''_r}\right)\right]\boldsymbol{e_x} \\ + \left[\frac{\overline{u_x}}{x_o}u''_x + \frac{1}{x_o}\left(u''_x u''_r - \overline{u''_x u''_r}\right)\right]\boldsymbol{e_r} \\ + \left[\frac{\overline{u_x}(1-C_3)}{x_o}u''_x + \frac{1-C_3}{x_o}\left(u''_x u''_\theta - \overline{u''_x u''_\theta}\right)\right]\boldsymbol{e_\theta} \\ + \left[\frac{\overline{u_r}}{r^o_{1/2}}u''_x + \frac{C_3}{r^o_{1/2}}\left(u''_r u''_\theta - \overline{u''_r u''_\theta}\right)\right]\boldsymbol{e_\theta} + \text{visc}, \end{aligned} \tag{2.22}$$

with the gradients of the normal stress in $\nabla\cdot\overline{\boldsymbol{u''u''}}$ being exactly zero, as $\boldsymbol{u''}$ is homogeneous in magnitude. Theoretically, the gradient of the Reynolds shear stress would still exist. However, at $r = r_{1/2}$, the correlation coefficient, $\rho_{xr} = \overline{u'_x u'_r}/\left(\overline{u'_x u'_x}\ \overline{u'_r u'_r}\right)^{1/2}$ is near constant [66], and its gradient is near zero. The additional viscous terms are negligibly small for highly turbulent flows.

The final forcing matrix is calculated as a sum of all of the contributions from

Eqs. (2.11), (2.13), (2.15) and (2.20), and is given by

$$A_F = A_{RJ} + A_x + A_r + A_C \simeq B_{RJ} \begin{bmatrix} -0.039 & 1 & 0 \\ -0.001 & 0.117 & 0 \\ 0 & 0 & 0.038 \end{bmatrix}. \tag{2.23}$$

It is clear that the final forcing matrix is very close to the matrix from Eq. (2.11), with less than 6% difference compared to the largest element. The periodicity in x and r, and the continuity correction do not have significant contributions in the shear layer of a round jet, whereas it had significant effects at the jet axis [67].

2.2.3.4 Non-linear terms

All the source terms in Eq. (2.23) are linear in $\boldsymbol{u''}$; but the transformation from $\boldsymbol{u'}$ to the statistically homogeneous and divergence-free $\boldsymbol{u''}$ in Eq. (2.21) gives rise to some non-linear source terms owing to the term $\boldsymbol{u'} \cdot \nabla \boldsymbol{u'}$, as seen in Eq. (2.22). These non-linear source terms can be written as $A_{NL} \cdot \boldsymbol{u''} - \overline{A_{NL} \cdot \boldsymbol{u''}}$, where A_{NL} is given by

$$A_{NL} = \begin{bmatrix} \frac{C_1}{r^o_{1/2}} u''_r & 0 & 0 \\ 0 & \frac{1-C_2}{x_0} u''_x & 0 \\ 0 & 0 & \frac{1-C_3}{x_0} u''_x + \frac{C_3}{r^o_{1/2}} u''_r \end{bmatrix}. \tag{2.24}$$

These terms have similar magnitudes to the linear source terms from Eqs. (2.13) and (2.15), as $\sqrt{u''^2_x}/\overline{u}_x \simeq 0.48$ and $\sqrt{u''^2_r}/\overline{u}_x \simeq 0.36$.

2.2.4 Summary

The simulation considers the forcing matrix calculated at $\{x, r, \theta\} = \{x_o, r^o_{1/2}, 0\}$, and hence the r-θ direction in the jet coordinates can be replaced by y and z in the Cartesian coordinate system of the DNS. The velocity solved for in the simulation correspond to values at the half-width of the jet, $\{u'_x, u'_r, u'_\theta\}(x_o, r^o_{1/2}, \theta) = \{u''_x, u''_y, u''_z\}$. For simplicity, $\boldsymbol{u''}$ would be represented as $\boldsymbol{u'}$ henceforth.

Some key aspects of this derived forcing must be emphasized. First, the forcing is a direct result of the physics of the free shear turbulent flows considered; the forcing term is not arbitrary, and is derived mathematically from the large scales of the mean

flow. Second, the forcing is not isotropic, which is consistent with results from experiments of free shear flows, where $\langle u_x'^2 \rangle > \langle u_y'^2 \rangle$ [40, 13]. Third, the forcing in this case is not purely from the diagonal terms as suggested by Lundgren's isotropic turbulence, but rather dominated by an off-diagonal shear term.

Comparing with other Homogeneous Shear Turbulence (HST) simulations, where the only production term is $Bu_y'\hat{\boldsymbol{e}}_{\boldsymbol{x}}$, there are additional linear forcing terms on the diagonal due to mean velocity gradients, renormalizations in order to maintain periodicity in the x and y/r directions, and continuity corrections. In addition to the linear diagonal forcing terms, there are also additional forcing terms that are non-linear in $\boldsymbol{u}'$. Finally, the mean advection term is calculated as $-\overline{\boldsymbol{u}} \cdot \nabla \boldsymbol{u}' = By\frac{\partial \boldsymbol{u}'}{\partial x}$, which has been included in past simulations. To avoid confusion with the shear strain (i.e. energy production) term, this term is referred to as shear convection.

2.3 A priori analysis

Multiple source terms have been computed in the previous section. Their effect on the turbulence quantities can be estimated using an *a priori* analysis. Once the most dominant source terms have been selected, the relationship between the source terms and other turbulence quantities can be established.

2.3.1 Contribution of source terms

The effect of all the source terms on the turbulence can be observed from the effects on the turbulent kinetic energy, $k = \frac{1}{2}\langle u_x'^2 + u_y'^2 + u_z'^2 \rangle$ ($\langle \cdot \rangle$ represents ensemble average). The transport equation for the turbulent kinetic energy can be obtained from the velocity fluctuations transport equation as

$$\frac{dk}{dt} = \left\langle u_i' \frac{\partial u_i'}{\partial t} \right\rangle. \tag{2.25}$$

The turbulent kinetic energy equation for the simulation including all the additional linear and non-linear terms and mean advection terms, is given by

$$\frac{dk}{dt} = -\varepsilon + \mathcal{P} + \mathcal{P}_{diag} + \mathcal{P}_{NL} + \mathcal{P}_{conv}, \tag{2.26}$$

where $\varepsilon = 2\nu\langle s_{ij}s_{ij} \rangle$ is the energy dissipation rate. All other terms vanish under statistical homogeneity. The contribution by each of the terms to turbulent kinetic energy production can be calculated and compared with the most dominant shear term $\mathcal{P} = B\langle u_x'u_y' \rangle$. The contribution from the diagonal terms is calculated as,

$$\frac{\mathcal{P}_{diag}}{\mathcal{P}} = \frac{-0.039B\langle u_x'u_x' \rangle + 0.089B\langle u_y'u_y' \rangle + 0.038B\langle u_z'u_z' \rangle}{B\langle u_x'u_y' \rangle}. \tag{2.27}$$

Using Reynolds stress values from the round jet results from Hussein *et al.* [40], $\frac{\mathcal{P}_{diag}}{\mathcal{P}} = 0.117$. The contribution from the non-linear terms can also be calculated as,

$$\frac{\mathcal{P}_{NL}}{\mathcal{P}} = \frac{0.82B\langle u'_x u'_x u'_y\rangle + 0.10B\langle u'_x u'_y u'_y\rangle}{B\langle u'_x u'_y\rangle U_o} + \frac{0.10B\langle u'_x u'_z u'_z\rangle + 0.59B\langle u'_y u'_z u'_z\rangle}{B\langle u'_x u'_y\rangle U_o}. \quad (2.28)$$

Using velocity triple correlation values from the round jet results from Hussein *et al.* [40], $\frac{\mathcal{P}_{NL}}{\mathcal{P}} = 0.209$. The contribution from the shear convection term is computed as

$$\frac{\mathcal{P}_{conv}}{\mathcal{P}} = \frac{B\left\langle y\frac{\partial u'_x}{\partial x}u'_x + y\frac{\partial u'_y}{\partial x}u'_y + y\frac{\partial u'_z}{\partial x}u'_z\right\rangle}{B\langle u'_x u'_y\rangle} = \frac{By\frac{\partial k}{\partial x}}{B\langle u'_x u'_y\rangle}. \quad (2.29)$$

Because of statistical homogeneity in the x direction, $\frac{\mathcal{P}_{conv}}{\mathcal{P}} = 0$. In other words, the advection by the mean term does not contribute to kinetic energy production, as mentioned earlier. Hence, the shear convection terms are not included in the current simulation. Further analyses and justifications are provided in Sections 2.3.3 and 2.5.2.

In summary, the shear strain is the most dominant term, contributing to 75% of the production of turbulent kinetic energy. The linear terms in the diagonal of the forcing matrix and the non-linear terms contribute to 9% and 16% of the production, respectively. Similar results are obtained for mixing layers and planar jets. The off-diagonal shear strain element is at least one order of magnitude larger than the other elements in the matrix and is the major driving force for turbulence production in these aptly named free shear flows, accounting for at least 75% of the turbulent kinetic energy production.

In the current study, for a triply periodic simulation of HST, it is a good approximation to use the off-diagonal shear strain, B, as the only forcing term, with the forcing matrix given by

$$\mathbf{A}_{\mathrm{HST}} = \begin{bmatrix} 0 & B & 0 \\ 0 & 0 & 0 \\ 0 & 0 & 0 \end{bmatrix}, \quad (2.30)$$

where B can be chosen based on the simulation parameters and the desired turbulent Reynolds number. While this term does not inject any external energy, it represents

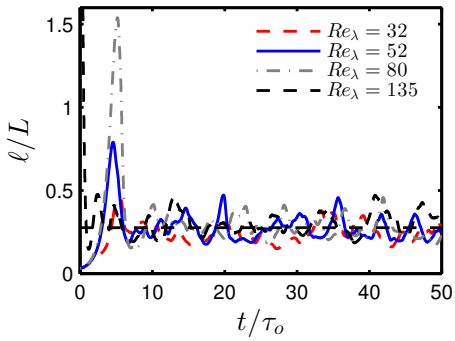

(a) Integral length scale

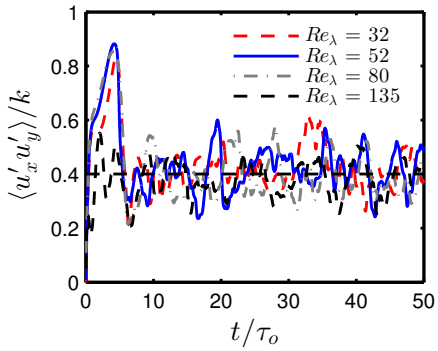

(b) Reynolds shear stress

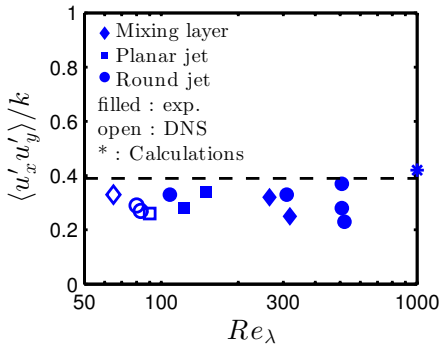

(c) Re_λ dependence

Figure 2.2: a) Integral length scale normalized by the domain width, b) Reynolds shear stress $\langle u'_x u'_y \rangle$ normalized by turbulent kinetic energy, for the four DNS, and c) comparison of Reynolds number dependence of Reynolds shear stress $\langle u'_x u'_y \rangle$ with other studies. Dashed lines corresponds to the averaged value obtained from all simulations in the current study.

the injection of energy into the velocity fluctuations by the mean flow, hence it is an “effective forcing term" in the spirit of Lundgren’s approach, and is henceforth referred to as a forcing term for simplicity. This is similar to conventional simulations of HST, where the off-diagonal shear strain term is the only mechanism for turbulence production [45, 14]. Those studies do not include any of the linear diagonal and non-linear forcing terms; but they include the shear convection term that does not contribute to turbulent kinetic energy.

2.3.2 Stationary state analysis

The entire mathematical framework presented in the previous section relies on the assumption that the velocity field can be decomposed into mean and fluctuating quantities. Then, the simulations in the current study solve for the velocity fluctua-

tions. By construction, these velocity fluctuations represent the fluctuations of the flow field in a small region of a *statistically stationary* turbulent flow. Hence, the fluctuating quantities and their related statistics *must* reach a statistically stationary state. This applies to turbulent kinetic energy, dissipation rate, Reynolds stress, and so on.

Before performing the HST simulations, the target Reynolds number of the simulation needs to be decided, so that the required grid resolution can be evaluated in order to fully resolve down to the smallest turbulent scales. The relationship between the forcing constant B and the Reynolds number needs to be established, in order to calculate the required shear strain, B. The expected eddy turnover time is also calculated from the turbulent kinetic energy and the energy dissipation rate, in order to determine the total simulation time. These expected turbulence quantities are estimated from the stationary state of these simulations.

The turbulent kinetic energy equation for this HST forcing, assuming spatial homogeneity, is

$$\frac{dk}{dt} = -\varepsilon + B\langle u'_x u'_y \rangle. \tag{2.31}$$

At statistically stationary state, the energy dissipation rate is

$$\varepsilon = B\langle u'_x u'_y \rangle. \tag{2.32}$$

This should be compared to the stationary state with the isotropic forcing [20],

$$\varepsilon = 2Ak \tag{2.33}$$

The cross correlation in Eq. (2.32) can be written in terms of the turbulent kinetic energy, $\langle u'_x u'_y \rangle = \beta k$, where β is a non-dimensional parameter.

The integral length scale, ℓ, is defined as,

$$\ell = \frac{u_{rms}^3}{\varepsilon} = \frac{2u_{rms}}{3\beta B}, \tag{2.34}$$

with

$$u_{rms} = \sqrt{\frac{2k}{3}} = \frac{3}{2}\beta B \ell. \tag{2.35}$$

The Taylor micro-scale, λ, is calculated as

$$\lambda = \sqrt{15\frac{\nu}{\varepsilon}} u_{rms}. \tag{2.36}$$

The expected Taylor micro-scale Reynolds number for HST is calculated as

$$Re_\lambda^o = \sqrt{\frac{45\beta B\ell^2}{2\nu}}. \tag{2.37}$$

For isotropic turbulence simulations, it was given by Carroll and Blanquart [20],

$$Re_\lambda^o = \sqrt{\frac{45A\ell^2}{\nu}} \simeq \sqrt{\frac{9AL^2}{5\nu}}, \tag{2.38}$$

as $\ell/L \simeq 0.2$ for isotropic turbulence in a triply periodic box domain [72, 20], where L is the domain width. As will be shown from numerical results in Fig. 2.2a and 2.2b, $\beta \simeq 0.4$ and $\ell/L \simeq 0.28$ for HST. So, given the same domain width and viscosity, DNS of HST can be performed with the same Reynolds number as DNS of homogeneous isotropic turbulence, using the forcing constant $B \simeq 3.2A$.

The expected values for turbulent kinetic energy, k_o, and energy dissipation rate, ε_o, can be calculated as

$$k_o = \frac{3}{2}u_{rms}^2 = \frac{27}{8}\beta^2 B^2 \ell^2, \tag{2.39}$$

and

$$\varepsilon_o = \frac{u_{rms}^3}{\ell} = \frac{27}{8}\beta^3 B^3 \ell^2. \tag{2.40}$$

The expected eddy turnover time τ_o is given by

$$\tau_o = \frac{k_o}{\varepsilon_o} = \frac{1}{\beta B} \simeq \frac{25}{32A}, \tag{2.41}$$

which is slightly higher than for the isotropic case, where $\tau_o = \frac{1}{2A}$ [20].

2.3.3 Shear convection

The proposed HST simulation has a key difference from most simulations of shear turbulence [14, 45, 41, 50]; it does not include the shear convection term $By\frac{\partial \boldsymbol{u'}}{\partial x}$. The shear convection term requires either a remeshing scheme after every few iterations [68] or implementing shear periodicity along the y direction to avoid boundary discontinuities [14, 41, 45]. It is often accomplished by using operator splitting [45, 31], which may introduce further errors in the computational solution.

As mentioned earlier, the shear convection term does not contribute to turbulent kinetic energy production (see section 2.3.1), as $\mathcal{P}_{conv} = \langle By\frac{\partial \boldsymbol{u'}}{\partial x} \cdot \boldsymbol{u'} \rangle = 0$ due to spatial homogeneity. That being said, it may still impact the turbulent flow. To quantify this impact, we evaluate the shear strain produced by the advection term and compare it to the existing shear strain due to the turbulence. The shear strain

Table 2.1: Simulation parameters of the different cases of shear turbulence simulations

No	Re_λ^o	N^3	L	ν	B	Forcing Matrix	Re_λ
1	36	64^3	2π	0.159	7.33	A_{HST}	32 ± 6
2	54	128^3	2π	0.159	16.5	A_{HST}	52 ± 9
3	80	192^3	2π	0.159	37.1	A_{HST}	80 ± 13
3a	80	192^3	2π	0.159	37.1	A_F	80 ± 15
3b	80	192^3	2π	0.159	37.1	$A_F + A_{NL}$	80 ± 13
3c	80	192^3	2π	1) 0.159 2) -0.0159	37.1	A_{HST}	121 ± 20
3d	80	192^3	2π	0.1431	37.1	A_{HST}	85 ± 10
4	128	384^3	0.126	$1.5e^{-5}$	2.77	A_{HST}	135 ± 23

due to the convection term can be calculated as $\frac{\partial \overline{u}_x}{\partial y} = B$ and compared against the existing shear strain due to the turbulence, $\frac{\partial u_x'}{\partial y}$. Since $\left\langle \frac{\partial u_x'}{\partial y} \right\rangle = 0$, the second order statistics are compared as,

$$\frac{B^2}{\left\langle \left(\frac{\partial u_x'}{\partial y} \right)^2 \right\rangle} = \frac{\frac{15\nu}{2} B^2}{\frac{15\nu}{2} \left\langle \left(\frac{\partial u_x'}{\partial y} \right)^2 \right\rangle} \simeq \frac{15\nu B^2}{2\varepsilon} = \frac{50}{\beta^2 Re_\lambda^2}, \tag{2.42}$$

with the isotropic assumption that $\varepsilon \simeq \frac{15\nu}{2} \left\langle \left(\frac{\partial u_x'}{\partial y} \right)^2 \right\rangle$. For $Re_\lambda = 100$, the ratio is 0.031. Hence, the impact of the shear convection term is small, and decreases with increasing Reynolds number. Thus, the shear convection term is omitted for true spatial homogeneity and numerical efficiency. Its impact will be discussed in Section 2.5.2.

2.4 Numerical results

2.4.1 Simulation

Direct numerical simulations of homogeneous shear turbulence are performed in a triply periodic box domain that is statistically homogeneous in all three directions. Simulations are performed with a domain width of $L = 2\pi$, and various Reynolds numbers Re_λ.

The simulations are performed using NGA [27], a semi-implicit velocity solver with an energy-conserving finite difference scheme on a standard staggered grid. The code solves the Navier-Stokes equations with the derived source term from Eq. (2.30) for constant density, temperature, and viscosity.

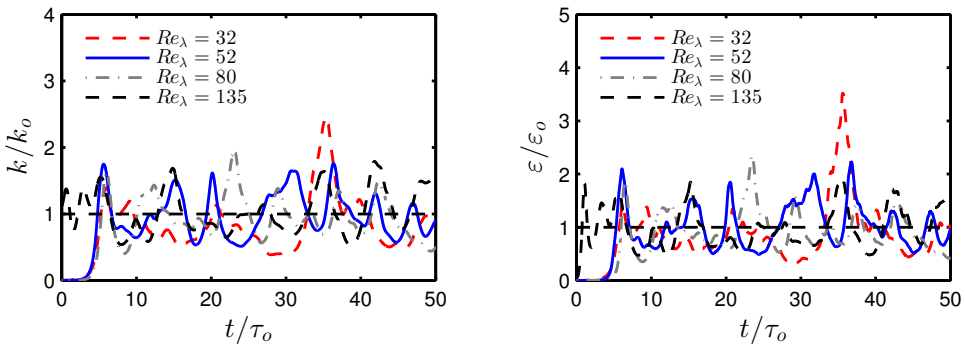

(a) Turbulent kinetic energy

(b) Energy dissipation rate

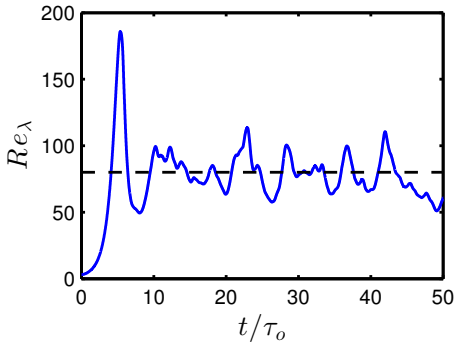

(c) Reynolds number

Figure 2.3: a) Turbulent kinetic energy normalized by its expected value (Eq. 2.39). b) Energy dissipation rate normalized by its expected value (Eq. 2.40). c) Taylor microscale Reynolds number, Re_λ, for DNS 3. Dashed line corresponds to $Re^o_\lambda = 80$.

The initial velocity fields are generated randomly, using the method suggested by Eswaran and Pope [28]. These velocity fields conform to a specified Passot-Pouquet energy spectrum [60] and are divergence free, as is required for constant density flows.

Multiple simulations are performed at different expected values of Re_λ. The simulation parameters for the four different cases are tabulated in Table 2.1. Cases 1 and 2 were performed to investigate low Reynolds number effects, if any. Cases 3 and 4 are chosen so the Reynolds number is comparable to simulations and experiments, published in literature (See Table 2.3 for a full list of experimental and full domain DNS studies). More precisely, case 3 has a similar Reynolds number to cases 1 [70], 4 [86] and 8 [10] from Table 2.3; case 4 has a Reynolds number close to cases 5 [35] and 9 [88] in Table 2.3.

The simulations were performed for a total of 50 eddy turnover times, during which

Table 2.2: Results from shear turbulence simulations in triply periodic cubic simulations

No	Re^o_λ	Re_λ	u'_x/u_{rms}	u'_y/u_{rms}	u'_z/u_{rms}	$\langle u'_x u'_y \rangle/k$	ℓ/L
1	36	32 ± 6	1.26	0.90	0.77	0.42	0.24
2	54	52 ± 9	1.23	0.93	0.78	0.41	0.27
3	80	80 ± 13	1.23	0.92	0.78	0.39	0.28
3a	80	80 ± 15	1.21	0.94	0.79	0.39	0.27
3b	80	80 ± 13	1.20	0.95	0.80	0.38	0.26
3c	80	121 ± 20	1.23	0.93	0.79	0.37	-
3d	80	85 ± 10	1.23	0.94	0.78	0.39	0.29
4	128	135 ± 23	1.22	0.93	0.80	0.38	0.31

the simulations were stable. The average values for the numerical results were calculated in the range, $10\tau_o$ to $50\tau_o$.

2.4.2 Temporal evolution

Since the configuration is periodic in all three directions, and spatially homogeneous, ensemble averaged mean quantities are calculated as spatial averages ($\langle \cdot \rangle$). These spatial averages are plotted as a function of time.

The time evolution of the integral length scale is plotted in Fig. 2.2a, and after an initial transient period of at most $10\tau_o$ gives a mean value of about $0.28L$, which is slightly higher than the $0.2L$ for isotropic turbulence observed by Rosales and Meneveau [72]. The integral length scale reaching a statistically stationary value of the order of the domain width is consistent with past simulations of statistically stationary homogeneous shear turbulence [81].

Since the largest gradient of the mean flow is the shear strain $\frac{\partial \overline{u}_x}{\partial y}$, the only significant Reynolds stress term is $\langle u'_x u'_y \rangle$. This is reflected by the simulation, as the forcing term is in the equation for the axial velocity (u'_x), proportional to the cross-stream velocity (u'_y). So, it is expected that u'_x and u'_y have a significant positive correlation. This is one of the major differences between HIT and HST, as there is no correlation among the velocities in different directions for the isotropic case. Figure 2.2b shows the $\langle u'_x u'_y \rangle$ values normalized by k at different Re_λ. It can be seen that after $5\tau_o$, the values fluctuate around 0.4 for all cases, in good agreement with each other.

The average value of Reynolds shear stress from all simulations of the current study is also plotted in Fig. 2.2c and compared with values from various simulations

Table 2.3: Anisotropy results from various experiments and simulations of different free shear turbulent flows. Average values of u_i'/u_{rms} and $\langle u_x' u_y' \rangle / k$ in the middle of shear layers of ML (mixing layers), PJ (planar jets), and RJ (round jets). S corresponds to simulations, E corresponds to experiments, C corresponds to calculations.

No	Case	Re_λ	u_x'/u_{rms}	u_y'/u_{rms}	u_z'/u_{rms}	$\langle u_x' u_y' \rangle / k$
1	MLS [70]	60–69	1.10	0.88	1.01	0.33
2	MLE [58]	155	1.15	0.93	0.91	0.32
3	MLE [89]	186	1.13	0.88	0.97	0.25
4	PJS [86]	89–92	1.05	1.02	0.92	0.26
5	PJE [35]	122	1.33	0.75	0.81	0.28
6	PJE [13]	148–154	1.15	0.93	0.90	0.34
7	PJC [65]	–[1]	1.28	0.85	0.81	0.42
8	RJS [10]	80	1.21	0.84	0.92	0.29
9	RJS [88]	113	1.21	0.90	0.85	0.27
10	RJE [59]	172	1.23	0.86	0.86	0.33
11	RJE [29]	232	1.21	0.88	0.88	–
12	RJE [16]	309	1.29	0.82	0.82	0.33
13	RJE [40]	508	1.17	0.88	0.92	0.28
			1.20	0.84	0.92	0.37
14	RJE [90]	520	1.22	0.86	0.88	0.23

[1] Planar jet calculations were performed by Pope using a Monte Carlo method to solve the joint pdf equation. These results correspond to the high Reynolds number limit, and are plotted at $Re_\lambda = 1000$ in Fig. 2.2c and 2.4b. These values agree very well with results from the current study.

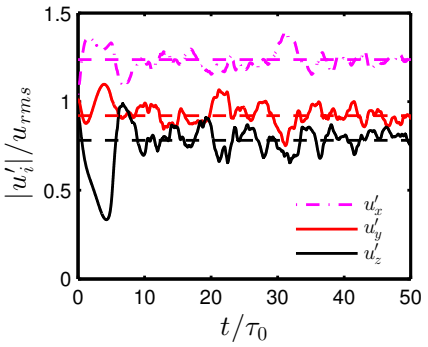

(a) Anisotropy in velocity

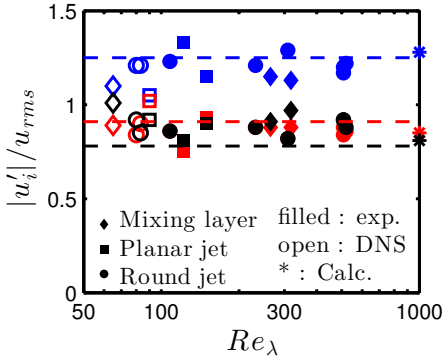

(b) Re_λ dependence of anisotropy

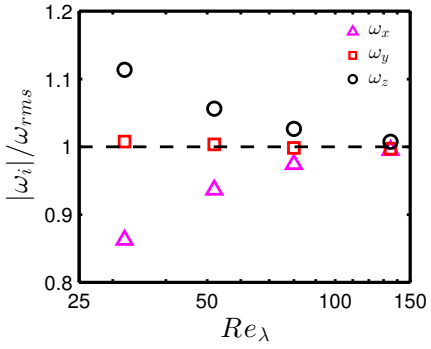

(c) Anisotropy in vorticity

Figure 2.4: a) Rms velocity components along x, y, and z, normalized by u_{rms}, for DNS 3. (Re_λ^o = 80) b) Mean values for velocity fluctuations normalized by u_{rms} from other studies plotted versus Re_λ. Dashed lines correspond to the averaged values from the current simulations (1.24, 0.92, and 0.78 respectively). c) Average values of rms vorticity components along different directions normalized by ω_{rms} plotted versus Re_λ. Dashed line corresponds to isotropic turbulence.

and experiments plotted as a function of Reynolds number. The current study overpredicts the Reynolds shear stress, by about $1.5\,\sigma$ compared to values from other studies, and there seems to be no clear dependence on Re_λ.

The turbulent kinetic energy and energy dissipation rate, normalized by their respective expected values calculated from Eq. (2.39) and (2.40), are plotted versus time for the different cases in Fig. 2.3. The values fluctuate around the expected values, so the estimation of k_o and ε_o are accurate. The fluctuations increase in magnitude with increasing Reynolds number. This is expected, as linear forcing becomes more unstable with higher Reynolds number, as observed by Carroll and Blanquart [20], who used a modification to the linear forcing term to improve stability. In contrast, the current forcing term uses constant mean shear, as opposed to

the constant production forcing used by Carroll and Blanquart [20].

Figure 2.3c shows the Reynolds number, based on Taylor micro-scale, versus time for case 3, and it can be observed that Re_λ fluctuates around the expected value (80, in this case) after a transient period of about $5\tau_o$.

2.4.3 Directional anisotropy

Second-order statistics can be analyzed to gather information about the velocity fluctuations and consequently about the turbulence. The magnitudes of the velocity fluctuation components ($|u'_x|$, $|u'_y|$, and $|u'_z|$) are calculated from the root mean square (rms) of the fluctuating velocity components (e.g., $|u'_i| = \sqrt{\langle u'^2_i \rangle}$). Because of the anisotropic nature of free shear flows, it is expected that the velocity fluctuations will be larger in magnitude along the axial direction. This is corroborated by other simulations and experiments in Table 2.3, and is reflected in the forcing. Although the forcing is only along the axial direction, turbulence redistributes some of the fluctuations to the other directions, while maintaining higher fluctuations in the axial direction.

Figure 2.4a plots the velocity fluctuation components along the x, y, and z directions normalized by u_{rms} for $Re^o_\lambda = 80$. For isotropic turbulence, velocity fluctuations are expected to be similar along all directions, and hence $|u'_i|/u_{rms} \simeq 1$. For HST, as expected, the axial direction has the largest fluctuations, and the cross-stream direction and spanwise direction have smaller fluctuations. The results follow the same trend for all Reynolds numbers considered. The average values from the four cases of our current study are $|u'_x|/u_{rms} \simeq 1.25$, $|u'_y|/u_{rms} \simeq 0.91$ and $|u'_z|/u_{rms} \simeq 0.78$.

The average values of rms velocity components are plotted in Fig. 2.4b, along with data from multiple simulations and experiments of mixing layers, planar jets, and round jets, plotted versus Reynolds number. The current simulation solves for $\boldsymbol{u}''$, and from Eq. (2.21), $\boldsymbol{u}'' = \boldsymbol{u}'$ at $x_o, r^o_{1/2}$. Therefore, the spatially-averaged results of the current study can be compared against temporally-averaged values in the middle of shear layers. All of the free shear flows seem to agree well with each other. The results from the current study agree reasonably well with the values from literature within 1 σ, except for $|u'_z|/u_{rms}$, where the current study underpredicts the values, by 2 σ. Also, there seem to be no Reynolds number effects on the velocity fluctuation magnitudes, as the values remain constant across a large range of Re_λ.

The anisotropy in the smallest turbulent length scales can be observed using the

root mean square of the vorticity components ($|\omega_x| = \sqrt{\langle\omega_x^2\rangle}$, etc), normalized by the rms vorticity, $\omega_{rms} = \sqrt{\langle\boldsymbol{\omega}\cdot\boldsymbol{\omega}\rangle/3}$. Kolmogorov suggested that at very high Reynolds number, the turbulence is isotropic at the smallest turbulent length scales and hence, the vorticity would be statistically isotropic with $|\omega_i| \simeq \omega_{rms}$. As shown in Fig. 2.4c and as expected, the averaged vorticity magnitudes reach isotropic values with increasing Reynolds numbers.

2.4.4 Energy spectrum

The one dimensional energy spectra for the velocity are calculated from the simulation results of DNS 1-4. Leveraging the flow homogeneity, energy spectra are calculated using one-dimensional Fourier transforms in the x direction, $(\mathcal{F}_1(\boldsymbol{u}))$ in space at different times during the simulations, $E(\kappa_1) = \mathcal{F}_1(\boldsymbol{u})\cdot(\mathcal{F}_1(\boldsymbol{u}))^*$ versus the wavenumber in the x direction, κ_1, where $\cdot^*$ represents the complex conjugate. The final spectrum plotted in Fig. 2.6a is calculated as the mean of the spectra from all data files from $10\tau_o$ to $50\tau_o$, at time intervals of $0.5\tau_o$ for data independence. Figure 2.6a shows the energy spectra of all the four simulations. The spectra are normalized by the Kolmogorov length and velocity scales and show a collapse at all wavenumbers. The four spectra follow well the $\kappa_1^{-5/3}$ spectrum expected from turbulence simulations.

As mentioned earlier, the conditions of DNS 4 were selected to match the DNS of Rogers and Moser [70]. Rogers and Moser performed a simulation of a temporally-evolving mixing layer using a Galerkin spectral method with $512\times210\times192$ Fourier modes. They reported one-dimensional energy spectra in x_1 (streamwise) and x_3 (spanwise) calculated at a Reynolds number of $Re_m \simeq 2000$. The one-dimensional spectra, $E(\kappa_1)$ and $E(\kappa_3)$, are calculated for DNS 4 and plotted in Fig. 2.5, where $E(\kappa_3) = \mathcal{F}_3(\boldsymbol{u})\cdot(\mathcal{F}_3(\boldsymbol{u}))^*$, where $\mathcal{F}_3(\boldsymbol{u})$ is the one dimensional Fourier transform of the velocity in the z direction. The one-dimensional spectra, $E(\kappa_1)$ and $E(\kappa_3)$, follow that $\int E(\kappa_i)d\kappa_i = \langle u_x'^2 + u_y'^2 + u_z'^2\rangle = 2k,\ i = 1,3$ and are plotted versus wavenumber in the two directions κ_1 and κ_3. It is seen that $E(\kappa_1)$ and $E(\kappa_3)$ are nearly indistinguishable, and these plots agree well with the spectra from Rogers and Moser [70]. Note that the ranges of wavenumbers are different between the two simulations, because of different domain sizes and resolutions. This spectral analysis shows that the simulations reproduce shear-driven turbulence in the spectral sense as well.

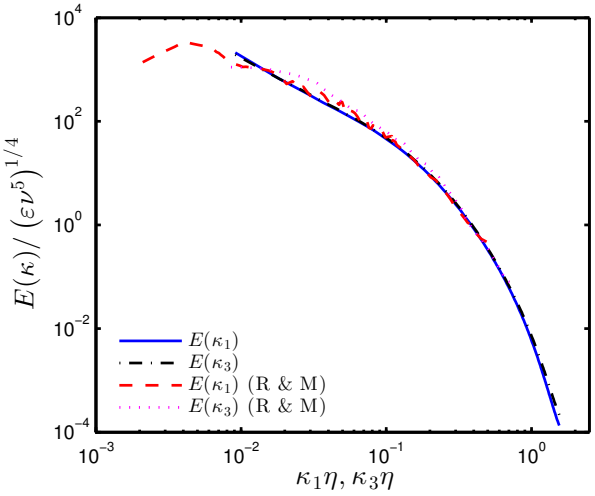

Figure 2.5: Comparison of one-dimensional energy spectra along x and z directions. R & M refers to the energy spectra published by Rogers and Moser [70].

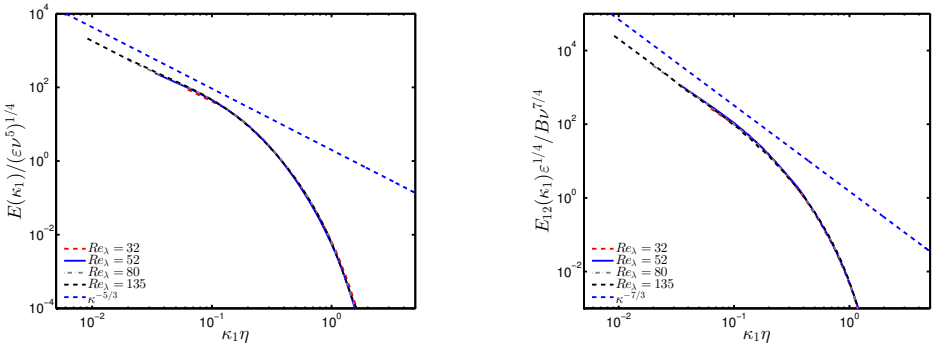

(a) Energy spectra

(b) Shear stress spectra

Figure 2.6: a) Energy spectra normalized by ε and ν. b) Shear stress spectra normalized by ε and ν. The dashed line corresponds to turbulence scaling from literature, $\kappa^{-5/3}$ in a) and $\kappa^{-7/3}$ in b).

2.4.5 Production spectrum

Finally, the one-dimensional spectra for the turbulent kinetic energy production are calculated from the shear stress spectra. The shear stress spectrum, $E_{12}(\kappa_1)$ is calculated from the same data files as the energy spectrum, as

$$E_{12}(\kappa_1) = 0.5\left[\mathcal{F}_1(u_x)\cdot\left(\mathcal{F}_1(u_y)\right)^* + \mathcal{F}_1(u_y)\cdot\left(\mathcal{F}_1(u_x)\right)^*\right]$$

such that $\int E_{12}(\kappa_1)d\kappa_1 = \langle u_x' u_y' \rangle$. The production spectra are plotted versus wavenumber in Fig. 2.6b. The wavenumber and the spectra are normalized with B

and Kolmogorov length and velocity scales, $u_\eta = (\nu\varepsilon)^{1/4}$, and the spectra show a collapse at all wavenumbers.

It is seen that the production spectra scale as $\kappa_1^{-7/3}$ as suggested by Lumley [52]. The production spectra decay faster than the energy spectra, which scale like $\kappa_1^{-5/3}$. Hence the production to energy ratio is higher in the large scales, and gets smaller approaching the small scales. In contrast, linear isotropic turbulence forces velocity proportional to the energy among all scales [53, 20] and most spectral techniques only force velocity over a low wavenumber bandwidth [28, 32, 17, 23].

2.5 Additional considerations

As mentioned earlier, all of these simulations were performed with a single off-diagonal forcing term. However, the additional diagonal terms from the velocity gradients and the diagonal and non-linear terms from the periodicity and continuity corrections can also be included in the simulation as forcing terms. The impact of these additional forcing terms are analyzed by comparing the simulations with and without them.

2.5.1 Linear diagonal and non-linear source terms

Simulation 3 was repeated as DNS 3a with all the linear diagonal terms from Eq. (2.23) and as DNS 3b with all linear and non-linear terms from Eq. (2.24). This second simulation is the closest representation to the half-width of the turbulent round jet.

2.5.1.1 Anisotropy and energy production

DNS 3a gives an average value of $\langle u'_x u'_y \rangle = 0.39$ and DNS 3b gives an average value of $\langle u'_x u'_y \rangle = 0.38$, which are both very close to the results from DNS 3. The diagonal terms only contribute to about 7% of the turbulent kinetic energy production, and the non-linear terms are responsible for 12% of it in DNS 3b. These results are slightly less than our *a priori* estimate of the contributions (see section 2.3.1). The off-diagonal term is the major contributor to the production, accounting for 93% and 81% of the kinetic energy production in DNS 3a and 3b respectively.

2.5.1.2 Turbulent kinetic energy budget

The various terms in the budget of the turbulent kinetic energy, namely the production, advection, turbulent diffusion, and the dissipation, are calculated and compared

against the turbulent kinetic energy budget for the turbulent round jet. The current simulations correspond to the location of the half-width of the round jet, and should be compared against the experimental values at $r = r_{1/2}$.

The budget values are plotted in Fig. 2.7 and compared with the experiment results of Panchapakesan and Lumley [59]. The forcing matrix from the velocity gradients corresponds to production, $Prod = \langle \boldsymbol{u'} \cdot \nabla \overline{\boldsymbol{u}} \cdot \boldsymbol{u'} \rangle = \langle \boldsymbol{u'} \cdot A_G \cdot \boldsymbol{u'} \rangle$; the diagonal elements of the forcing matrix from the renormalization matrices A_x and A_r correspond to advection, $Adv = \overline{\boldsymbol{u}} \cdot \nabla k = \langle \boldsymbol{u'} \cdot A_x \cdot \boldsymbol{u'} \rangle + \langle \boldsymbol{u'} \cdot A_r \cdot \boldsymbol{u'} \rangle$; and the turbulent diffusion can be calculated from the triple correlation, $Diff = \nabla \cdot \langle \boldsymbol{u'} k \rangle = \langle k u'_y \rangle / r_{1/2} + 3 \langle k u'_x \rangle / x_o$. The dissipation rate is calculated as $Diss = -\varepsilon$. These quantities are calculated from the three simulations, regardless of what the forcing matrix is. All the values are normalized by $U_o^3 / r_{1/2}$, where U_o is calculated as $U_o = \sqrt{k/0.062}$ [40] and $r_{1/2}$ is calculated as $r_{1/2} = 0.586 U_o / B$ [77].

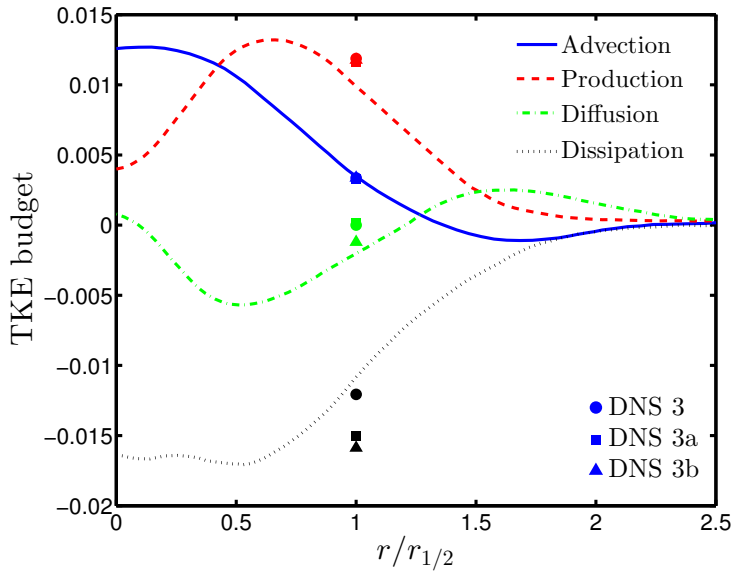

Figure 2.7: Normalized turbulent kinetic energy budget. The lines correspond to experimental results from Panchapakesan and Lumley [59]. Symbols correspond to different simulations: DNS3 - circles, DNS 3a - triangles, DNS 3b - squares.

As expected, the major contributions to the budget are from production and dissipation, and the advection and diffusion are closer to zero. The advection by the mean is accurately represented by the simulation, whereas the production and dissipation are slightly over-predicted. This result is consistent with the over-prediction of the shear Reynolds stress $\langle u'_x u'_y \rangle$ (see Fig. 2.2c), and the dissipation increasing to match the

turbulent kinetic energy production. The diffusion value of case 3b matches fairly well with the experimental results, as they include non-linear source terms which appear as diffusion terms (triple correlations) in the kinetic energy budget, while case 3 and 3a show zero diffusion. Apart from this, there are very small differences between the simulations without the diagonal terms (case 3), with the diagonal terms (case 3a), and with the non-linear terms (case 3b). In fact, the dissipation values from DNS 3 are closer to the experimental results. Hence, adding the additional source terms do not make any improvement in the turbulent kinetic energy budget, except in the turbulent diffusion.

The simulations involve a balance between the two major contributors, production and dissipation. As seen in Fig. 2.8, the ratio of production to dissipation of kinetic energy fluctuates around a value of 1.0 (for our DNS), after an initial increase. The current simulation method focuses only on the velocity fluctuations and by definition has to be statistically stationary in the long term. This is in fact true as the simulation is stable in the long term, and reaches a stationary state where production and dissipation balance each other. The simulations by Kasbaoui *et al.* however had to be stopped at $Bt = 20$, because of the exponential growth of the kinetic energy, where P/ε ratio is much higher than 1 for all the simulations [45]. While being higher than 1, the ratio of P/ε in all three cases have the general same evolution and seem to tend towards unity.

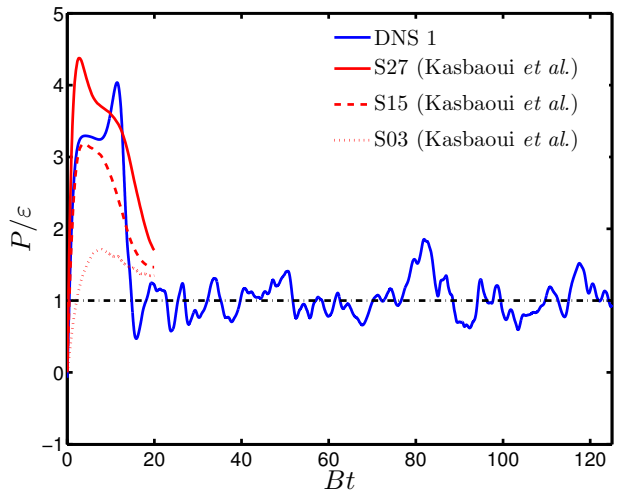

Figure 2.8: Ratio of production to dissipation of kinetic energy. The blue line corresponds to simulations in the current study and the three lines correspond to three simulations by Kasbaoui *et al.*, with different initial conditions.

2.5.1.3 Velocity correlations

The velocity correlation between u'_x and u'_y is analyzed by plotting their joint pdf. Contour plots of the probability density function at different velocity fluctuation values are shown in Fig. 2.9. High probability is found near small values of the velocity fluctuations, and a positive correlation is observed from the positive tilt of the contours. There seems to be few discernible differences between the simulations with only the off-diagonal term (case 3), and with additional diagonal and non-linear terms (case 3b). The key difference is in the skewness of the velocity component towards the negative values, and the maximum being away from the origin for case 3b.

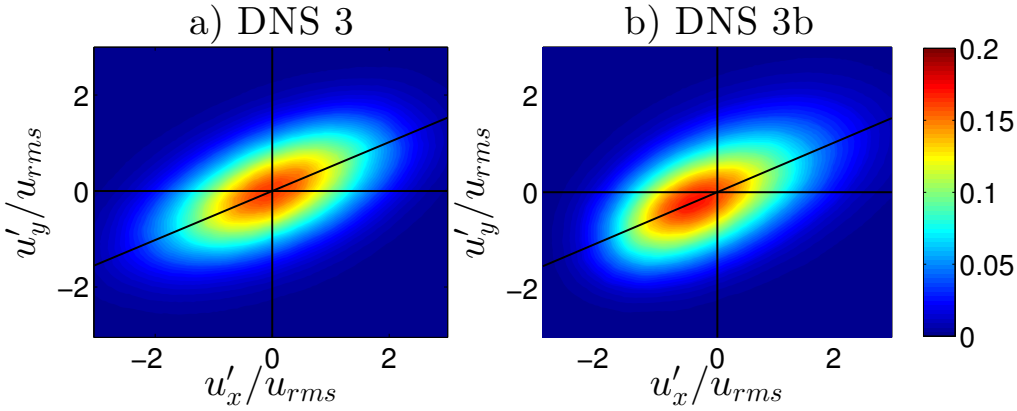

Figure 2.9: Joint pdf of the normalized velocity fluctuations in the x and y directions from simulation with a) just the off-diagonal term, and b) linear and non-linear terms.

The marginal pdf of the velocity fluctuations in the x and y directions are plotted in Fig. 2.10. It was verified that the mean of the velocity fluctuations are zero, despite the high skewness observed in the results of DNS 3b. The velocity fluctuations in the x direction (u'_x) show larger differences between the two simulations. The normalized skewness and flatness for DNS 3 are $\langle u''^3\rangle/\langle u''^2\rangle^{1.5} = -0.03$ and $\langle u''^4\rangle/\langle u''^2\rangle^2 = 2.83$ respectively, while for DNS 3b gives 0.41 and 3.06 respectively. The differences are less prominent in velocity fluctuations in the y direction (u'_y). The skewness and flatness values are -0.01 and 3.02 for DNS 3 and 0.26 and 3.14 for DNS 3b respectively. The skewness values from DNS 3b are comparable to those calculated from the experiments of Hussein *et al* [40], 0.37 for u'_x and 0.45 for u'_y, and Panchapakesan and Lumley [59], 0.44 for u'_x and 0.39 for u'_y. The flatness values for both simulations are near 3.0, which is the flatness for normal distributions.

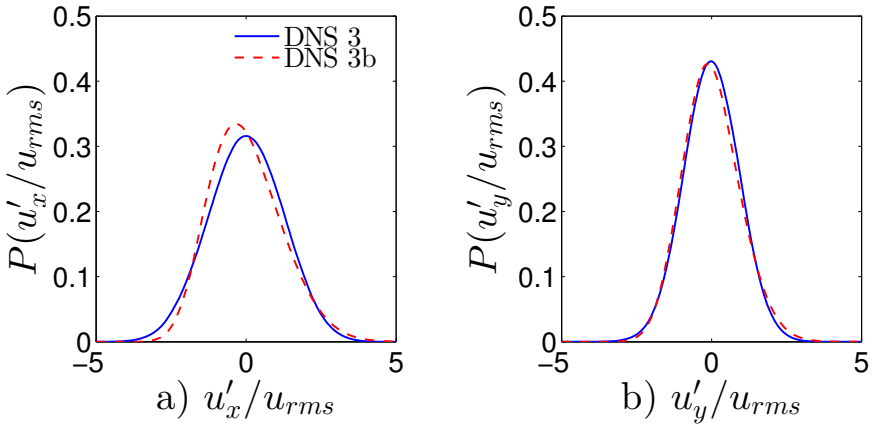

Figure 2.10: Marginal pdf of the normalized velocity fluctuations in the a) x and b) y directions from simulation with just the off-diagonal term, and linear and non-linear terms.

2.5.2 Advection by the mean

As mentioned in section 2.3, homogeneous shear turbulence has been simulated in the past using the off-diagonal production term (Bu'_y), and the advection by the mean term ($By\frac{\partial \boldsymbol{u'}}{\partial x}$). The production term has been included in all the simulations in the current study. The mean advection is represented by the renormalization matrices, A_x and A_r as forcing terms, and captured correctly in the turbulent kinetic energy budget (see section 2.5.1.2). The only effect missing is the straining induced by the mean flow [45, 50, 14, 41].

Multiple studies have performed sheared turbulence simulations by including the shear convection term, but do not reach long term stability and as a result, usually run only until $Bt = 28$ or lower [45, 50, 14, 41, 71]. Kasbaoui*et al.*'s [45] study represents one of the best cases of the past studies, reaching $Bt = 20$, which corresponds to $t/\tau_o = 8$ in our case. Their simulations of sheared turbulence also include the shear convection term, which was implemented using operator splitting. Only a brief description of the multi-step procedure is given here. The reader is referred to Ref. [45] for more details. Step 1 starts with the velocity vector $\boldsymbol{u}^n$, and the momentum equation is solved with the production term included, resulting in $\overline{\boldsymbol{u}}$, referred to as $\boldsymbol{u}_1$ henceforth. Then, step 2 is to apply the shear-remapping, by $\breve{\boldsymbol{u}}(\boldsymbol{x}) = \boldsymbol{u}_1(\boldsymbol{x} - By\Delta t)$ and apply a pressure correction, to get $\boldsymbol{u}^{n+1}$ which is divergence free, referred to as $\boldsymbol{u}_2$. The boundary conditions in the y direction are shear periodic, such that $f(x, L_y, z) = f(x - BtL_y, 0, z)$.

The simulations in our current study solve for the momentum equation with the

production term, hence the velocity field corresponds to $\boldsymbol{u}_1$. To quantify the effect of step 2, the shear convection term is applied *a posteriori*. Specifically, the velocity field is convected in the x direction proportional to the distance in the y direction from the bottom of the domain. The time step ΔT is chosen such that the difference in displacement at $y = 0$ and $y = L_y$ is exactly one grid point, that is $BL_y\Delta T = \Delta x$. This time step was of similar magnitude and slightly higher than the time step per iteration, Δt, in the current study. The pressure correction is then applied to obtain the divergence-free velocity field, $\boldsymbol{u}_2$.

Table 2.4: Turbulence quantities before and after shear remapping.

Re^o_λ	$\boldsymbol{u}_1$			$\boldsymbol{u}_2$			Drop
	k/k_o	$\langle u'_x u'_y\rangle/k$	$\varepsilon/\varepsilon_o$	k/k_o	$\langle u'_x u'_y\rangle/k$	$\varepsilon/\varepsilon_o$	in ε
36	0.842	0.430	1.018	0.842	0.432	0.876	13.9%
54	0.972	0.415	1.139	0.972	0.415	0.984	13.5%
80	0.918	0.394	0.955	0.918	0.394	0.865	9.4%
128	1.019	0.381	0.997	1.019	0.381	0.910	8.7%

The turbulence quantities are calculated from the original data files (corresponding to the velocity field after step 1, $\boldsymbol{u}_1$) and from the shifted data files (corresponding to the velocity field after step 2, $\boldsymbol{u}_2$ using appropriate boundary conditions). The average quantities are summarized in Table 2.4. As expected (see section 2.3.1), the turbulent kinetic energy and the Reynolds shear stress are not affected at all. The only change observed is a reduction in the viscous dissipation rate, ε, by about $8 - 14\%$. The drop in ε decreases with increase in Reynolds number, which is consistent with the *a priori* analysis of shear convection (see Section 2.3.3).

The effect of shear convection on the turbulent kinetic energy can be emulated by decreasing the viscous dissipation rate in two different ways. First and to be consistent with the splitting procedure of Kasbaoui *et al.* [45], a new simulation DNS 3c is performed, where step 1 is to solve the momentum equation with the production term ($\nu_1 = \nu$) and step 2 is to solve the equation,

$$\frac{\partial \boldsymbol{u''}}{\partial t} = \nu_2 \nabla^2 \boldsymbol{u''}, \tag{2.43}$$

with $\nu_2 = -0.10\nu$. This emulates the shear convection term with the operator splitting aspect, where solving the momentum equation and the shear convection are executed as different steps. While these methods likely do not capture all the physical effects of the shear convection, it aims to emulate the biggest effect of shear

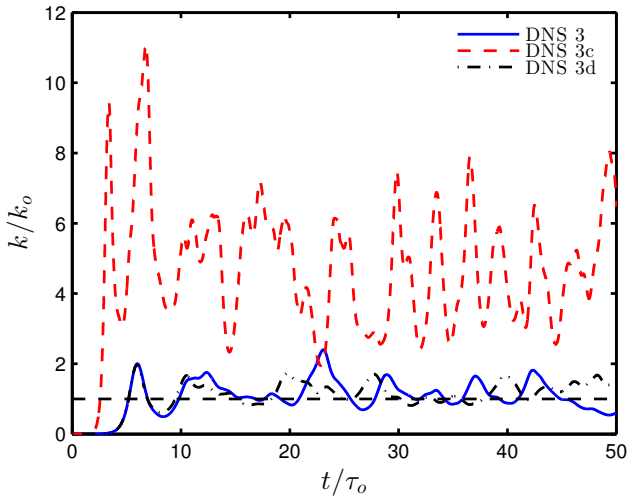

Figure 2.11: Evolution of turbulent kinetic energy normalized by the expected value (Eq. 2.39) for different treatment of the shear convection term.

convection on the turbulence statistics.

Alternatively, if there were no operator splitting and all the operations were to be performed in one step, it would correspond to solving the momentum equation with the production term, and an effective viscosity, $\nu_{eff} = \nu_1 + \nu_2 = 0.90\nu$. DNS 3d is performed under these conditions, which correspond to the same parameters as DNS 3 with $\nu = 0.1431$ instead of 0.159. Figure 2.11 shows the evolution of kinetic energy from the three simulations, DNS 3, DNS 3c, and DNS 3d. Unsurprisingly, DNS 3 and 3d are very similar. Effectively, DNS 3d is a simulation with the pure shear and only a different viscosity, i.e. a different Reynolds number. However, when shear convection is emulated with operator splitting, the evolution of the turbulent kinetic energy is completely different. It is striking that such a small reduction in ε (about 10%) has such a large effect on k (about 500%). From this comparison, proper care must be taken while using operator splitting, considering the numerical implications and errors associated with it.

In the current simulations, the time step per iteration, Δt is approximately equal to ΔT, the time taken for a shift by one grid point. As the actual time step, Δt is reduced, the shear convection term would be applied only every $N_s = \Delta T/\Delta t$ iterations, and its contribution would decrease linearly with decrease in Δt. This first order error (in Δt) is consistent with Godunov-style splitting schemes.

2.6 Conclusions

The velocity field was decomposed into the mean and fluctuating component, and the additional terms in the fluctuating velocity transport equation. The production term was calculated from the mean velocity gradients, as linear forcing terms in the momentum equation. Additional linear and non-linear source terms arise from rescaling the velocity field for periodicity and continuity.

An a priori analysis was performed to calculate the expected kinetic energy, dissipation rate and their scaling dependence on the forcing constant and the domain width at a statistically stationary state. The effect of shear convection was also calculated a priori, and was negligible al large Reynolds numbers.

DNS of shear turbulence was performed in triply periodic cubic domain at different Reynolds numbers. Anisotropy is observed both in the components of velocity and vorticity, with stronger Reynolds number dependence in the anisotropy of vorticity. Energy spectra obtained from the present homogeneous shear turbulence agree well with the spectra from temporally evolving shear layers. The results also highlight the effects of the additional forcing terms that were neglected in previous studies and the role of shear convection and the associated splitting errors in the unbounded evolution of previous numerical simulations.

Chapter 3

INCOMPRESSIBLE TURBULENCE SIMULATIONS IN NON-CUBIC AND NON-HOMOGENEOUS COMPUTATIONAL DOMAINS

3.1 Introduction

The simulations in the previous chapter were performed in cubic and periodic domains. However, performing turbulent flame simulations with similar linear forcing techniques requires cuboidal domains with non-periodic boundary conditions. The domain needs an inflow to introduce more reactants into the domain and an outflow to remove the combustion products, as the flame constantly consumes the reactants and creates products. Furthermore, the domain length needs to be longer in the direction perpendicular to the average flame front, so that the boundary conditions do not affect the flame behavior. An analysis of the turbulent behavior at high aspect ratio and with non-periodic boundary conditions needs to be completed before performing simulations of turbulent flames.

The numerical approach for investigating the effects of aspect ratio is presented in Section 3.2 and the results are discussed in Section 3.4. The numerical approach for performing turbulence simulations with inflow and outflow is detailed in Section 3.5 and the results are provided in Section 3.6.

3.2 Numerical setup

The momentum equation solved in the isotropic simulations is given by

$$\frac{\partial \boldsymbol{u}}{\partial t} + \nabla \cdot (\boldsymbol{u} \otimes \boldsymbol{u}) = -\frac{\nabla p}{\rho} + \nu \nabla^2 \boldsymbol{u} + A\boldsymbol{u'}, \tag{3.1}$$

where A is the isotropic forcing constant, using Lundgren's [53] isotropic forcing technique. The momentum equation solved in the shear simulations is given by

$$\frac{\partial \boldsymbol{u}}{\partial t} + \nabla \cdot (\boldsymbol{u} \otimes \boldsymbol{u}) = -\frac{\nabla p}{\rho} + \nu \nabla^2 \boldsymbol{u} + Bu'_x \boldsymbol{e_y}, \tag{3.2}$$

where B is the shear forcing constant. Note that in the following simulations, the forcing is applied in the y direction, and is proportional to the velocity fluctuations in the x direction.

All simulations in the current section rely on periodic boundary conditions and hence they result in statistical homogeneity in all three directions. Therefore, ensemble averages can be replaced by volume averages, calculated as

$$\langle a \rangle(t) = \frac{1}{V} \int_x \int_y \int_z a(x, y, z, t)\, dx\, dy\, dz. \tag{3.3}$$

The simulation parameters for the different simulations are presented in Table 3.1. We consider two domains with very different aspect ratios. The first one is identical to the one in Chapter 2, where the domain is cubic with a domain width of L in each direction. The second one is elongated in the x direction by a factor of eight.

Table 3.1: Simulation parameters of the triply periodic domain simulations.

	Cubic		Cuboidal	
	Isotropic	Shear	Isotropic	Shear
Domain size	$L \times L \times L$		$8L \times L \times L$	
Grid	$128 \times 128 \times 128$		$1024 \times 128 \times 128$	
$\boldsymbol{f}$	$A\boldsymbol{u'}$	$Bu'_x\boldsymbol{e_y}$	$A\boldsymbol{u'}$	$Bu'_x\boldsymbol{e_y}$
Re_t	160	220	130	200
Re_λ	50	60	45	55
ℓ/L	0.18	0.26	0.16	0.25

The domain width, viscosity, and the forcing constant are kept constant between the simulations, so the effects of the aspect ratio on the turbulent flow can be isolated and analyzed. The simulations are performed using NGA [27], a semi-implicit velocity solver with an energy-conserving finite difference scheme on a standard staggered grid. The code solves the Navier-Stokes equations for constant density, temperature, and viscosity. The simulations are initialized with velocity fields from the results of simulations from DNS 2 of the previous chapter, at similar turbulence parameters. The velocity fields are rescaled, and copied over eight times for the initial conditions of the cuboidal simulations, and random small perturbations (of 1% magnitude compared to u_{rms}) in velocity are included to break symmetry. The two forcing constants are related by $B = 3.2\,A$, as calculated from Chapter 2.

3.3 Stationary state analysis

By construction (see chapter 2), the velocity field represents the fluctuations of the flow field in a small region of a *statistically stationary* turbulent flow. Hence, the fluctuating quantities and their related statistics *must* reach a statistically stationary state. This applies to turbulent kinetic energy, dissipation rate, Reynolds stress,

etc. We briefly review the scaling found in Carroll and Blanquart's study [20], and Chapter 2.

The turbulent kinetic energy equation for the isotropic turbulence forcing, assuming spatial homogeneity, is

$$\frac{dk}{dt} = -\varepsilon + 2Ak. \tag{3.4}$$

At statistically stationary state, the energy dissipation rate is

$$\varepsilon = 2Ak. \tag{3.5}$$

The integral length scale, ℓ, is defined as,

$$\ell = \frac{u_{rms}^3}{\varepsilon} = \frac{u_{rms}}{3A}, \tag{3.6}$$

with

$$u_{rms} = \sqrt{\frac{2k}{3}} = 3A\ell. \tag{3.7}$$

The expected turbulent Reynolds number is calculated as,

$$Re_{t,i}^o = \frac{u_{rms}\ell}{\nu} = \frac{3A\ell^2}{\nu}, \tag{3.8}$$

The Taylor micro-scale, λ, is calculated as

$$\lambda = u_{rms}\sqrt{15\frac{\nu}{\varepsilon}}. \tag{3.9}$$

The expected Taylor micro-scale Reynolds number is given by

$$Re_{\lambda,i}^o = \sqrt{\frac{45A\ell^2}{\nu}}, \tag{3.10}$$

and the expected values for turbulent kinetic energy, $k_{o,i}$, and energy dissipation rate, $\varepsilon_{o,i}$, can be calculated as

$$k_{o,i} = \frac{3}{2}u_{rms}^2 = \frac{27}{2}A^2\ell^2, \tag{3.11}$$

and

$$\varepsilon_{o,i} = \frac{u_{rms}^3}{\ell} = 27A^3\ell^2. \tag{3.12}$$

The expected eddy turnover time τ_o, i is given by

$$\tau_{o,i} = \frac{k_{o,i}}{\varepsilon_{o,i}} = \frac{1}{2A}. \tag{3.13}$$

$\ell/L \simeq 0.18$ for isotropic turbulence in a triply periodic box domain [72, 20], where L is the domain width. It was shown in Chapter 2 that for HST, $u_{rms} = 3B\beta\ell/2$. The expected values for turbulent kinetic energy, $k_{o,s}$, and energy dissipation rate, $\varepsilon_{o,s}$, can be calculated as

$$k_{o,s} = \frac{3}{2}u_{rms}^2 = \frac{27}{8}\beta^2 B^2 \ell^2, \tag{3.14}$$

and

$$\varepsilon_{o,s} = \frac{u_{rms}^3}{\ell} = \frac{27}{8}\beta^3 B^3 \ell^2. \tag{3.15}$$

The expected turbulent Reynolds number is calculated as,

$$Re_{t,s}^o = \frac{u_{rms}\ell}{\nu} = \frac{3B\beta\ell^2}{2\nu}, \tag{3.16}$$

and the expected eddy turnover time, τ_o, is given by

$$\tau_{o,s} = \frac{k_{o,s}}{\varepsilon_{o,s}} = \frac{1}{\beta B}. \tag{3.17}$$

Table 3.2: Scaling parameters of the incompressible turbulence simulations.

	Isotropic			Shear			Advection
	Cubic	Cuboidal	In/Outflow(I/O)	Cubic	Cuboidal	I/O	I/O
k_o		$27A^2\ell^2/2$			$27\beta^2B^2\ell^2/8$		
ε_o		$27A^3\ell^2$			$27\beta^3B^3\ell^2/8$		
Re_t^o		$3A\ell^2/\nu$			$3B\beta\ell^2/2\nu$		
$\boldsymbol{V}$	0	0	0	0	0	0	$V\boldsymbol{e_y}$
ℓ/L	0.18	0.16	0.16	0.26	0.25	0.23	0.33
β	0	0	0	0.40	0.38	0.41	0.31

3.4 Impact of aspect ratio

All four simulations are performed for 100 eddy turnover times, τ, and averages are calculated after a transient period of 10τ. The effects of the aspect ratio on the turbulence and flow anisotropy are discussed in the following subsections. The effects of the aspect ratio on the turbulence quantities are analyzed by observing the differences between the cubic and cuboidal simulations for both isotropic and shear turbulence.

3.4.1 Isotropic turbulence

The turbulent Reynolds number and the normalized integral length scale are shown in Fig. 3.1. The two simulations have similar initial profile, but the cuboidal case

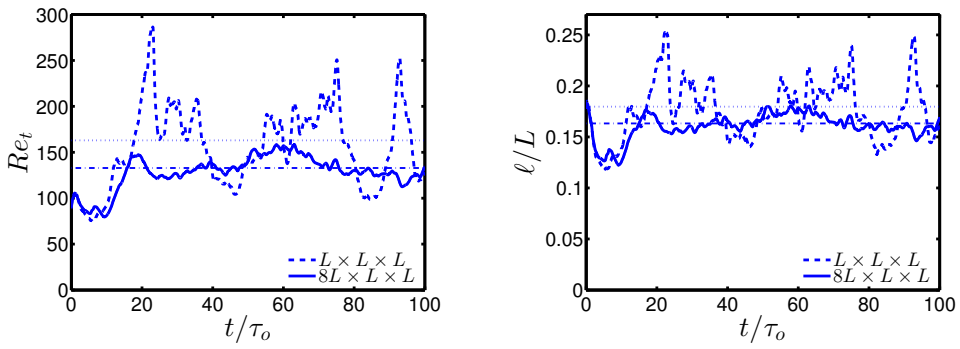

(a) Turbulent Reynolds number

(b) Integral length scale

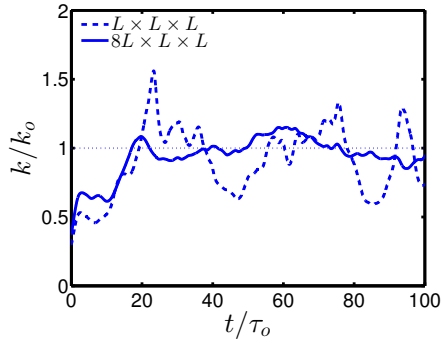

(c) Turbulent kinetic energy

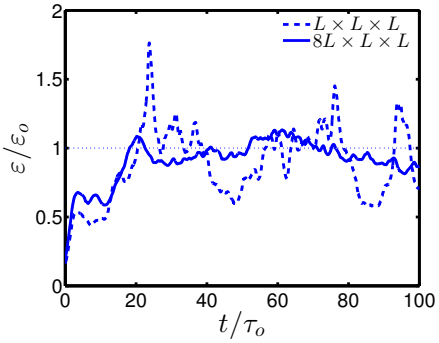

(d) Energy dissipation rate

Figure 3.1: Isotropic turbulence simulation results. Time evolution of the turbulent Reynolds number (a), integral length scale normalized by the domain width L (b), turbulent kinetic energy normalized by the expected values, $k_{o,i}$, (c) energy dissipation rate normalized by the expected values, $\varepsilon_{o,i}$ (d) for cubic (dashed lines) and cuboidal domains (solid lines). Dotted lines and dash-dotted lines in a) and b) represent the average values from the cubic and cuboidal simulations respectively.

has lower turbulent Reynolds number. The volume averages from the long domain simulation have much smaller oscillations owing to the larger number of data points. The oscillations in the cubic simulation results are well known and can theoretically be reduced by using a modification proposed by Carroll and Blanquart [20], but the current study does not use the modification for a cleaner comparison between cases. It can be seen that while the cubic simulation has an average integral length scale value of about $\ell \simeq 0.18\,L$, the cuboidal case shows a smaller integral length scale of about $\ell \simeq 0.16\,L$. The integral length scale in the cuboidal case appears to be controlled by the smallest dimension length, L, (and not $8\,L$), and its reduced integral length scale is consistent with the turbulent reacting flow simulations performed by Brock *et al.* [9] This difference explains the lower Reynolds number, as it is directly

proportional to the square of the integral length scale. The time evolution of kinetic energy and energy dissipation rate are also plotted for the cubic and cuboidal isotropic cases in Fig. 3.1, normalized by their respective expected values calculated using their respective integral length scale values, and they fluctuate around a value of 1.

3.4.2 Shear turbulence

The turbulent Reynolds number and the normalized integral length scale are shown in Fig. 3.2. Once again, it can be seen that while the cubic simulation has an average integral length scale value of about $\ell \simeq 0.26\,L$, the cuboidal case shows a slightly smaller integral length scale of about $\ell \simeq 0.25\,L$. The drop in integral length scale in longer domains for shear turbulence is not as severe as for isotropic turbulence. This difference once again explains the slightly lower Reynolds number, as it is directly proportional to the square of the integral length scale (Eq. (3.16)). The time evolution of kinetic energy and energy dissipation rate are plotted over the domain for the cubic and cuboidal shear cases in Fig. 3.2, normalized by their expected values. The two simulations have similar initial profile, but the cuboidal case has much smaller oscillations owing (once again) to the larger number of data points, and the results from both cases fluctuate around the expected values.

The time evolution of the Reynolds shear stress normalized by the turbulent kinetic energy is plotted in Fig. 3.3. The average value of β is 0.4 for the cubic simulation, 0.38 for the cuboidal simulation. The Reynolds shear stress is not strongly affected by the aspect ratio of the computational domain.

When discussing shear turbulence, the effect of shear convection on the turbulence statistics should also be analyzed. This requires including an imposed mean velocity in the simulation, which has a gradient of $-B$ in the cross-stream direction. This is not possible with a triply periodic computational domain, as the imposed mean velocity is not periodic. Hence, a new computational domain is required in order to include shear convection in these simulations.

3.5 Turbulence with inflow and outflow - Numerical approach

The computational domain is doubly periodic in the y and z directions, and has an inflow/outflow in the x direction. Three different simulations are performed: one with isotropic turbulence, one with shear turbulence, and one where shear forcing is applied along with shear convection.

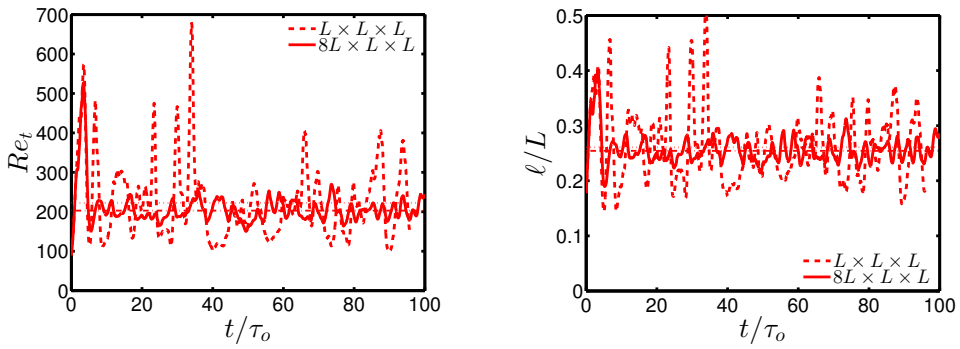

(a) Turbulent Reynolds number

(b) Integral length scale

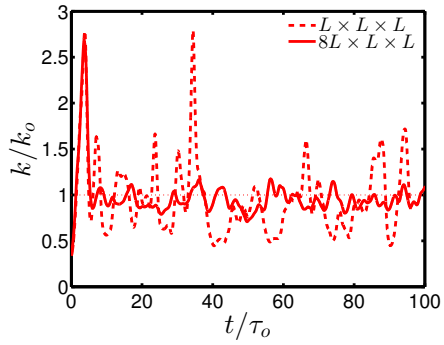

(c) Turbulent kinetic energy

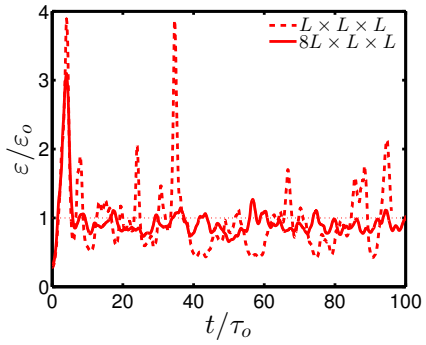

(d) Energy dissipation rate

Figure 3.2: Shear turbulence simulation results. Time evolution of the turbulent Reynolds number (a), integral length scale normalized by the domain width L (b), turbulent kinetic energy normalized by the expected values, $k_{o,i}$, (c) energy dissipation rate normalized by the expected values, $\varepsilon_{o,i}$ (d) for cubic (dashed lines) and cuboidal domains (solid lines). Dotted lines and dash-dotted lines in a) and b) represent the average values from the cubic and cuboidal simulations respectively.

The momentum equation solved in these simulations is given by

$$\frac{\partial \boldsymbol{u}}{\partial t} + \nabla \cdot (\boldsymbol{u} \otimes \boldsymbol{u}) = -\frac{\nabla p}{\rho} + \nu \nabla^2 \boldsymbol{u} + \boldsymbol{f} - \boldsymbol{V} \cdot \nabla \boldsymbol{u}, \tag{3.18}$$

where $\boldsymbol{f}$ is the forcing vector, which is $A\boldsymbol{u'}$ for the isotropic case and $Bu'_x \boldsymbol{e_y}$ for the shear case.

The effect of shear convection was investigated *a priori* in the previous chapter. Leveraging the long domain and the inflow/outflow boundary conditions in the x direction, shear convection is now applied in a portion of the computational domain. More specifically, we introduce a convection velocity, $\boldsymbol{V} = V\boldsymbol{e_y}$, which has a gradient of $-B$ in a portion of the domain between 3.5 L and 7.5 L and V is constant in the rest of the domain. A profile of the convection velocity as a function of x,

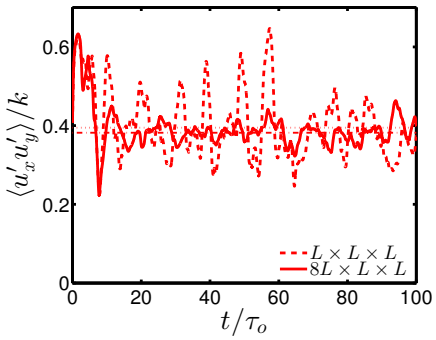

Figure 3.3: Time evolution of Reynolds shear stress normalized by the turbulent kinetic energy.

normalized by the domain width and shear forcing constant is shown in Fig. 3.4. The portion with a mean velocity gradient of $-B$ corresponds to homogeneous shear turbulence with shear convection, whereas the portion with constant V just corresponds to the shear simulation with no shear convection. The simulation parameters for the three different simulations are presented in Table 3.3.

Table 3.3: Simulation parameters of the three different cases of incompressible turbulence with inflow/outflow

	Isotropic	Shear	Advection
Domain size	$11L \times L \times L$		
Grid	$1408 \times 128 \times 128$		
$\boldsymbol{f}$	$A\boldsymbol{u'}$	$Bu_x'\boldsymbol{e_y}$	$Bu_x'\boldsymbol{e_y}$
$\boldsymbol{V}$	0	0	$V\boldsymbol{e_y}$
Re_t	130	130	210
Re_λ	45	45	55

The simulations utilize the same flow configuration used in previous work to simulate turbulent flames [9, 48, 75, 76, 49]. Specifically, the domain is periodic in the y and z direction, which results in statistical homogeneity along these directions. Hence ensemble averages can be replaced by planar averages, calculated as

$$\overline{a}(x,t) = \frac{1}{L^2} \int_y \int_z a(x,y,z,t)\, dy\, dz. \tag{3.19}$$

Based on mass balance, the mean velocity in the x direction, $\overline{u}_x$ is constant. The mean velocity in the parallel directions are set to be zero, $\overline{u}_y = \overline{u}_z = 0$.

The domain has an inflow and an outflow in the x direction, and the mean velocity of the inflow is chosen to be constant in time, and small enough so that the flow from the inlet reaches a statistically stationary state before $x = 0.5\,L$, but large enough to not create any stability issues at the inlet/outlet. Superimposed on the mean velocity at the inflow are fields of fluctuating velocities computed from simulations of homogeneous isotropic turbulence at a lower turbulent Reynolds number. The chosen mean velocity is slightly larger than the rms velocity at the inlet, $\overline{u} \sim 1.15 u_{rms}$, and the time taken for any Lagrangian particles to travel a distance of L in the x direction is $20\,\tau_o$. Convective outflow boundary condition is applied at the outlet at $x = 11\,L$. The velocity fields are subjected to the forcing term, $\boldsymbol{f}$, between $0.5\,L$ and $10\,L$, and the turbulent kinetic energy is expected to be constant through these parts.

Again, the domain width, viscosity, and the forcing constant are kept constant between the three simulations that are compared, so that the effects of the type of forcing and advection by the mean on the turbulent flow can be isolated and analyzed, from the effects of these other parameters. It is ideal for the isotropic and shear simulations to have similar turbulent Reynolds number. The relationship between the two forcing constants can be calculated by equating the two expected turbulent Reynolds numbers,

$$Re^o_{t,i} = \frac{3A\ell_i^2}{\nu} = \frac{3B\beta\ell_s^2}{2\nu} = Re^o_{t,s}, \tag{3.20}$$

$$B = \frac{2A}{\beta}\left(\frac{\ell_i}{\ell_s}\right)^2. \tag{3.21}$$

From initial simulations, the integral length scales were calculated as $\ell_i \simeq 0.16\,L$ and $\ell_s \simeq 0.23\,L$. The isotropic and shear forcing constants are hence related by $B = 2.4\,A$.

3.6 Turbulence with inflow and outflow

The effects of the forcing technique and mean advection on the turbulence and flow anisotropy are discussed in the following subsections.

3.6.1 Effects of forcing

The effects of the forcing matrix on the turbulence quantities are analyzed by observing the differences between the isotropic simulation and the shear simulation.

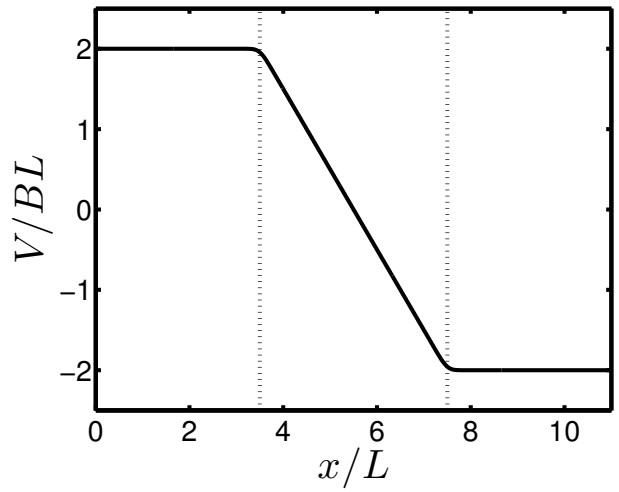

Figure 3.4: Advection velocity profile normalized by the shear forcing constant and domain width.

3.6.1.1 Global quantities

The turbulent Reynolds number is plotted in Fig. 3.5a. The Reynolds number is constant in the portion where the forcing is applied, and much lower near the inlet and outlet. The Reynolds number for the shear case reaches a high value at a transient region near the inlet, and stabilizes to a constant value of around 130, comparable to that of the isotropic case. The time averaged integral length scale is plotted for the two cases in Fig. 3.5b. The integral length scale is $\ell \simeq 0.16\,L$ for the isotropic forcing and is the same value from the triply periodic cuboidal domain. The value is $\ell \simeq 0.23\,L$ for the shear forcing, which is about 1.5 times the integral length scale for the isotropic case. This was observed in triply periodic simulations as well. These values are used in the calculation of the expected values of the turbulent kinetic energy and the dissipation rate. The time-averaged kinetic energy and energy dissipation rate are plotted over the domain for the two cases in Fig. 3.5, normalized by their respective expected values. The two simulations have similar kinetic energy and energy dissipation rate profiles as seen in Fig. 3.5, and have small fluctuations around the expected values for most of the domain.

3.6.1.2 Effects on flow anisotropy

As shown in section 3.6.1.1, the turbulence intensity is comparable between the different forcing techniques, but large differences are expected in the turbulence

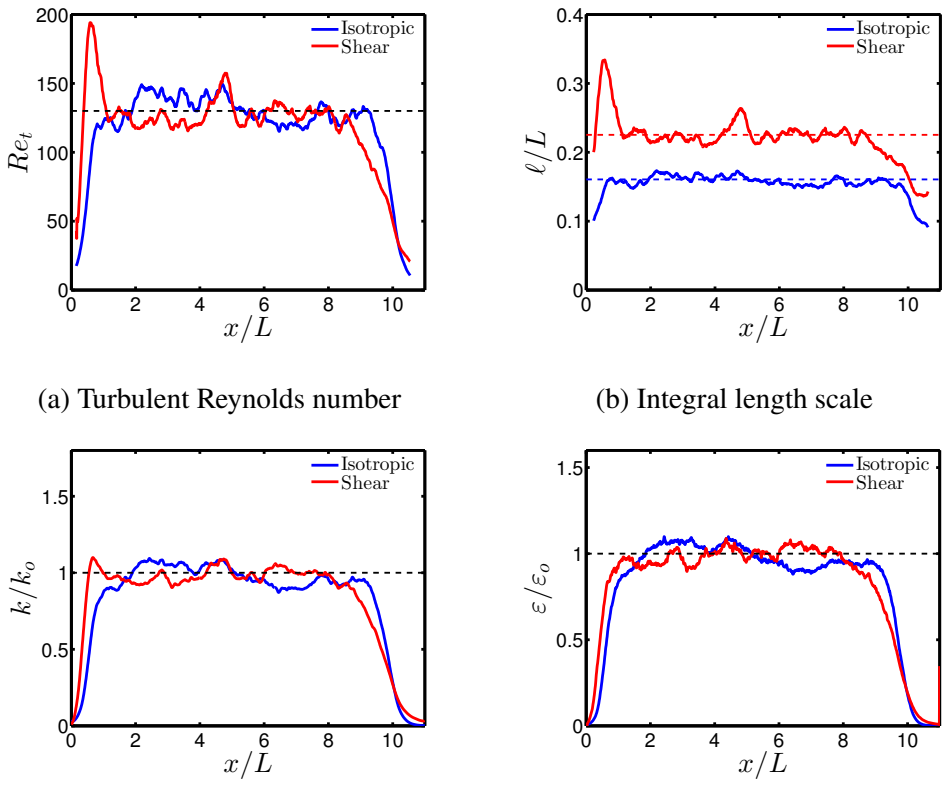

(a) Turbulent Reynolds number

(b) Integral length scale

(c) Turbulent kinetic energy

(d) Energy dissipation rate

Figure 3.5: a) Turbulent Reynolds number profile, b) Integral length scale normalized by the domain width, c) Turbulent kinetic energy profile normalized by the expected value k_o, d) Energy dissipation rate normalized by the expected value ε_o, for isotropic (blue) and shear forcing (red) cases. Dashed lines in b) correspond to average values.

anisotropy. This anisotropy can be characterized by examining the components of the velocity and vorticity vectors.

The magnitudes of the fluctuating velocity components are plotted as a function of space, normalized by $|u_{rms}|$ in Fig. 3.6a for the isotropic forcing and Fig. 3.6b for the shear forcing. For the isotropic forcing, the velocity fluctuations are statistically isotropic throughout. With shear forcing, the velocity components are significantly anisotropic throughout the domain. It is important to note that for the shear forcing case, the shear forcing is applied in the y direction, proportional to the velocity fluctuations in the x direction. The velocity components are the strongest in magnitude in the forced direction (y), which is consistent with simulations from the previous chapter. The average values of the velocity anisotropy are calculated as $|u'_x|/|u_{rms}| = 0.93$, $|u'_y|/|u_{rms}| = 1.23$, and $|u'_z|/|u_{rms}| = 0.79$.

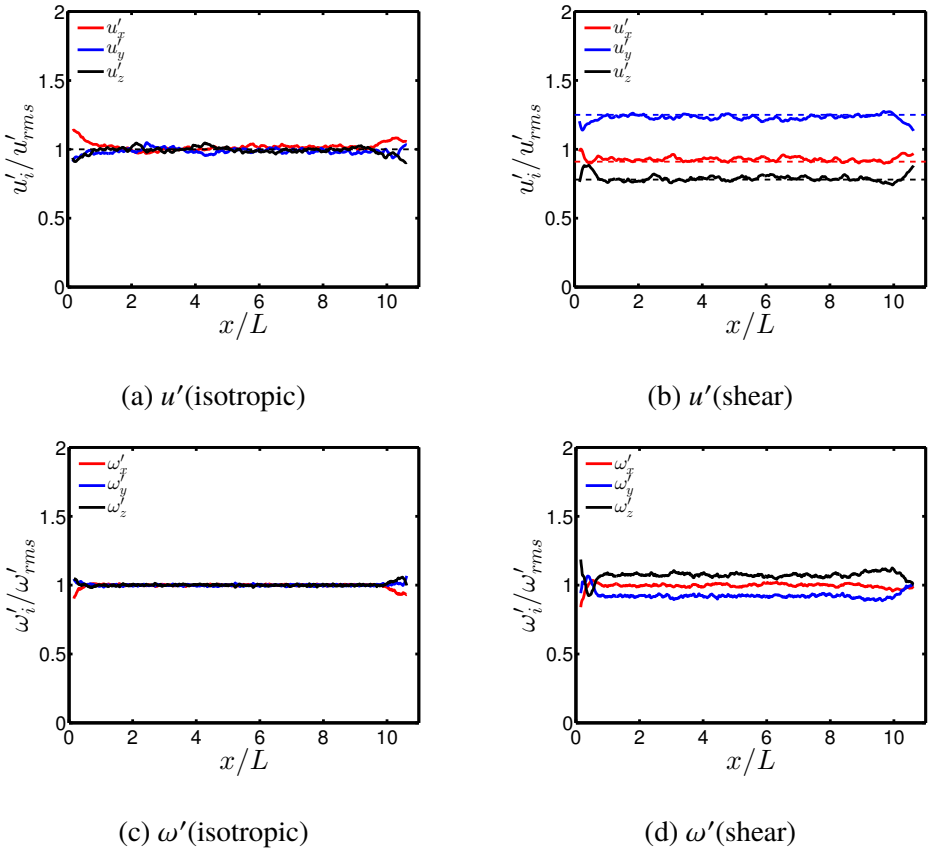

(a) u'(isotropic) (b) u'(shear)

(c) ω'(isotropic) (d) ω'(shear)

Figure 3.6: Velocity fluctuation magnitudes for the isotropic forcing (a) and shear forcing (b), normalized by the root mean square velocity, u_{rms}. Vorticity fluctuation magnitudes normalized by the root mean square velocity, ω_{rms}, for the isotropic forcing c) and shear forcing d). Dashed lines in (b) correspond to average values.

The anisotropy in the small scales can be studied by evaluating the rms vorticity components along the different directions, $|\omega'_i| = (\overline{\omega'_i\omega'_i})^{1/2}$. They are shown, normalized by $|\omega_{rms}| = ((\overline{\omega'_x\omega'_x} + \overline{\omega'_y\omega'_y} + \overline{\omega'_z\omega'_z})/3)^{1/2}$ for the isotropic forcing in Fig. 3.6c and for the shear forcing in Fig. 3.6d. The isotropic forcing technique produces isotropic vorticity fields $|\omega'_i|/|\omega_{rms}| \simeq 1$ throughout the domain. In contrast and as mentioned previously, in the shear forcing case, the vorticity is somewhat anisotropic. The vorticity component magnitudes are given by $|\omega'_x|/|\omega_{rms}| = 1.00$, $|\omega'_y|/|\omega_{rms}| = 1.07$, and $|\omega'_z|/|\omega_{rms}| = 0.92$ and are consistent with the anisotropy in vorticity from Chapter 2.

Another significant measure of the anisotropy on the flow is the Reynolds shear stress. Figure 3.7 shows the Reynolds shear stress profile normalized by the turbulent kinetic energy for the isotropic and shear case. As expected, there is zero Reynolds shear stress in the isotropic case, as there is no cross-correlation of the velocity

components. For the shear case, however the Reynolds shear stress is positive, and has a value of $\beta = 0.41$, which agrees well with results from Chapter 2 and Table 3.2.

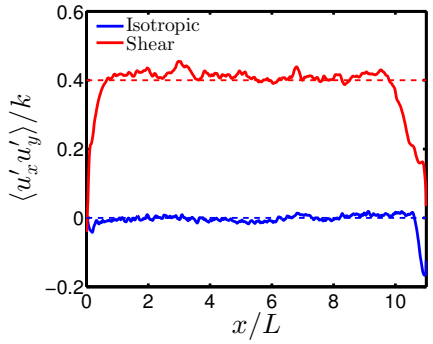

Figure 3.7: Reynolds shear stress profile normalized by the turbulent kinetic energy.

3.6.2 Effects of advection

The effects of the mean advection on the turbulence quantities are analyzed by observing the differences between the shear simulation and the advection simulation. Once again, the mean advection velocity in the advection simulation, $\boldsymbol{V}$, is in the y direction, and has a gradient of $-B$ from $x = 3.5\,L$ to $x = 7.5\,L$, in the middle of the domain. This portion is used to compare and contrast the turbulence statistics between simulations with just shear turbulence production, and simulations with shear turbulence production and shear convection.

3.6.2.1 Global quantities

The turbulent Reynolds number is shown in Fig. 3.8a. As expected, the Reynolds number is similar for all three simulations except for the region where shear convection is applied. The increase in turbulent Reynolds number in the shear convection region can be explained by the increase in integral length scale as observed in Fig. 3.8b. The average integral length scale is calculated between $x = 4\,L$ to $x = 7\,L$ for the two cases, and $\ell \simeq 0.23\,L$ for the shear case and $\ell \simeq 0.33\,L$ when shear convection is included. In other words, the integral length scale is larger when shear convection is included, by about 50%. The time-averaged kinetic energy and energy dissipation rate are plotted over the domain for the three cases in Fig. 3.8, normalized by their respective expected values. The three simulations have similar kinetic energy and energy dissipation rate as seen in Fig. 3.8 outside the convection region, but the turbulent kinetic energy is once again much higher in the region with

shear convection for the advection simulation, and the dissipation rate is slightly lower.

As shown from the results, when shear convection is included, $\ell/L \simeq 0.33$ and $\beta \simeq 0.31$. So, the expected turbulence quantities with convection can be calculated as

$$k_{o,a} = k_{o,s} \left(\frac{\beta_a}{\beta_s}\right)^2 \left(\frac{\ell_a}{\ell_s}\right)^2 \simeq 1.21\ k_{o,s}, \tag{3.22}$$

$$\varepsilon_{o,a} = \varepsilon_{o,s} \left(\frac{\beta_a}{\beta_s}\right)^3 \left(\frac{\ell_a}{\ell_s}\right)^2 \simeq 0.92\ \varepsilon_{o,s}, \tag{3.23}$$

and

$$Re^o_{t,a} = Re^o_{t,s} \left(\frac{\beta_a}{\beta_s}\right) \left(\frac{\ell_a}{\ell_s}\right)^2 \simeq 1.60\ Re^o_{t,s}. \tag{3.24}$$

This explains the higher Reynolds number and turbulent kinetic energy and slightly lower dissipation observed where shear convection is included.

3.6.2.2 Effects on flow anisotropy

The effect of the mean convection on the turbulence anisotropy can be studied by comparing the results from the shear simulation and the advection simulation, specifically in the region between $3.5\,L$ and $7.5\,L$. The anisotropy is once again characterized by examining the components of the velocity and vorticity vectors.

The magnitudes of the fluctuating velocity components are plotted, normalized by $|u_{rms}|$ in Fig. 3.9a for the shear case and Fig. 3.9b for the advection case. With shear forcing, the velocity components are anisotropic throughout the domain, and their values are given by $|u'_x|/|u_{rms}| = 0.93$, $|u'_y|/|u_{rms}| = 1.23$, and $|u'_z|/|u_{rms}| = 0.79$. In the portion where shear convection is included in the advection case, the velocity components are still anisotropic, but the values are slightly different, and now $|u'_x|$ is the weakest, with the values given by $|u'_x|/|u_{rms}| = 0.83$, $|u'_y|/|u_{rms}| = 1.24$, and $|u'_z|/|u_{rms}| = 0.88$. These values agree better with experiments and simulations of shear-dominated flows like mixing layers and jets, as seen in Fig. 3.11a. It is important to note that since the forcing is applied in the y direction proportional to the fluctuations in the x directions, u'_y should be compared to the streamwise velocity fluctuations and u'_x should be compared to the cross-stream velocity fluctuations.

The rms vorticity components along the different directions, $|\omega'_i|$, normalized by $|\omega_{rms}|$ are plotted for the shear simulation in Fig. 3.9c and for the advection forcing in Fig. 3.9d. The shear simulation vorticity component magnitudes are given by

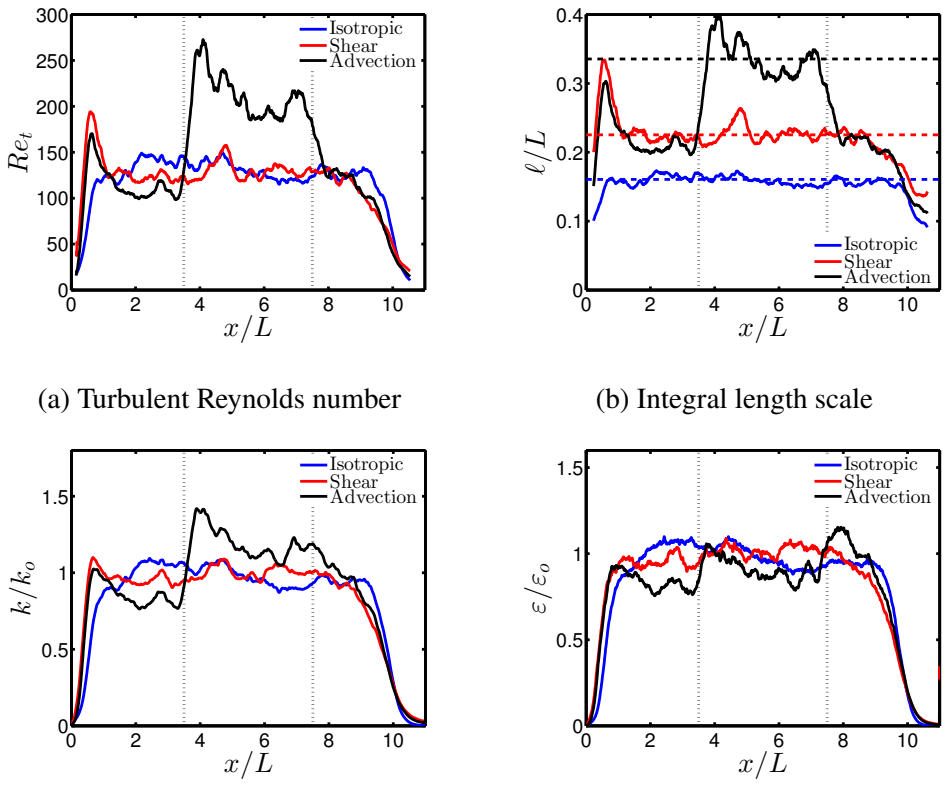

(a) Turbulent Reynolds number

(b) Integral length scale

(c) Turbulent kinetic energy

(d) Energy dissipation rate

Figure 3.8: a) Turbulent Reynolds number profile, b) Integral length scale normalized by the domain width, c) Turbulent kinetic energy profile normalized by the expected value, k_o, d) Energy dissipation rate normalized by the expected value, ε_o, for isotropic (blue), shear (red), and advection (black) cases.

$|\omega_x'|/|\omega_{rms}| = 1.00$, $|\omega_y'|/|\omega_{rms}| = 0.92$, and $|\omega_z'|/|\omega_{rms}| = 1.07$. When shear convection is included, however, the ω_y' becomes the dominant vorticity component, and the average values are given by $|\omega_x'|/|\omega_{rms}| = 0.99$, $|\omega_y'|/|\omega_{rms}| = 1.07$, and $|\omega_z'|/|\omega_{rms}| = 0.94$.

Another significant impact of the shear convection on the flow is on the Reynolds shear stress. Fig. 3.10 shows the Reynolds shear stress profile normalized by the turbulent kinetic energy for the shear and advection case. As mentioned earlier, for the shear case, the Reynolds shear stress has a value of $\beta \simeq\approx 0.41$, and the portion with shear convection shows a value of $\beta \simeq 0.31$, which agrees better with results from the literature of shear-dominated turbulent flows such as mixing layers, planar jets, and round jets, as seen in Fig. 3.11b.

The turbulent kinetic energy budget values are calculated using the same method

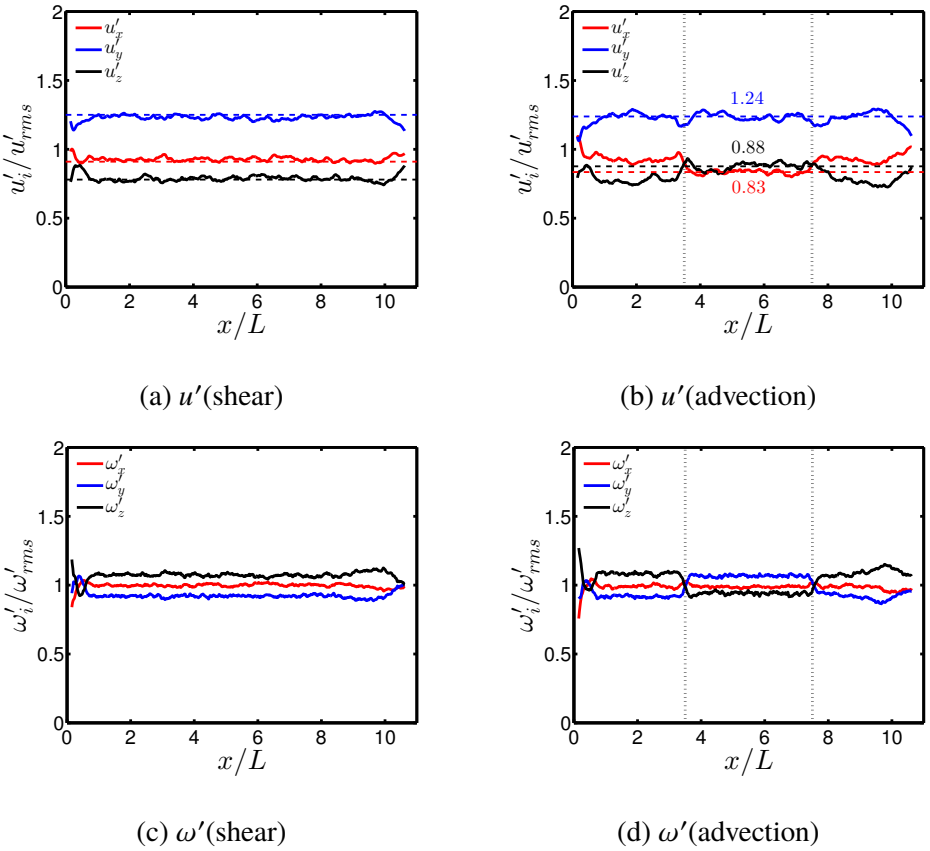

(a) u'(shear) (b) u'(advection)

(c) ω'(shear) (d) ω'(advection)

Figure 3.9: Velocity fluctuation magnitudes for the shear simulation (a) and advection simulation (b), normalized by the root mean square velocity, u_{rms}. Vorticity fluctuation magnitudes normalized by the root mean square vorticity, ω_{rms}, for the shear simulation (c) and advection simulation (d). Dotted lines in these plots correspond to the part of the domain where shear convection is included. Dashed lines correspond to average values calculated between 4 L and 7 L.

as in Section 2.5.1.2 and plotted in Fig. 3.12 with results from Section 2.5.1.2 and the experiment results of Panchapakesan and Lumley [59]. All the values are normalized by $U_o^3/r_{1/2}$, where U_o is calculated as $U_o = \sqrt{k/0.052}$ [59] and $r_{1/2}$ is calculated as $r_{1/2} = 0.586U_o/B$ [77]. As expected, the shear convection term had zero contribution to the turbulent kinetic energy budget and is not included in the budget plot. It can be seen that the production, advection and dissipation are accurately captured, compared to the simulations without advection.

3.7 Conclusions

The impact of the aspect ratio of the computational domain on both isotropic and shear turbulence characteristics was studied. The integral length scale was reduced

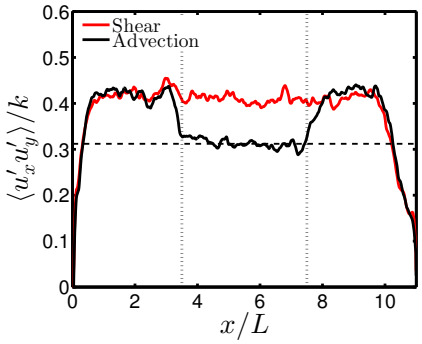

Figure 3.10: Reynolds shear stress profile normalized by the turbulent kinetic energy.

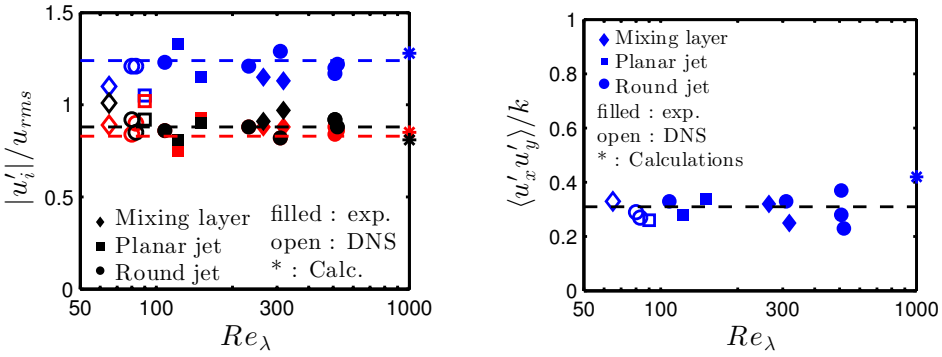

(a) Anisotropy in u'

(b) Reynolds shear stress

Figure 3.11: a) Anisotropy in velocity from other studies of free shear flows as a function of Reynolds number for u'_x (red), u'_y (blue), and u'_z (black) b) Reynolds shear stress values as a function of Reynolds number. Dashed lines correspond to the portion with the shear convection included from the advection case.

for the case of isotropic turbulence. Introducing an inflow/outflow in one direction had very small effects on both isotropic turbulence and shear turbulence. The velocity and vorticity components remained isotropic for the isotropic turbulence forcing scheme as expected, and anisotropic for the shear turbulence. Shear convection was introduced in a region of the domain along with shear turbulence forcing. This resulted in statistically stationary shear turbulence, with larger integral length scale, and anisotropy values that agree much better with those of free shear flows.

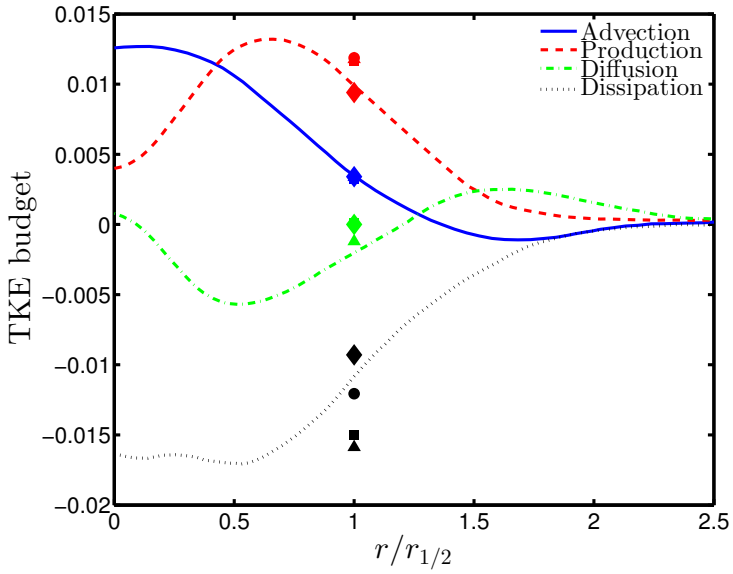

Figure 3.12: Normalized turbulent kinetic energy budget. The lines correspond to experimental results from Panchapakesan and Lumley [59]. Symbols correspond to different simulations: Incompressible with shear convection - diamonds, Chapter 2 results: DNS 3 - circles, DNS 3a - triangles, DNS 3b - squares.

Chapter 4

MATHEMATICAL DERIVATION OF THE TURBULENCE FORCING TECHNIQUE FOR TURBULENT FLAMES

4.1 Introduction

The flows considered in the current study are highly turbulent reacting flows and a cuboidal Cartesian domain is considered in the vicinity of the flame front, at $\boldsymbol{x_F}$, as seen in Fig. 4.1, with the unburnt side of the flow on the left of the flame front in the domain. The final goal is to perform statistically stationary simulations of turbulent flames in this canonical cuboidal computational domain, that represent turbulent flame behavior observed in more complex geometries. A list of assumptions is mentioned in Section 4.2 and the governing equations for the turbulent flame simulations are described in Section 4.3. The Favre velocity decomposition of the velocity field is explained in Section 4.4 and the average velocity is decomposed further in Section 4.5. The velocity field is rescaled to correct for periodicity and continuity in Section 4.6, the impact of each of the source terms are discussed in Section 4.7, and finally the forcing matrix is calculated in Section 5.1.1.

4.2 Assumptions

A list of assumptions is needed to simulate the spatially-evolving reacting flows using simple computational domains.

1. The reacting flows considered are statistically stationary, which means the ensemble averages are independent of time.
2. The computational domain is small, and is in the vicinity of the target flame location, $\boldsymbol{x_F}$.
3. The turbulence is fully developed in the vicinity of $\boldsymbol{x_F}$.
4. The curvature of the mean flame front is small in comparison to the computational domain.
5. The turbulent Mach number is low in the vicinity of $\boldsymbol{x_F}$.

The gradient of the mean density is calculated in the target flows and using assumption 1, it is only a function of space. The average flame front is located by tracking the

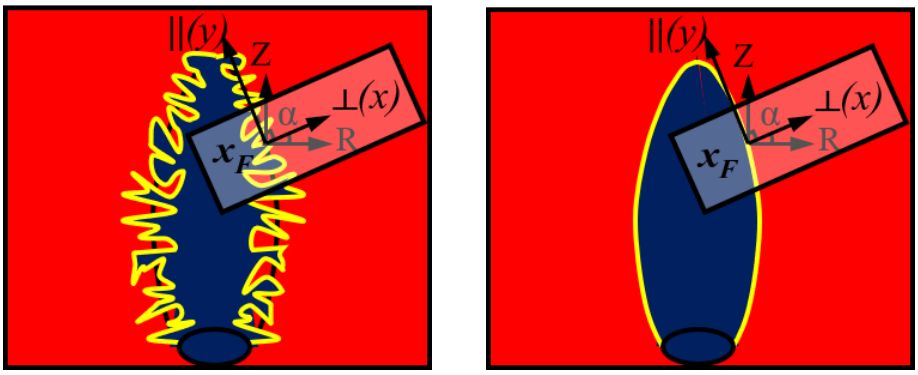

(a) Instantaneous flame location (b) Mean flame location

Figure 4.1: Reacting jet schematic, with unburnt mixture represented in blue, flame location in yellow, and burnt mixture in red. The black cuboid marks the simulation domain, with the Cartesian directions of the domain indicated.

locations where the gradient reaches its maximum value, when traversing along the gradient. The longer direction of the cuboidal computational domain, $\boldsymbol{e}_{\perp}$, is chosen perpendicular to the average flame front, i.e., $\boldsymbol{e}_{\perp} = -\nabla\overline{\rho}/|\nabla\overline{\rho}|$. The domain has an inflow/outflow configuration in the direction perpendicular to the flame ($\boldsymbol{e}_{\boldsymbol{x}} = \boldsymbol{e}_{\perp}$), with periodic boundary conditions in the parallel directions ($\boldsymbol{e}_{\boldsymbol{y}} = \boldsymbol{e}_{\parallel}, \boldsymbol{e}_{\boldsymbol{z}} = \boldsymbol{e}_{|}$).

4.3 Governing equations

The governing equations considered for the current turbulent flame simulations are low Mach number Navier-Stokes equations. The conservation of mass is given by

$$\frac{\partial \rho}{\partial t} + \nabla \cdot (\rho \boldsymbol{u}) = 0\,. \tag{4.1}$$

The conservation of linear momentum equation is

$$\frac{\partial}{\partial t}(\rho \boldsymbol{u}) + \nabla \cdot (\rho \boldsymbol{u} \otimes \boldsymbol{u}) + \nabla p - \nabla \cdot \underline{\underline{\tau}} = 0\,, \tag{4.2}$$

where p is the hydrodynamic pressure field and $\underline{\underline{\tau}}$ is the viscous stress tensor. The species transport equation is expressed as

$$\frac{\partial}{\partial t}(\rho Y_i) + \nabla \cdot (\rho \boldsymbol{u} Y_i) + \nabla \cdot \boldsymbol{j}_i - \dot{\omega}_i = 0\,, \tag{4.3}$$

where Y_i, $\dot{\omega}_i$, and $\boldsymbol{j}_i$ are the mass fraction, production rate, and diffusion flux, respectively, of species i. The diffusion flux is calculated as

$$\boldsymbol{j}_i = -\rho D_i \frac{Y_i}{X_i} \nabla X_i - \rho Y_i \boldsymbol{u}_{\boldsymbol{c}}\,, \tag{4.4}$$

where D_i is the species diffusivity, calculated as $D_i = \alpha/Le_i$, where $\alpha = \lambda/(\rho c_p)$ is the thermal diffusivity of the mixture, where λ is the thermal conductivity of the mixture, and Le_i is the Lewis number of species i. Constant non-unity Lewis numbers calculated from corresponding laminar flames are used. X_i is the mole fraction of species i, and $\boldsymbol{u_c}$ is the correction velocity to ensure zero net diffusion flux, $\sum_i \boldsymbol{j}_i = 0$ [5]. The conservation of energy is implemented as a transport equation for temperature, T, using the form

$$\frac{\partial}{\partial t}(\rho T) + \nabla \cdot (\rho \boldsymbol{u} T) - \frac{1}{c_p}\nabla \cdot (\lambda \nabla T) - \dot{\omega}_T + \frac{1}{c_p}\sum_i c_{p,i}\boldsymbol{j}_i \cdot \nabla T = 0\,, \tag{4.5}$$

where $c_{p,i}$ is the heat capacity of species i, $c_p = \sum_i Y_i c_{p,i}$ is the heat capacity of the mixture, and $\dot{\omega}_T = -1/c_p \sum_i h_i \dot{\omega}_i$ is the heat source term, where h_i is the specific enthalpy of species, i. The equation of state used to bring closure to this system of equations is given by

$$p_0 = \rho R T \sum_i \frac{Y_i}{W_i} \tag{4.6}$$

where p_0 is the thermodynamic pressure, R is the universal gas constant, and W_i is the molecular weight of species i. Using the low turbulent Mach number assumption (5), the fluctuations in the hydrodynamic pressure field, p, are small compared to the constant thermodynamic pressure, p_0, used in the equation of state.

4.4 Limits of Favre velocity decomposition

Lundgren's analysis [14] decomposed the velocity field into mean and fluctuating quantities. More specifically, Lundgren's method considered constant density flows and the velocity is split using Reynolds decomposition, $\boldsymbol{u} = \overline{\boldsymbol{u}} + \boldsymbol{u'}$, where $\overline{\cdot}$ represents the ensemble average. For turbulent flame simulations involving variable density flows, a Favre decomposition is more appropriate, $\boldsymbol{u} = \widetilde{\boldsymbol{u}} + \boldsymbol{u''}$, where $\widetilde{\cdot}$ is the Favre-average defined by $\widetilde{a} = \overline{\rho a}/\overline{\rho}$. Applying ensemble averaging on the continuity equation gives

$$\frac{\partial \overline{\rho}}{\partial t} + \nabla \cdot (\overline{\rho \boldsymbol{u}}) = \nabla \cdot (\overline{\rho}\widetilde{\boldsymbol{u}}) = 0\,, \tag{4.7}$$

where $\frac{\partial \overline{\rho}}{\partial t} = 0$ because of the statistical stationarity. The continuity equation for the fluctuating velocity is hence given by,

$$\frac{\partial \rho}{\partial t} + \nabla \cdot (\rho \boldsymbol{u''}) = -\widetilde{\boldsymbol{u}} \cdot \nabla \rho - \rho \nabla \cdot \widetilde{\boldsymbol{u}}\,, \tag{4.8}$$

with the additional terms representing advection by the mean flow and dilatation, respectively. Applying ensemble averaging on the conservation of linear momentum,

we arrive at the Favre-averaged Navier-Stokes equation,

$$\frac{\partial}{\partial t}(\overline{\rho}\widetilde{\boldsymbol{u}}) + \nabla\cdot(\overline{\rho}\widetilde{\boldsymbol{u}}\otimes\widetilde{\boldsymbol{u}}) = -\nabla\overline{p} + \nabla\cdot\underline{\underline{\overline{\tau}}} - \nabla\cdot\left(\overline{\rho\boldsymbol{u}''\otimes\boldsymbol{u}''}\right). \tag{4.9}$$

The transport equation for $\rho\boldsymbol{u}'' = \rho(\boldsymbol{u}-\widetilde{\boldsymbol{u}})$, calculated from the difference between Eq. (4.2) and Eq. (4.9), is given by

$$\begin{aligned}\frac{\partial}{\partial t}(\rho\boldsymbol{u}'') + \nabla\cdot(\rho\boldsymbol{u}''\otimes\boldsymbol{u}'') = -\nabla p' + \nabla\cdot\underline{\underline{\tau'}} - \frac{\partial}{\partial t}(\rho'\widetilde{\boldsymbol{u}}) - \nabla\cdot(\rho'\widetilde{\boldsymbol{u}}\otimes\widetilde{\boldsymbol{u}})\\ - \nabla\cdot(\rho\widetilde{\boldsymbol{u}}\otimes\boldsymbol{u}'') - \nabla\cdot(\rho\boldsymbol{u}''\otimes\widetilde{\boldsymbol{u}}) + \nabla\cdot\left(\overline{\rho\boldsymbol{u}''\otimes\boldsymbol{u}''}\right),\end{aligned} \tag{4.10}$$

where $a' = a - \overline{a}$ is the fluctuating part of a. Some of the additional terms can be expanded as

$$\begin{aligned}-\frac{\partial}{\partial t}(\rho'\widetilde{\boldsymbol{u}}) &= -\widetilde{\boldsymbol{u}}\frac{\partial\rho'}{\partial t} = -\widetilde{\boldsymbol{u}}\frac{\partial\rho}{\partial t}\\ -\nabla\cdot(\rho'\widetilde{\boldsymbol{u}}\otimes\widetilde{\boldsymbol{u}}) &= -\widetilde{\boldsymbol{u}}\nabla\cdot(\rho'\widetilde{\boldsymbol{u}}) - \rho'\widetilde{\boldsymbol{u}}\cdot\underline{\underline{\nabla\widetilde{\boldsymbol{u}}}}\\ -\nabla\cdot(\rho\widetilde{\boldsymbol{u}}\otimes\boldsymbol{u}'') &= -\widetilde{\boldsymbol{u}}\nabla\cdot(\rho\boldsymbol{u}'') - \rho\boldsymbol{u}''\cdot\underline{\underline{\nabla\widetilde{\boldsymbol{u}}}}\\ -\nabla\cdot(\rho\boldsymbol{u}''\otimes\widetilde{\boldsymbol{u}}) &= -\rho\boldsymbol{u}''(\nabla\cdot\widetilde{\boldsymbol{u}}) - \widetilde{\boldsymbol{u}}\cdot\underline{\underline{\nabla(\rho\boldsymbol{u}'')}}\\ \rho\boldsymbol{u}'' + \rho'\widetilde{\boldsymbol{u}} &= \rho\boldsymbol{u}'' + \rho\widetilde{\boldsymbol{u}} - \overline{\rho}\widetilde{\boldsymbol{u}} = \rho\boldsymbol{u} - \overline{\rho}\widetilde{\boldsymbol{u}}\\ -\rho'\widetilde{\boldsymbol{u}}\cdot\underline{\underline{\nabla\widetilde{\boldsymbol{u}}}} - \rho\boldsymbol{u}''\cdot\underline{\underline{\nabla\widetilde{\boldsymbol{u}}}} &= -(\rho\boldsymbol{u} - \overline{\rho}\widetilde{\boldsymbol{u}})\cdot\underline{\underline{\nabla\widetilde{\boldsymbol{u}}}}\end{aligned}$$

Using continuity (Eqs. (4.1) and (4.7)),

$$-\widetilde{\boldsymbol{u}}\left(\frac{\partial\rho}{\partial t} + \nabla\cdot(\rho'\widetilde{\boldsymbol{u}}) + \nabla\cdot(\rho\boldsymbol{u}'')\right) = -\widetilde{\boldsymbol{u}}\left(\frac{\partial\rho}{\partial t} + \nabla\cdot(\rho\boldsymbol{u}) - \nabla\cdot(\overline{\rho}\widetilde{\boldsymbol{u}})\right) = 0$$

After applying the above-mentioned expansions and simplifications, Eq. (4.10) becomes

$$\begin{aligned}\frac{\partial}{\partial t}(\rho\boldsymbol{u}'') + \nabla\cdot(\rho\boldsymbol{u}''\otimes\boldsymbol{u}'') = -\nabla p' + \nabla\cdot\underline{\underline{\tau'}} - (\rho\boldsymbol{u} - \overline{\rho}\widetilde{\boldsymbol{u}})\cdot\underline{\underline{\nabla\widetilde{\boldsymbol{u}}}}\\ - \widetilde{\boldsymbol{u}}\cdot\underline{\underline{\nabla(\rho\boldsymbol{u}'')}} - \rho\boldsymbol{u}''(\nabla\cdot\widetilde{\boldsymbol{u}}) + \nabla\cdot\left(\overline{\rho\boldsymbol{u}''\otimes\boldsymbol{u}''}\right),\end{aligned} \tag{4.11}$$

where $-(\rho\boldsymbol{u} - \overline{\rho}\widetilde{\boldsymbol{u}})\cdot\underline{\underline{\nabla\widetilde{\boldsymbol{u}}}}$ corresponds to the production of turbulent kinetic energy, $-\widetilde{\boldsymbol{u}}\cdot\underline{\underline{\nabla(\rho\boldsymbol{u}'')}}$ is the advection by the mean flow, $-\rho\boldsymbol{u}''(\nabla\cdot\widetilde{\boldsymbol{u}})$ corresponds to dilatation, and $\nabla\cdot\left(\overline{\rho\boldsymbol{u}''\otimes\boldsymbol{u}''}\right)$ is the divergence of the Reynolds stress. Using the same analysis as Lundgren [14], most of the contribution to turbulent kinetic energy is expected to come from the production term and the dilatation term. The goal would be to solve Eqs. (4.8) and (4.11) for the fluctuating velocity, $\boldsymbol{u}''$, and the full density field, ρ. This, however, presents subtle challenges.

From Eq. (4.7), the dilatation term (i.e. the divergence of the Favre-averaged velocity) can be calculated as $\nabla \cdot \widetilde{\boldsymbol{u}} = -\widetilde{\boldsymbol{u}} \cdot \nabla\overline{\rho}/\overline{\rho}$, from the mean density field. However, the continuity equation needs to be solved in order to calculate the mean density field, for which one needs the dilatation term. This dilatation causes a closure problem, as it implies a two-way coupling between the density and velocity field. Hence, the Favre-averaged velocity should be decomposed further, so that the dilatational part can be resolved in the simulation, and not added as a source term. This velocity decomposition is described in the consequent section.

4.5 Helmholtz decomposition of mean velocity

The Favre-averaged velocity, $\widetilde{\boldsymbol{u}}$, is split using a Helmholtz decomposition into its solenoidal part, $\widetilde{\boldsymbol{u}}^s$, and its dilatational part, $\widetilde{\boldsymbol{u}}^d$, i.e., $\widetilde{\boldsymbol{u}} = \widetilde{\boldsymbol{u}}^s + \widetilde{\boldsymbol{u}}^d$, such that $\nabla \cdot \widetilde{\boldsymbol{u}}^s = 0$ and $\nabla \times \widetilde{\boldsymbol{u}}^d = \boldsymbol{0}$. Helmholtz decomposition offers an infinite number of choices for the two velocity fields shifted by a constant. As will be discussed later, the solenoidal velocity at the averaged flame location, $\widetilde{\boldsymbol{u}}^s(\boldsymbol{x_F})$ will be chosen based on simulation requirements.

The instantaneous velocity field is decomposed as $\boldsymbol{u} = \boldsymbol{u^i} + \boldsymbol{u^r}$, where $\boldsymbol{u^r} = \boldsymbol{u''} + \widetilde{\boldsymbol{u}}^d$ is the resolved part of the velocity field, and $\boldsymbol{u^i} = \widetilde{\boldsymbol{u}}^s$ is the imposed part of the velocity field, which is divergence-free.

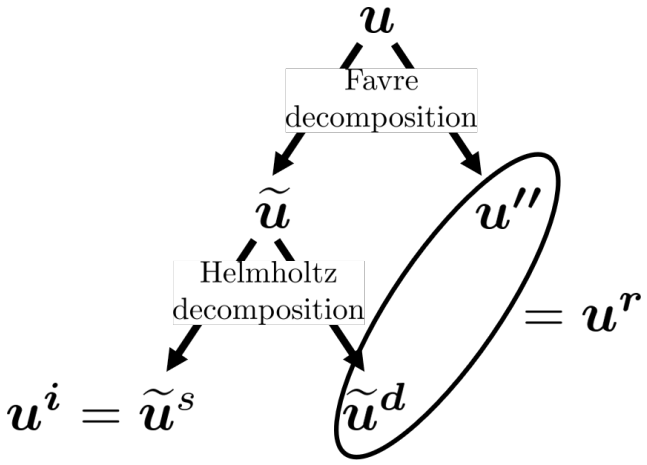

Figure 4.2: Velocity decomposition of the instantaneous velocity field, $\boldsymbol{u}$, into the imposed scales, $\boldsymbol{u^i}$, and the resolved scales, $\boldsymbol{u^r}$.

The continuity equation (Eq. (4.1)) then becomes

$$\frac{\partial \rho}{\partial t} + \nabla \cdot (\rho \boldsymbol{u^r}) = -\nabla \cdot (\rho \boldsymbol{u^i}) = -\boldsymbol{u^i} \cdot \nabla \rho \tag{4.12}$$

where the term, $-\boldsymbol{u^i} \cdot \nabla\rho$, corresponds to the advection by the imposed flow. The ensemble average of this equation gives,

$$\frac{\partial\overline{\rho}}{\partial t} + \nabla \cdot (\overline{\rho\boldsymbol{u^r}}) = -\boldsymbol{u^i} \cdot \nabla\overline{\rho}, \tag{4.13}$$

where, by definition, the gradient of the mean density is identically zero in the unburnt and burnt regions. It is only non-zero in the perpendicular direction through the flame. At the flame front ($\boldsymbol{x_F}$), the perpendicular component of the imposed velocity is chosen to be zero, $u^i_\perp(\boldsymbol{x_F}) = 0$, which implies at the flame location, the right hand side of Eq. 4.13 is zero and $\widetilde{u^r}_\perp(\boldsymbol{x_F}) = \widetilde{u}_\perp(\boldsymbol{x_F})$. Since $\boldsymbol{u^i}$ is dilatation-free by definition, $u^i_\perp = 0$ applies through the flame. In summary, the additional term on the right hand side is zero in the unburnt, burnt, and through the flame, which implies it is zero everywhere, and Eq. (4.13) becomes

$$\nabla \cdot (\overline{\rho\boldsymbol{u^r}}) = 0. \tag{4.14}$$

The momentum equation (Eq. (4.2)) becomes,

$$\begin{aligned}\frac{\partial}{\partial t}(\rho\boldsymbol{u^r}) + \nabla \cdot (\rho\boldsymbol{u^r} \otimes \boldsymbol{u^r}) = -\nabla p + \nabla \cdot \underline{\underline{\boldsymbol{\tau^r}}} - \frac{\partial}{\partial t}(\rho\boldsymbol{u^i}) - \nabla \cdot (\rho\boldsymbol{u^i} \otimes \boldsymbol{u^i}) \\ - \nabla \cdot (\rho\boldsymbol{u^i} \otimes \boldsymbol{u^r}) - \nabla \cdot (\rho\boldsymbol{u^r} \otimes \boldsymbol{u^i}) + \nabla \cdot \underline{\underline{\boldsymbol{\tau^i}}}.\end{aligned} \tag{4.15}$$

Some of the additional terms can be expanded using the fact that the imposed velocity is time-independent and divergence-free,

$$-\frac{\partial}{\partial t}(\rho\boldsymbol{u^i}) = -\boldsymbol{u^i}\frac{\partial\rho}{\partial t}$$

$$-\nabla \cdot (\rho\boldsymbol{u^i} \otimes \boldsymbol{u^i}) = -\boldsymbol{u^i}\nabla \cdot (\rho\boldsymbol{u^i}) - \rho\boldsymbol{u^i} \cdot \underline{\underline{\nabla\boldsymbol{u^i}}}$$

$$-\nabla \cdot (\rho\boldsymbol{u^i} \otimes \boldsymbol{u^r}) = -\boldsymbol{u^i}\nabla \cdot (\rho\boldsymbol{u^r}) - \rho\boldsymbol{u^r} \cdot \underline{\underline{\nabla\boldsymbol{u^i}}}$$

$$-\nabla \cdot (\rho\boldsymbol{u^r} \otimes \boldsymbol{u^i}) = -\rho\boldsymbol{u^r}(\nabla \cdot \boldsymbol{u^i}) - \boldsymbol{u^i} \cdot \underline{\underline{\nabla(\rho\boldsymbol{u^r})}} = -\boldsymbol{u^i} \cdot \underline{\underline{\nabla(\rho\boldsymbol{u^r})}}$$

$$-\boldsymbol{u^i}\frac{\partial\rho}{\partial t} - \boldsymbol{u^i}\nabla \cdot (\rho\boldsymbol{u^i}) - \boldsymbol{u^i}\nabla \cdot (\rho\boldsymbol{u^r}) = -\boldsymbol{u^i}\left(\frac{\partial\rho}{\partial t} + \nabla \cdot (\rho\boldsymbol{u})\right) = 0$$

After simplifying using Eq. (4.12), Eq. (4.15) becomes

$$\frac{\partial}{\partial t}(\rho\boldsymbol{u^r}) + \nabla \cdot (\rho\boldsymbol{u^r} \otimes \boldsymbol{u^r}) = -\nabla p + \nabla \cdot \underline{\underline{\boldsymbol{\tau^r}}} - \rho\boldsymbol{u^r} \cdot \underline{\underline{\nabla\boldsymbol{u^i}}} - \boldsymbol{u^i} \cdot \underline{\underline{\nabla(\rho\boldsymbol{u^r})}} - \rho\boldsymbol{u^i} \cdot \underline{\underline{\nabla\boldsymbol{u^i}}} + \nabla \cdot \underline{\underline{\boldsymbol{\tau^i}}}. \tag{4.16}$$

The ensemble average of this equation gives,

$$\nabla \cdot (\overline{\rho\boldsymbol{u^r} \otimes \boldsymbol{u^r}}) = -\nabla\overline{p} + \nabla \cdot \underline{\underline{\overline{\boldsymbol{\tau^r}}}} - \overline{\rho\boldsymbol{u^r}} \cdot \underline{\underline{\nabla\boldsymbol{u^i}}} - \boldsymbol{u^i} \cdot \underline{\underline{\nabla\left(\overline{\rho\boldsymbol{u^r}}\right)}} - \overline{\rho}\boldsymbol{u^i} \cdot \underline{\underline{\nabla\boldsymbol{u^i}}} + \nabla \cdot \underline{\underline{\overline{\boldsymbol{\tau^i}}}}. \tag{4.17}$$

The pressure field is decomposed into its mean and its fluctuations, ($\nabla p^i = \nabla \overline{p}$ and $\nabla p^r = \nabla p'$) as in Section 4.4. The mean pressure gradient can be removed by subtracting the mean momentum equation (Eq. (4.17)) from Eq. (4.16), which further changes the momentum equation to

$$\frac{\partial}{\partial t}(\rho \boldsymbol{u}^r) + \nabla \cdot (\rho \boldsymbol{u}^r \otimes \boldsymbol{u}^r) = -\nabla p^r + \nabla \cdot \underline{\underline{\boldsymbol{\tau}^r}} - \left(\rho \boldsymbol{u}^r - \overline{\rho \boldsymbol{u}^r}\right) \cdot \underline{\underline{\nabla \boldsymbol{u}^i}} - \boldsymbol{u}^i \cdot \underline{\underline{\nabla \left(\rho \boldsymbol{u}^r - \overline{\rho \boldsymbol{u}^r}\right)}} - \rho' \boldsymbol{u}^i \cdot \underline{\underline{\nabla \boldsymbol{u}^i}} + \nabla \cdot \left(\underline{\underline{\boldsymbol{\tau}^i}} - \underline{\overline{\boldsymbol{\tau}}}\right) + \nabla \cdot \left(\overline{\rho \boldsymbol{u}^r \otimes \boldsymbol{u}^r}\right), \quad (4.18)$$

where $-\left(\rho \boldsymbol{u}^r - \overline{\rho \boldsymbol{u}^r}\right) \cdot \underline{\underline{\nabla \boldsymbol{u}^i}}$ is the turbulence production term and $-\boldsymbol{u}^i \cdot \underline{\underline{\nabla \left(\rho \boldsymbol{u}^r - \overline{\rho \boldsymbol{u}^r}\right)}}$ is the advection by the imposed flow. Note that the average $\overline{\rho \boldsymbol{u}^r}$ is zero in the direction parallel to the mean flame front. $\nabla \cdot \left(\overline{\rho \boldsymbol{u}^r \otimes \boldsymbol{u}^r}\right)$ is the divergence of the Reynolds stress, $\nabla \cdot \left(\underline{\underline{\boldsymbol{\tau}^i}} - \underline{\overline{\boldsymbol{\tau}}}\right)$ is the difference between the viscous stress of the imposed flow and the mean stress, and $-\rho' \boldsymbol{u}^i \cdot \underline{\underline{\nabla \boldsymbol{u}^i}}$ is present only near the flame, where density fluctuates. The magnitude of $\boldsymbol{u}^i \cdot \underline{\underline{\nabla \boldsymbol{u}^i}}$ depends on the reacting flow configuration. After the velocity decomposition, Eq. (4.3) and Eq. (4.5) become

$$\frac{\partial}{\partial t}(\rho Y_i) + \nabla \cdot (\rho \boldsymbol{u}^r Y_i) + \nabla \cdot \boldsymbol{j}_i - \dot{\omega}_i = -\boldsymbol{u}^i \cdot \nabla(\rho Y_i), \quad (4.19)$$

and

$$\frac{\partial}{\partial t}(\rho T) + \nabla \cdot (\rho \boldsymbol{u}^r T) - \frac{1}{c_p} \nabla \cdot (\lambda \nabla T) - \dot{\omega}_T + \frac{1}{c_p} \sum_i c_{p,i} \boldsymbol{j}_i \cdot \nabla T = -\boldsymbol{u}^i \cdot \nabla(\rho T), \quad (4.20)$$

with the additional terms corresponding to advection by the imposed flow.

4.6 Periodicity and continuity correction

For the resolved part of the velocity field, the Cartesian directions, x, y, and z are chosen along the perpendicular direction, $\perp$, and the parallel directions, $\parallel$ and $|$, respectively. The velocity components along the three directions are given by $u = u_\perp$, $v = u_\parallel$, and $w = u_|$. The intent is to use periodic boundary conditions along y and z, parallel to the average flame front. But in reality, the velocity field is not periodic parallel to the flame. A necessary (but not sufficient) condition for using periodic boundary conditions is that the mean and root mean square (rms) of the velocity field are invariant in the periodic directions.

As mentioned previously, the parallel components of the mean velocity is zero at the flame location, and using the small domain assumption, it is zero throughout. For the perpendicular component, it can be calculated from Eq. (4.14), that $\partial \left(\overline{\rho u^r}\right) / \partial x =$

0. Hence, the mean momentum in the x direction does not vary along x, and this implies that the mass flux per unit area along x, $J(x) = (1/A)\int_y\int_z u(x,y,z)\,dy\,dz$ is constant throughout, and can be calculated as $J = \text{const} = \overline{\rho}(\boldsymbol{x_F})\,\widetilde{u}(\boldsymbol{x_F})$. The transport equation for the fuel mass fraction is given by,

$$\frac{\partial}{\partial t}(\rho Y_F) + \nabla\cdot(\rho \boldsymbol{u}^{\boldsymbol{r}} Y_F) + \nabla\cdot\boldsymbol{j}_F - \dot{\omega}_F = 0, \tag{4.21}$$

and integrating this equation over a finite volume around the flame location in statistically stationary reacting flows gives

$$\int_y\int_z \overline{\rho\,u^r}(\boldsymbol{x_F})\,Y_{F,u}\,dy\,dz = -\int_x\int_y\int_z \dot{\omega}_F\,dx\,dy\,dz,$$

Based on mass balance of the fuel mass fraction at the flame location in statistically stationary reacting flows, the mass flux per unit area perpendicular to the flame front, $\overline{\rho u^r} = \overline{\rho}(\boldsymbol{x_F})\,\widetilde{u}(\boldsymbol{x_F})$, balances the mean turbulent flame speed, $\rho_u\,\overline{S_T}(\boldsymbol{x_F})$, where S_T is the turbulent flame speed defined by $S_T = \frac{1}{\rho_u Y_{F,u} A}\int_x\int_y\int_z dot\omega_F\,dx\,dy\,dz,$.

The root mean square of the velocity field is usually not constant in reacting flows, but the rms of the resolved velocity needs to be invariant in the parallel directions, so that periodic boundary conditions can be used. Hence, the velocity components are normalized to ensure that their second order statistics are constant along the parallel directions, just like in Rah *et al.* [17] and in Section 2.2.3.

The three components of the velocity, u, v, and w are decomposed using their spatial dependence in the two parallel directions,

$$u^r = u^* f_u(y)\,g_u(z), \quad v^r = v^* f_v(y)\,g_v(z), \quad w^r = w^* f_w(y)\,g_w(z), \tag{4.22}$$

where f_v and g_v are the time-independent spatial dependences of the magnitudes of v, $f_v(y) = \sqrt{\widetilde{v^{r2}}(y)\Big/\widetilde{v^{r2}}(y_F)}$ and $g_v(z) = \sqrt{\widetilde{v^{r2}}(z)\Big/\widetilde{v^{r2}}(z_F)}$, and so on for f_u, g_u, f_w, and g_w. At the flame location, $\boldsymbol{x_F}$, $f_i = g_i = 1$, and $\boldsymbol{u}^{\boldsymbol{r}}$ and $\boldsymbol{u}^*$ have the same magnitudes.

Rescaling the velocity field for periodicity generates additional terms in both continuity and momentum equations. The only change in the continuity equation comes from the convective term, $\nabla\cdot(\rho\boldsymbol{u}^{\boldsymbol{r}})$. At the flame location, this term becomes $\nabla\cdot(\rho\boldsymbol{u}^{\boldsymbol{r}}) = \nabla\cdot(\rho\boldsymbol{u}^{\boldsymbol{*}}) + \rho v^* f_v'(y_F) + \rho w^* g_w'(z_F)$. Ideally, there should be no additional terms in the continuity equation due to the rescaling. Hence, a continuity correction, $\exp\left[-f_v'(y_F)\,(y - y_F)\right]$, is included for v^r and a similar correction is

added for w^r. The final rescaling after periodicity and continuity correction is given by,

$$u^r = u^* f_u(y) g_u(z),$$
$$v^r = v^* f_v(y) g_v(z) \exp\left[-f_v'(y_F)(y - y_F)\right],$$
$$w^r = w^* f_w(y) g_w(z) \exp\left[-g_w'(z_F)(z - z_F)\right].$$

From the transformation, the gradients of the y component of the velocity, v, are given by $\partial v^r/\partial y = \partial v^*/\partial y$, $\partial v^r/\partial x = \partial v^*/\partial x$, and $\partial v^r/\partial z = \partial v^*/\partial z + v^* g_v'(z_F)$. The gradients of the other components of the velocity field can be calculated in a similar fashion.

Rescaling the velocity field for periodicity and continuity results in additional terms in the momentum equation. The terms in Eq. (4.18) that are affected by the transformation are the convective term, $\nabla \cdot (\rho \boldsymbol{u}^r \otimes \boldsymbol{u}^r) = \boldsymbol{u}^r \nabla \cdot (\rho \boldsymbol{u}^r) + \rho \boldsymbol{u}^r \cdot \underline{\underline{\nabla \boldsymbol{u}^r}}$, the advection by the imposed flow, $-\boldsymbol{u}^i \cdot \underline{\underline{\nabla \left(\rho \boldsymbol{u}^r - \overline{\rho \boldsymbol{u}^r}\right)}}$, and the divergence of the Reynolds stress terms, $\nabla \cdot (\overline{\rho \boldsymbol{u}^r \otimes \boldsymbol{u}^r})$. Considering just the rescaling of v^r, the terms affected by the rescaling become,

$$\boldsymbol{u}^r \nabla \cdot (\rho \boldsymbol{u}^r) = \boldsymbol{u}^* \nabla \cdot (\rho \boldsymbol{u}^*),$$
$$\rho \boldsymbol{u}^r \cdot \underline{\underline{\nabla \boldsymbol{u}^r}} = \rho \boldsymbol{u}^* \cdot \underline{\underline{\nabla \boldsymbol{u}^*}} + g_v'(z_F)\, \rho w^* v^*\, \boldsymbol{e_y},$$
$$-\boldsymbol{u}^i \cdot \underline{\underline{\nabla \left(\rho \boldsymbol{u}^r - \overline{\rho \boldsymbol{u}^r}\right)}} = -\boldsymbol{u}^i \cdot \underline{\underline{\nabla \left(\rho \boldsymbol{u}^* - \overline{\rho \boldsymbol{u}^*}\right)}} - g_v'(z_F)\, w^i \left(\rho v^* - \overline{\rho v^*}\right) \boldsymbol{e_y},$$
$$\nabla \cdot (\overline{\rho \boldsymbol{u}^r \otimes \boldsymbol{u}^r}) = \nabla \cdot (\overline{\rho \boldsymbol{u}^* \otimes \boldsymbol{u}^*}) + g_v'(z_F)\, \overline{\rho w^* v^*}\, \boldsymbol{e_y}.$$

All the additional terms in the momentum equation due to the rescaling are either linear or quadratic in velocity. These terms are combined and can be organized into linear terms of the form $-\left(\rho \boldsymbol{u}^* - \overline{\rho \boldsymbol{u}^*}\right) \cdot \underline{\underline{A_L(\boldsymbol{u}^i)}}$ and quadratic terms of the form $-\rho \boldsymbol{u}^* \cdot \underline{\underline{A_Q(\boldsymbol{u}^*)}} - \overline{\rho \boldsymbol{u}^* \cdot \underline{\underline{A_Q(\boldsymbol{u}^*)}}}$. By construction, $\boldsymbol{u}^*$ is homogeneous along the two parallel directions, and $\nabla \cdot (\overline{\rho \boldsymbol{u}^* \otimes \boldsymbol{u}^*}) = d(\overline{\rho u^* \boldsymbol{u}^*})/dx + \left(\overline{\boldsymbol{u}^* \otimes \boldsymbol{u}^*}\right)_{\|,|} \cdot \nabla \overline{\rho} = d(\overline{\rho u^* \boldsymbol{u}^*})/dx$. The momentum equation from Eq. (4.18) after rescaling, transforms into

$$\begin{aligned}\frac{\partial}{\partial t}(\rho \boldsymbol{u}^*) + \nabla \cdot (\rho \boldsymbol{u}^* \otimes \boldsymbol{u}^*) = &-\nabla p^r + \nabla \cdot \underline{\underline{\boldsymbol{\tau}^*}} - \left(\rho \boldsymbol{u}^* - \overline{\rho \boldsymbol{u}^*}\right) \cdot \underline{\underline{\nabla \boldsymbol{u}^i}} \\ &- \boldsymbol{u}^i \cdot \underline{\underline{\nabla \left(\rho \boldsymbol{u}^* - \overline{\rho \boldsymbol{u}^*}\right)}} - \rho' \boldsymbol{u}^i \cdot \underline{\underline{\nabla \boldsymbol{u}^i}} + \nabla \cdot \left(\underline{\underline{\boldsymbol{\tau}^i}} - \underline{\underline{\overline{\boldsymbol{\tau}}}}\right) + d(\overline{\rho u^* \boldsymbol{u}^*})/dx \\ &- \left(\rho \boldsymbol{u}^* - \overline{\rho \boldsymbol{u}^*}\right) \cdot \underline{\underline{A_L(\boldsymbol{u}^i)}} - \left(\rho \boldsymbol{u}^* \cdot \underline{\underline{A_Q(\boldsymbol{u}^*)}} - \overline{\rho \boldsymbol{u}^* \cdot \underline{\underline{A_Q(\boldsymbol{u}^*)}}}\right). \quad (4.23)\end{aligned}$$

4.7 Source terms

After the velocity decomposition and rescaling, the transport equations that $\boldsymbol{u}^*$ verify are the same as the original Navier-Stokes equation with additional source terms. The additional terms in the momentum equation after the final transformation are

1. $-\left(\rho\boldsymbol{u}^* - \overline{\rho\boldsymbol{u}^*}\right) \cdot \underline{\underline{\nabla \boldsymbol{u}^i}}$, which is the linear production term, that produces turbulent kinetic energy,

2. $-\boldsymbol{u}^i \cdot \nabla \underline{\underline{\left(\rho\boldsymbol{u}^* - \overline{\rho\boldsymbol{u}^*}\right)}}$, which represents convection by the imposed velocity in the direction parallel to the mean flame front,

3. $-\rho'\boldsymbol{u}^i \cdot \underline{\underline{\nabla \boldsymbol{u}^i}}$, which influences the turbulent kinetic energy near the flame, where the density fluctuates and $\overline{\rho'\boldsymbol{u}^*}$ is not zero. $\boldsymbol{u}^i \cdot \underline{\underline{\nabla \boldsymbol{u}^i}}$ is expected to be large in reacting flows with strong mean gradients of pressure perpendicular to the flame, for instance, in swirling jet flames. Henceforth, this term is referred to as the "pressure" term.

4. $\nabla \cdot \left(\underline{\underline{\boldsymbol{\tau}^i}} - \overline{\underline{\underline{\boldsymbol{\tau}}}}\right)$, the difference between the gradient of the viscous stress of the imposed scales, $\underline{\underline{\boldsymbol{\tau}^i}}(\mu, \boldsymbol{u}^i)$, and the mean stress, $\overline{\underline{\underline{\boldsymbol{\tau}}}(\mu, \boldsymbol{u})}$. This is the difference between two terms that are very close to each other, and is negligible.

5. $d(\overline{\rho u^* \boldsymbol{u}^*})/dx$ is constant in time, and only present near the flame. This term only contributes to mean pressure gradients and does not contribute to turbulent kinetic energy. Hence this term can be lumped with the mean pressure gradients and omitted in the simulation.

6. $-\left(\rho\boldsymbol{u}^* - \overline{\rho\boldsymbol{u}^*}\right) \cdot \underline{\underline{A_L(\boldsymbol{u}^i)}}$ is a linear forcing term, resulting from the rescaling. This can be combined with the production term, to make a final linear forcing term, $\left(\rho\boldsymbol{u}^* - \overline{\rho\boldsymbol{u}^*}\right) \cdot \underline{\underline{\boldsymbol{A_c}}}$, where $\underline{\underline{\boldsymbol{A_c}}} = -\underline{\underline{\nabla \boldsymbol{u}^i}} - \underline{\underline{A_L}}$.

7. $-\left(\rho\boldsymbol{u}^* \cdot \underline{\underline{A_Q(\boldsymbol{u}^*)}} - \overline{\rho\boldsymbol{u}^* \cdot \underline{\underline{A_Q(\boldsymbol{u}^*)}}}\right)$, which is a non-linear term due to the rescaling. These terms generate turbulence proportional to triple correlations of velocity, which are generally small and have limited effects on the turbulence statistics as seen in DNS 3b in Section 2.5.1. Hence these terms are neglected.

The final momentum equation for the resolved quantities is given by

$$\frac{\partial}{\partial t}(\rho \boldsymbol{u}^*) + \nabla \cdot (\rho \boldsymbol{u}^* \otimes \boldsymbol{u}^*) = -\nabla p^r + \nabla \cdot \underline{\underline{\boldsymbol{\tau}^*}} + \left(\rho \boldsymbol{u}^* - \overline{\rho \boldsymbol{u}^*}\right) \cdot \underline{\underline{A_c(\boldsymbol{u}^i)}} - \boldsymbol{u}^i \cdot \underline{\underline{\nabla \left(\rho \boldsymbol{u}^* - \overline{\rho \boldsymbol{u}^*}\right)}} - \rho' \boldsymbol{u}^i \cdot \underline{\underline{\nabla \boldsymbol{u}^i}}, \quad (4.24)$$

where the additional terms can be calculated from the imposed mean velocity, $\boldsymbol{u}^i$.

4.8 Conclusions

The turbulence forcing techniques developed for incompressible turbulence have been extended to reacting flows. Reynolds decomposition of the velocity field used in the previous chapters is initially replaced by a Favre decomposition. The dilatation due to the flame poses a problem, which is resolved by performing an additional Helmholtz decomposition on the Favre-averaged velocity field. The velocity field is rescaled for periodicity and continuity, which results in additional linear and quadratic source terms. Once again, the final transport equations are like the Navier-Stokes equation with additional source terms. The additional source terms in the momentum equation are discussed and the terms that significantly affect turbulent reacting flows are the production term, advection term, and the pressure term.

Chapter 5

DIRECT NUMERICAL SIMULATIONS OF TURBULENT FLAMES UNDER DIFFERENT TURBULENT CONDITIONS

The final momentum equation for the resolved quantities from Chapter 4 is given by

$$\frac{\partial}{\partial t}(\rho \boldsymbol{u}^*) + \nabla \cdot (\rho \boldsymbol{u}^* \otimes \boldsymbol{u}^*) = -\nabla p^r + \nabla \cdot \underline{\underline{\boldsymbol{\tau}^*}} + \left(\rho \boldsymbol{u}^* - \overline{\rho \boldsymbol{u}^*}\right) \cdot \underline{\underline{A_c(\boldsymbol{u}^i)}} - \boldsymbol{u}^i \cdot \underline{\underline{\nabla \left(\rho \boldsymbol{u}^* - \overline{\rho \boldsymbol{u}^*}\right)}} - \rho' \boldsymbol{u}^i \cdot \underline{\underline{\nabla \boldsymbol{u}^i}}, \quad (5.1)$$

where $\left(\rho \boldsymbol{u}^* - \overline{\rho \boldsymbol{u}^*}\right) \cdot \underline{\underline{A_c(\boldsymbol{u}^i)}}$ is the production term, $\underline{\underline{A_c}}$ is the forcing matrix, $-\boldsymbol{u}^i \cdot \underline{\underline{\nabla \left(\rho \boldsymbol{u}^* - \overline{\rho \boldsymbol{u}^*}\right)}}$ is the advection by the imposed velocity, and $-\rho' \boldsymbol{u}^i \cdot \underline{\underline{\nabla \boldsymbol{u}^i}}$ is the pressure term. The impact of each of these terms can be analyzed by including extreme versions of each of these terms in the turbulent flame simulations.

Different turbulent flame simulations are performed to observe the impact of the different terms in Eq. 4.24. Section 5.1 discusses the numerical approach. Then, results from two simulations of turbulent flames using shear forcing and isotropic turbulence forcing are compared in Section 5.2. The effects of the shear convection are observed in Section 5.3 and the impact of the pressure term is analyzed in Section 5.4. Finally, Section 5.5 details the conclusions drawn about the effects of the large scale flow on the turbulent flames.

5.1 Numerical approach

5.1.1 Forcing matrix

Previous DNS of turbulent flames with linear forcing assumed the proportionality matrix, $\underline{\underline{A_c}}$ to be a diagonal matrix [2, 10, 18, 19, 11] just like Lundgren suggested [14]. The forcing term for this isotropic case is given by [10, 18, 19, 11]

$$\boldsymbol{f}_{iso} = A \frac{k_o}{k} (\rho \boldsymbol{u} - \overline{\rho \boldsymbol{u}}), \quad (5.2)$$

where A is the isotropic forcing constant, $k = \widetilde{\boldsymbol{u}'' \cdot \boldsymbol{u}''}/2$ is the Favre-averaged turbulent kinetic energy, and k_o is the expected turbulent kinetic energy. The factor $\frac{k_o}{k}$ is added to help with the stability of the simulations [3]. This factor maintains constant production of turbulent kinetic energy throughout the domain, $P = 2Ak_o$, where forcing is applied. k_o/k is often close to 1 for the isotropic case.

The proportionality matrix $\underline{\underline{A_c}}$ could in fact be calculated from experiments of turbulent flames. Unfortunately, this would require access to 3D velocity data. Instead, the proportionality matrix is calculated at the flame location from recent results of large eddy simulations (LES) of a reacting jet [22]. The mean velocity gradients are calculated at the flame location 30 diameters from the jet inlet, where the flame normal is close to the radial direction (6^o) as,

$$\underline{\underline{A_c}} = \underline{\underline{\nabla \boldsymbol{u}^i}} = - \begin{bmatrix} \frac{\partial u_Z^i}{\partial Z} & \frac{\partial u_Z^i}{\partial R} & 0 \\ \frac{\partial u_R^i}{\partial Z} & \frac{\partial u_R^i}{\partial R} & 0 \\ 0 & 0 & \frac{u_R^i}{R} \end{bmatrix} = B_C \begin{bmatrix} -0.023 & 1 & 0 \\ -0.006 & 0.012 & 0 \\ 0 & 0 & 0.011 \end{bmatrix}. \tag{5.3}$$

The calculations reveal that the off-diagonal shear strain rate element $\partial u_Z^i / \partial R$ is the largest element of the matrix $\underline{\underline{A_c}}$ by two orders of magnitude. In comparison, the other elements of the matrix are negligible, and the shear turbulence forcing vector may be approximated by

$$\boldsymbol{f}_{shear} = B \frac{k_o}{k} \left(\rho u_\perp - \overline{\rho u}_\perp \right) \boldsymbol{e}_\parallel, \tag{5.4}$$

where $B = \partial \widetilde{u}_X / \partial R$ is the shear forcing constant. The forcing is only in the $y(\parallel)$ direction, linear with the momentum fluctuations in the $x(\perp)$ direction. The $\frac{k_o}{k}$ is included in the shear simulations as well, and is very close to 1.

In most cases, the proportionality matrix would be a combination of small diagonal elements and a dominant off-diagonal shear strain rate element. Hence, the forcing matrix containing only the off-diagonal element and the forcing matrix with only diagonal elements can be seen as the two extreme cases of turbulence forcing. The diagonal forcing matrix has been used extensively already in previous studies [18, 19, 11, 10, 2] and the present study focuses on the off-diagonal forcing matrix and the comparison between the two.

5.1.2 Advection

The most dominant part of the advection by the imposed velocity is the shear convection, while the other parts correspond to bulk motion in the parallel directions, and those have no effects on the flow due to the periodic boundary conditions. Recall that $\boldsymbol{u}_\perp^{\boldsymbol{i}} = 0$ at the flame location, so there is no bulk velocity in the perpendicular

direction. The effects of the shear convection on incompressible turbulence has already been analyzed in Section 3.6.2. The imposed mean velocity for shear convection is given by $\boldsymbol{u^i} = \boldsymbol{V} = V\boldsymbol{e_y}$, which is plotted in Fig. 5.1. To be consistent with the shear production term, the imposed velocity has a gradient of $-B$ between 3.5 L and 7.5 L. The maximum imposed speed, $V_{max} = 2BL$ is much larger than the rms velocity, $u' = 3/2\beta B\ell \sim 0.12BL$, therefore it controls the CFL condition and consequently reduces the time step for a stable simulation. This is the reason shear convection is limited to a portion of width 4 L at the center, and not over the whole domain, which would result in $V_{max} = 5.5BL$.

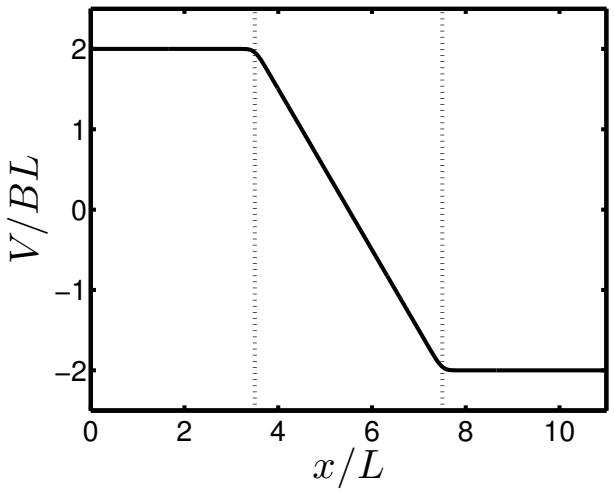

Figure 5.1: Advection velocity profile normalized by the shear forcing constant and domain width.

5.1.3 Pressure term

$-\rho'\boldsymbol{u^i} \cdot \underline{\overline{\nabla \boldsymbol{u^i}}} = \rho'\boldsymbol{\mathcal{P}}$ is the pressure term (or the inertial term of the imposed velocity), which is most significant in flames with strong mean pressure gradients. For instance, in swirling jet flames,

$$\boldsymbol{\mathcal{P}} = -\boldsymbol{u^i} \cdot \underline{\overline{\nabla \boldsymbol{u^i}}} \simeq \widetilde{u}_\theta^2/R_F\ \boldsymbol{e_R},$$

where R_F is the radial location of the flame from the axis. The flame normal is in the radial direction, hence $\boldsymbol{e}_\perp = \boldsymbol{e_R}$. The mean azimuthal velocity is given by, $\widetilde{u}_\theta = SU_o$, where S is the swirl number, and U_o is the centerline velocity. Hence,

the pressure term is calculated as $\rho'\mathcal{P} = \rho' S^2 U_o^2 / R_F \boldsymbol{e}_\perp$. An extreme value of the pressure term is chosen for this simulation, corresponding to a maximum swirl number of 0.5. The ratio of the centerline velocity to the flame location can be calculated from the shear forcing constant, B, using the relation, $B = 0.586 U_o / R_F$, and the centerline velocity can be calculated from the expected kinetic energy for the isotropic case, using the relation, $k_o = 0.052\, U_o^2$. These are estimates from the half-width of a round jet, as these values are not easily available for a swirling reacting jet.

5.1.4 Governing equations

The low Mach number Navier-Stokes equations solved in the simulations of the current study are given by

$$\frac{\partial \rho}{\partial t} + \nabla \cdot (\rho \boldsymbol{u}) = -\boldsymbol{V} \cdot \nabla \rho, \tag{5.5}$$

$$\frac{\partial}{\partial t}(\rho \boldsymbol{u}) + \nabla \cdot (\rho \boldsymbol{u} \otimes \boldsymbol{u}) = -\nabla p + \nabla \cdot \tau + \boldsymbol{f} - \boldsymbol{V} \cdot \nabla(\rho \boldsymbol{u}) + \rho' \boldsymbol{\mathcal{P}}, \tag{5.6}$$

where $\boldsymbol{f}$ is the forcing vector, calculated in Eq. (5.2) and (5.4) for the two turbulence forcing techniques.

$$\frac{\partial}{\partial t}(\rho Y_i) + \nabla \cdot (\rho \boldsymbol{u} Y_i) = -\nabla \cdot \boldsymbol{j}_i + \dot{\omega}_i - \boldsymbol{V} \cdot \nabla(\rho Y_i), \tag{5.7}$$

$$\frac{\partial}{\partial t}(\rho T) + \nabla \cdot (\rho \boldsymbol{u} T) = \nabla \cdot (\rho \alpha \nabla T) + \dot{\omega}_T - \frac{1}{c_p} \sum_i c_{p,i} \boldsymbol{j}_i \cdot \nabla T + \frac{\rho \alpha}{c_p} \nabla c_p \cdot \nabla T - \boldsymbol{V} \cdot \nabla(\rho T). \tag{5.8}$$

The dynamic viscosities of the species, μ_i, are calculated using standard kinetic theory [9], and the viscosity of the mixture is calculated using a modified form of Wilke's formula [10]. The thermal conductivities of the species, λ_i, are calculated by using a modified form of Eucken's formula [7], and the thermal conductivity of the mixture is computed with the method suggested by Mathur *et al.* [15] The equation of state used to bring closure to this system of equations is given by

$$p_0 = \rho R T \sum_i \frac{Y_i}{W_i} \tag{5.9}$$

where p_0 is the thermodynamic pressure, R is the universal gas constant, and W_i is the molecular weight of species i.

The production rates of the species and enthalpy are calculated using a reduced $n\text{–}C_7H_{16}$ combustion model with 35 species and 217 elementary reactions (which counts for forward and backward reactions separately) [1].

Equations (5.5) - (4.6) are solved using NGA [6], a finite difference solver with an energy-conserving scheme on a staggered grid, designed to simulate variable density low Mach number turbulent flows. The scheme is second order accurate in space, and a semi-implicit second order Crank-Nicolson scheme is used for time integration [16]. The scalar transport scheme used is the third order BQUICK [8] scheme, that ensures that scalars stay within bounds. For the advection simulation, the shear convection is applied using central difference in the momentum equation and continuity equation, and using an upwind scheme for scalar transport, with implicit corrections for time integration of the momentum and scalar transport equations.

5.1.5 Computational domain

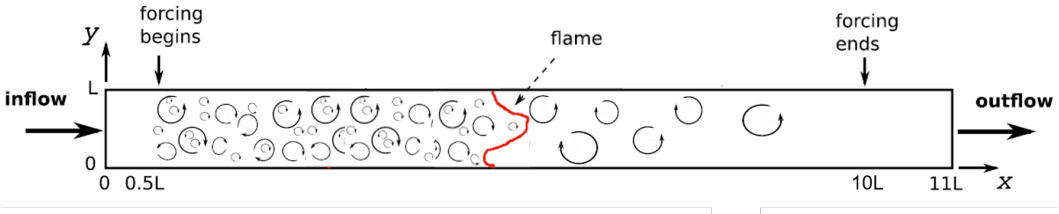

Figure 5.2: Schematic of the computational domain for the turbulent flame simulations, adapted from Savard *et al.* [19]

The simulation utilizes the same flow configuration used in previous work to simulate turbulent flames [2, 10, 18, 19, 11], see Fig. 5.2. The computational domain is meshed with a uniform grid, with equal spacing in the three directions, $\Delta x = \Delta y = \Delta z \simeq 1.6\,\eta_u$, where $\eta_u = \left(\nu_u^3/\epsilon^3\right)^{1/4}$ is the Kolomogorov length scale in the unburnt side. Due to the increased turbulence intensity, the pressure simulations are performed in a finer grid (by a factor of 1.5 in each direction) to capture the turbulent small scales. The domain is periodic in the y and z direction, which results in statistical homogeneity along these directions. Hence ensemble averages can be replaced by planar averages, calculated as

$$\overline{a}(x,t) = \frac{1}{L^2}\int_y\int_z a(x,y,z,t)\,dy\,dz. \tag{5.10}$$

The domain has an inflow and an outflow in the x direction. When the mean velocity of the inflow is matched with the turbulent flame speed, the simulation can be performed for long time periods at the statistically stationary state. The average turbulent flame speed is estimated from previously performed similar simulations [10], and is used as the mean velocity for the inflow. Superimposed on

the mean velocity are fields of fluctuating velocities computed from simulations of homogeneous isotropic turbulence at a lower turbulent Reynolds number, so there is no negative velocity at the inflow. The velocity fields are subjected to the forcing scheme between $0.5\,L$ and $10\,L$, such that the turbulent kinetic energy production is fixed through the flame.

The inflow consists of a premixed unburnt mixture of $n-C_7H_{16}$ with air at an equivalence ratio of $\phi = 0.9$ at standard temperature ($T_u = 298$ K) and pressure ($p_0 = 1$ atm) conditions. The simulation parameters for the four different simulations are presented in Table 5.1.

Table 5.1: Simulation parameters of the different cases of turbulent flame simulations

	Isotropic	Shear	Advection	Pressure
Domain size	$11L \times L \times L$			
Grid	$1408 \times 128 \times 128$			$1920 \times 192 \times 192$
$\boldsymbol{f}$	$\boldsymbol{f}_{iso}$	$\boldsymbol{f}_{shear}$	$\boldsymbol{f}_{shear}$	$\boldsymbol{f}_{iso}$
Forcing constant (s^{-1})	$A = 5280$	$B = 22700$	$B = 22700$	$A = 5280$
$\boldsymbol{V}$	0	0	$V\boldsymbol{e_y}$	0
$\mathcal{P}$	0	0	0	$S^2U_o^2/R_F\ \boldsymbol{e_x}$
u'/S_L	16	17	17	25
ℓ/l_F	0.95	1.15	1.15	1.00
$Re_{t,u}$	140	180	180	150
Ka_u	1950	1850	1850	1850

The significant non-dimensional parameters are u'/S_L, ℓ/l_F, Re_t, and Ka_u. u' is the root mean square velocity in the unburnt region and is about 17 times larger than the laminar flame speed, S_L. The laminar flame thickness, l_F is nearly equal to the integral length scale in the unburnt side, defined as $\ell = u'^3/\varepsilon = (2k/3)^{3/2}/\varepsilon$, where $\varepsilon = \overline{\nabla \cdot \boldsymbol{\tau}' \cdot u''}/\overline{\rho}$ is the energy dissipation rate. $Re_t = u'\ell/\nu_u$ is the turbulent Reynolds number in the unburnt region, where ν_u is the kinematic viscosity of the unburnt mixture. The unburnt Karlovitz number is defined as $Ka_u = (l_F/\eta_u)^2 = l_F^2\left(\varepsilon/\nu_u^3\right)^{1/2}$, and the current study simulates turbulent flames at high $Ka_u \simeq 1900$, which means the Kolmogorov length scale is much smaller than the flame thickness. It is important to note that only two of the four non-dimensional parameters are independent.

Turbulent flames are impacted by these non-dimensional parameters [11, 10, 2]. Among them, the unburnt Karlovitz number has been identified in previous studies as the controlling parameter for the impact of turbulence on the chemistry. [10].

Hence, the Karlovitz numbers need to be equal between the simulations that are compared, so the effects of the flow conditions alone can be isolated and analyzed. The expected Karlovitz number for the isotropic and shear simulations can be calculated as,

$$Ka_{o,i} = \frac{l_F^2 \varepsilon^{1/2}}{\nu^{3/2}} = \frac{l_F^2 \sqrt{27} A^{3/2} \ell_i}{\nu^{3/2}}, \tag{5.11}$$

$$Ka_{o,s} = \frac{l_F^2 \varepsilon^{1/2}}{\nu^{3/2}} = \frac{l_F^2 \sqrt{27} B^{3/2} \beta^{3/2} \ell_s}{\sqrt{8} \nu^{3/2}}. \tag{5.12}$$

Equating the two Karlovitz numbers gives the relation, $B = 2A/\beta(\ell_i/\ell_s)^{2/3} \simeq 4.3A$, using the integral length scale values calculated for incompressible simulations in Section 3.6.1.1 ($\ell_i \simeq 0.16\,L$ and $\ell_s \simeq 0.23\,L$). Using these values, the expected turbulent kinetic energy values, $k_{0,i} = 27A^2\ell_i^2/2$ and $k_{0,s} = 27\beta^2 B^2 \ell_s^2/8$ can be calculated. The expected energy dissipation rates are the same for the two cases, $\varepsilon_{0,i} = 27A^3\ell_i^2 = 27\beta^3 B^3 \ell_s^2/8 = \varepsilon_{0,s}$ [3]. These forcing terms calculated here are used between $x = 0.5\,L$ and $x = 10\,L$ in the simulations. The simulations are initialized with the same velocity and scalar fields from DNS of turbulent flames performed by Lapointe and Blanquart [11], at similar turbulence parameters, corresponding to flame B, and the same inflow field is used between the simulations. The different simulation results are compared and contrasted in the following sections.

5.2 Results - Forcing type

Turbulent flame simulations are performed using isotropic forcing (Eq. (5.2)) and shear forcing (Eq. (5.4)). The simulations are performed for 50 eddy turnover times, τ, and averages are calculated after a transient period of 10τ. The effects of the different forcing techniques on chemistry and turbulence are discussed in the following subsections.

5.2.1 Global quantities

2D contours of temperature in the x-y plane are shown in Fig. 5.3 for the two different forcing techniques. In both cases, the turbulent flame structure can be observed near the middle of the domain, around $5.5\,L$. The turbulent flame brush thickness, l_t, is calculated by computing from the peak value of the mean temperature and the temperature difference across the flame, $l_t = (T_b - T_u)/|\nabla\overline{T}|_{max}$. The flame brush thickness for the isotropic case is with $l_t = 1.44\,L$ and slightly smaller for the shear case with $l_t = 1.25\,L$.

The time-averaged planar-averaged kinetic energy and energy dissipation rate are

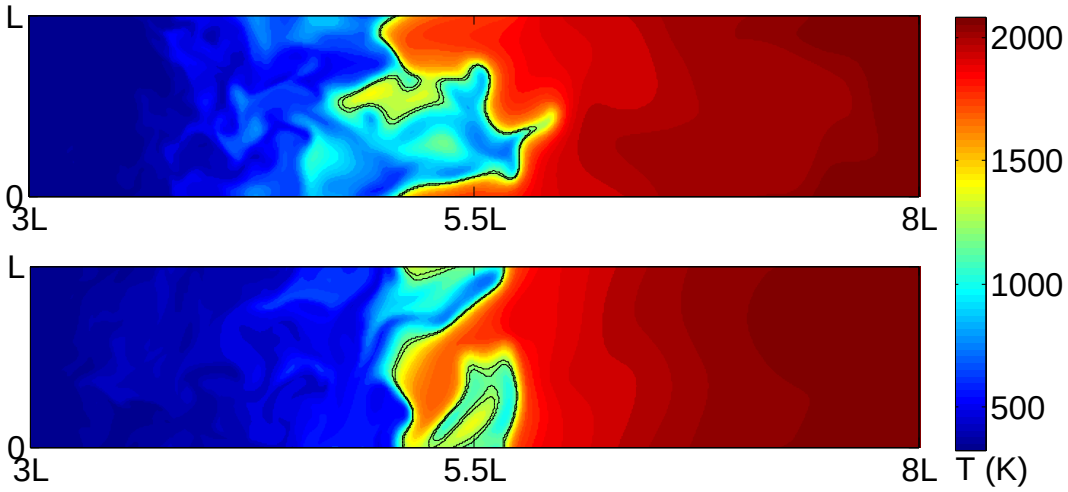

Figure 5.3: Instantaneous temperature contours in the x-y plane for isotropic forcing (top) and shear forcing (bottom). The black curves locate the edges of the reaction zone, corresponding to $T_{\text{peak}} - 30\,K$ and $T_{\text{peak}} + 30\,K$, where T_{peak} is the maximum fuel consumption temperature.

plotted over the domain for the two cases in Fig. 5.4, normalized by their expected values. The two simulations have similar kinetic energy and energy dissipation rate in the unburnt region as seen in Fig. 5.4. The average integral length scale is plotted for the two cases in 5.4c, and $\ell \simeq 0.16L$ for the isotropic forcing throughout and for the shear forcing, $\ell \simeq 0.20L$ in the unburnt side and $\ell \simeq 0.13L$ in the burnt side. The integral length scale for shear turbulence decreases with the drop in Reynolds number, which is consistent with results from Chapter 2 (see DNS 1-4 in Table 2.2).

The turbulent Reynolds number is shown in Fig. 5.5a. The Reynolds number is higher for the shear turbulence case, far away from the flame location. The Reynolds number drops significantly through the flame, due to the increased viscosity, and is comparable to the isotropic case on the burnt side. The Karlovitz number profiles are plotted in Fig. 5.5b. The profiles are very similar for the two simulations, and the Karlovitz number has been successfully matched across the two simulations.

The turbulent flame speed S_T is computed from the fuel consumption rate, $\dot{\omega}_F$ as

$$S_T = \frac{1}{\rho_u Y_{F,u} L^2} \iiint -\dot{\omega}_F \, dV, \tag{5.13}$$

and it is plotted in Fig. 5.6 for the two cases. The speeds remain close to each other up to $t = 3\tau$, due to the same initial conditions, but ultimately diverge from each other. The average turbulent flame speed is computed from values between

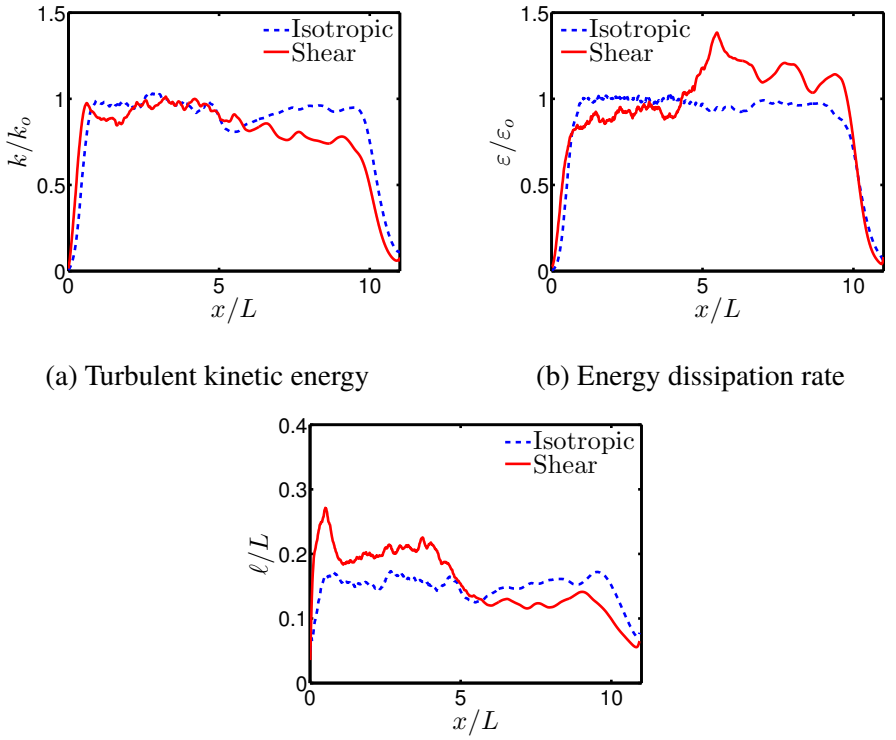

(a) Turbulent kinetic energy

(b) Energy dissipation rate

(c) Integral length scale

Figure 5.4: a) Turbulent kinetic energy profile normalized by the expected value k_o, b) Energy dissipation rate normalized by the expected value ε_o, and c) Integral length scale normalized by the domain width for isotropic (blue) and shear forcing (red) cases.

10τ to 50τ. For isotropic forcing, $\overline{S_T}/S_L \simeq 2.3$ and for shear forcing, $\overline{S_T}/S_L \simeq 2.0$. The shear forcing technique generates lower turbulent flame speeds, by about 12%. A similar trend is observed in the turbulent flame surface area, with averages of $\overline{A_T}/A \simeq 3.0$ and $\overline{A_T}/A \simeq 2.6$ for isotropic and shear simulations respectively. The flame surface area is calculated as the area of the isotherm, using a marching cube algorithm [13]. The $\overline{S_T}/S_L$ values of 2.3 and 2.0 and the $\overline{A_T}/A$ values of 3.0 and 2.6 agree very well with results from Lapointe and Blanquart. [10]

5.2.2 Effects on chemistry

The effects of the forcing on the chemistry and the flame structure are studied by observing the statistical relations between species and temperature. First, the means of the mass fractions of the fuel and hydrogen, conditioned on the temperature are normalized by their maximum values and plotted in Fig. 5.7a. The mean of the fuel consumption rate $\dot{\omega}_F$, conditioned on the temperature, is plotted in Fig. 5.7b,

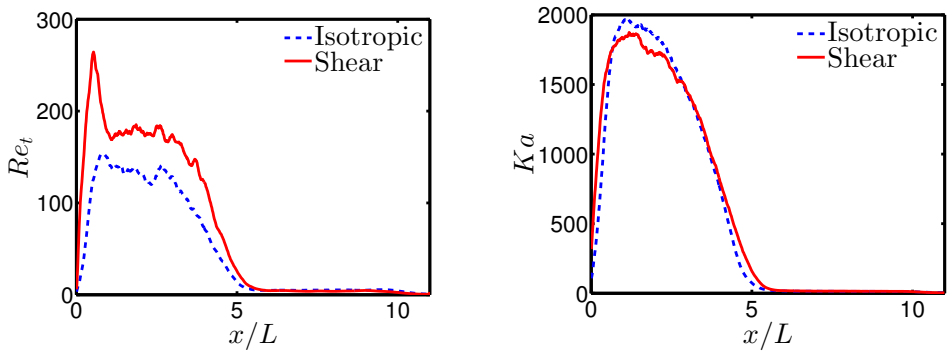

(a) Turbulent Reynolds number (b) Karlovitz number

Figure 5.5: a) Turbulent Reynolds number profile and b) Karlovitz number profile for isotropic (blue) and shear forcing (red) cases.

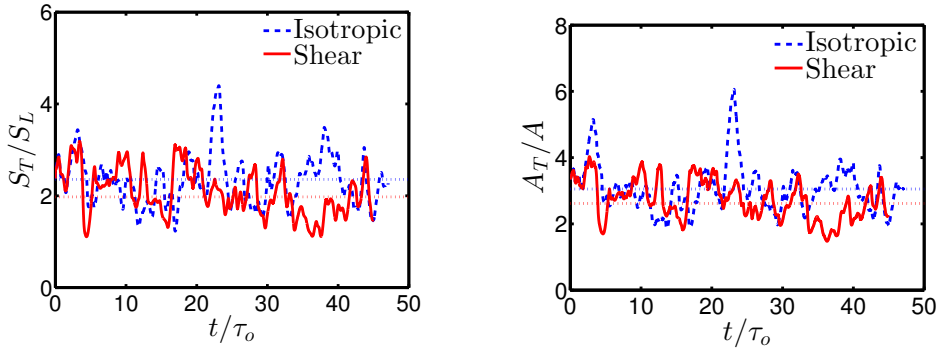

(a) Turbulent flame speed (b) Turbulent flame surface area

Figure 5.6: Time evolution of the turbulent flame speed normalized by the laminar flame speed (a) and the flame surface area normalized by the cross section area (b). Dotted lines correspond to the average values.

normalized by the peak fuel consumption rate for a corresponding laminar flame and compared with results from laminar flames using non-unity Lewis numbers. Finally, the probability density function (pdf) of $\dot{\omega}_F$ at peak fuel consumption temperature T_{peak} is plotted in Fig. 5.7c.

In Fig. 5.7a, the two sets of curves agree perfectly with each other, and there are no observed differences between the forcing techniques. In Fig. 5.7b, the maximum fuel consumption, $\dot{\omega}_{F,peak}$ is observed at T_{peak} = 1230 K. Once again, there is no discernible difference between the results using the different forcing techniques. The fuel consumption rate for both turbulent flames is less than that for a laminar flame, which is consistent with previous studies [10]. Finally, the pdfs have similar shapes for the two cases, with only slight differences in the fuel consumption rate

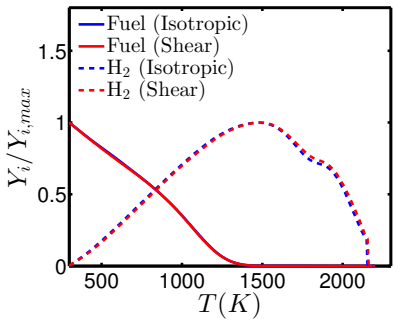

(a) Species mass fractions

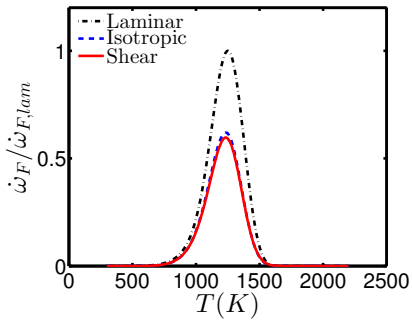

(b) Fuel consumption rate

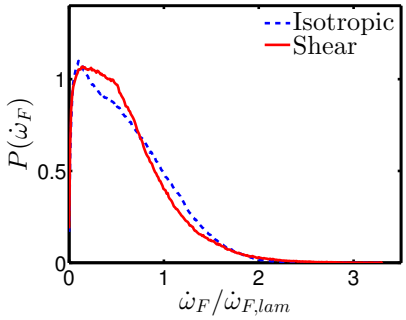

(c) Probability of fuel consumption

Figure 5.7: a) Conditional mean of fuel and hydrogen mass fractions versus temperature, b) Conditional mean of fuel consumption rate versus temperature, c) Probability density function of fuel consumption rate at maximum fuel consumption temperature, T_{peak}.

distribution.

As discussed previously, the turbulent flame structure is controlled by the non-dimensional parameters (Re, Ka, u'/S_L, and ℓ/l_F) [10], which are comparable between the two simulations. Hence, the results show that the forcing technique has no effect on the flame chemistry, as long as the turbulence intensity is similar.

5.2.3 Effects on flow anisotropy

As shown in section 5.2.1, the turbulence intensity is comparable between the different forcing techniques, and the only differences are expected to be in the turbulence anisotropy. This anisotropy can be characterized by examining the components of the velocity and vorticity vectors.

The magnitudes of the fluctuating velocity components are calculated from the root mean square (rms) of the fluctuating velocity field i.e., $|u_i'| = (\widetilde{u_i'' u_i''})^{1/2}$. They are

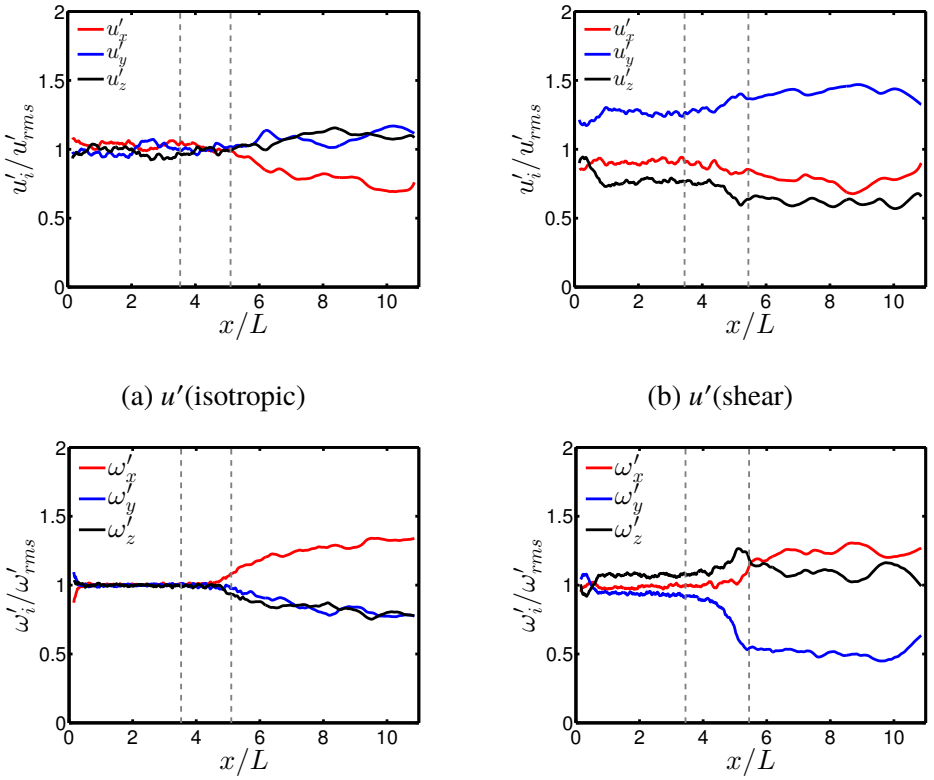

(a) u'(isotropic) (b) u'(shear)

(c) ω'(isotropic) (d) ω'(shear)

Figure 5.8: Velocity fluctuation magnitudes for the isotropic forcing (a) and shear forcing (b), normalized by the root mean square velocity, u_{rms}. Vorticity fluctuation magnitudes normalized by the root mean square vorticity, ω_{rms}, for the isotropic forcing (c) and shear forcing (d). The gray dashed lines correspond to the edges of the flame brush, x_s and x_e, where $d\overline{\rho}/dx$ reaches its minimum value at $0.5(x_s + x_e)$, and $x_e - x_s = (\rho_b - \rho_u)/(d\overline{\rho}/dx)_{min}$

plotted, normalized by $|u_{rms}| = ((\widetilde{u''_x u''_x} + \widetilde{u''_y u''_y} + \widetilde{u''_z u''_z})/3)^{1/2}$ in Fig. 5.8a for the isotropic forcing and in Fig. 5.8b for the shear forcing. For the isotropic forcing, the velocity fluctuations are statistically isotropic in the unburnt region. The velocity components are anisotropic in the burnt region, since the flame stretches the flow, creating anisotropy [2]. The u'_x component has the least energy in the burnt region, and it is important to note that the velocity components along the periodic directions (y and z) are similar for the isotropic case. For the shear forcing case, the velocity fluctuations start out anisotropic in the unburnt region because of the forcing, and the anisotropy increases slightly as the flow proceeds through the flame. The velocity components are different along all three directions.

The anisotropy in the turbulent small scales can be studied by evaluating the rms

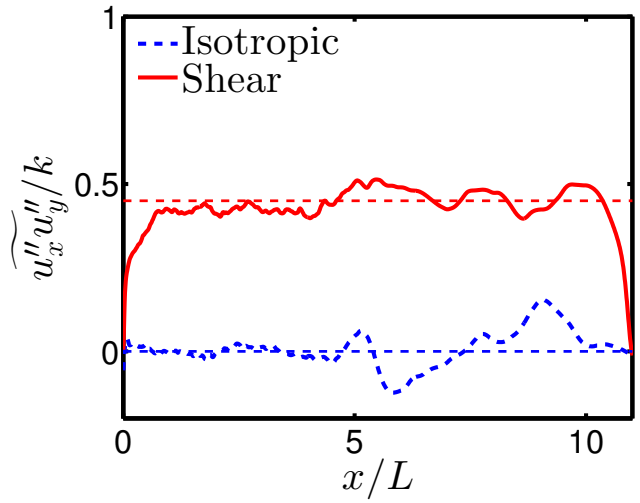

Figure 5.9: Reynolds shear stress normalized by the turbulent kinetic energy for isotropic (blue) and shear (red) cases.

vorticity components along the different directions, $|\omega_i'| = (\overline{\omega_i'\omega_i'})^{1/2}$. They are shown, normalized by $|\omega_{rms}| = ((\overline{\omega_x'\omega_x'}+\overline{\omega_y'\omega_y'}+\overline{\omega_z'\omega_z'})/3)^{1/2}$ for the isotropic forcing in Fig. 5.8c and for the shear forcing in Fig. 5.8d. The isotropic forcing technique produces isotropic vorticity fields $|\omega_i'|/|\omega_{rms}| \simeq 1$ in the unburnt region, and the vorticity components shift away from isotropic values as the flow progresses through the flame. ω_x' becomes the dominant component. In contrast, and as mentioned previously, in the shear forcing case, the unburnt region is already anisotropic due to the anisotropic turbulence forcing. The vorticity magnitudes shift away from isotropic values as the flow passes through the flame, and ω_y' becomes the least dominant component. The vorticity components along y and z are similar for the isotropic technique, and are different for the shear forcing technique.

The impact of the flame alone on the flow anisotropy can be observed in the burnt region of the isotropic case (Fig. 5.8a and 5.8c); and the isolated effect of the shear forcing can be seen in the unburnt side of the shear case (Fig. 5.8b and 5.8d). It is clear that the shear forcing has a slightly bigger impact on the velocity anisotropy and the flame has a bigger impact on the vorticity anisotropy.

Finally, the Reynolds shear stress normalized by the kinetic energy is plotted as a function of space in Fig. 5.9. For the isotropic case, the Reynolds shear stress is zero throughout, within statistical uncertainty. For the shear case, the Reynolds shear stress value is around 0.45 in the unburnt region, with a very slight increase in the

burnt region due to the lower Reynolds number (see Table 2.2).

5.3 Results - Advection

Turbulent flame simulations are performed using shear forcing (Eq. (5.4)) with shear convection applied. The simulation is initialized with the same initial conditions, and the same inflow field is used from the other simulations.

5.3.1 Time step

As explained earlier in Section 5.1.2, the maximum magnitude of the imposed velocity is given by $V_{max} = 2BL$ and it is about 15 times larger than the rms velocity, $u' \sim 0.12BL$. Hence, the CFL condition for this imposed mean velocity gives,

$$V_{max}\frac{\Delta t}{\Delta y} < 1. \tag{5.14}$$

Therefore $\Delta t < \frac{\Delta y}{2BL}$. It is clear that the turbulent flame simulations with shear convection must be performed with a smaller time step. It is observed that the chosen time step has an effect on the results, hence it is reduced until the results are independent of time step, which is observed for $dt = 2\times10^{-8}$ and lower. Hence, the time step chosen for the advection simulation is 2×10^{-8}, which is 20 times smaller than that of the shear simulation. Hence, a simulation is performed starting from the velocity and scalar field at 30τ from the shear simulation, and shear forcing and shear convection are applied to the turbulent flame simulations for 10τ.

The effects of shear convection on chemistry and turbulence are discussed in the following subsections.

5.3.2 Global quantities

2D contours of temperature in the x-y plane are plotted in Fig. 5.10 for shear turbulence with and without shear convection. In both cases, the turbulent flame position can be observed near the middle of the domain, $5.5L$. Qualitatively, there is no distinct difference between the two simulations. The flame brush thickness is the same for the two cases.

The time-averaged kinetic energy and energy dissipation rate are plotted over the domain for the two cases along with isotropic turbulence in Fig. 5.11, normalized by their expected values. The shear and advection simulations have similar kinetic energy and energy dissipation rate outside the shear convection region seen in Fig. 5.11, however the values where shear convection is applied are different between

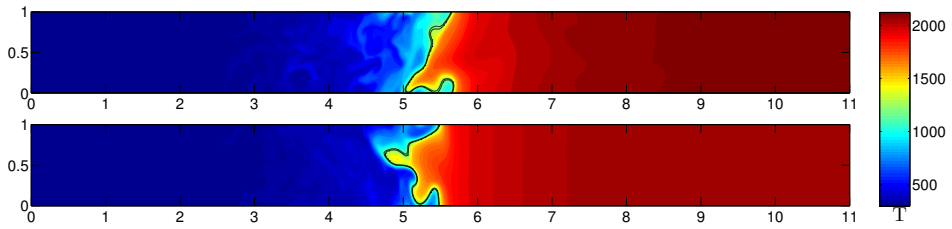

Figure 5.10: Instantaneous temperature contours in the x-y plane for shear simulation (top) and advection simulation (bottom). The black curves locate the edges of the reaction zone, corresponding to $T_{\text{peak}} - 30\,K$ and $T_{\text{peak}} + 30\,K$, where T_{peak} is the maximum fuel consumption temperature.

the advection simulation and the other two cases. The results from the advection simulation also fluctuates more due to the smaller sample size.

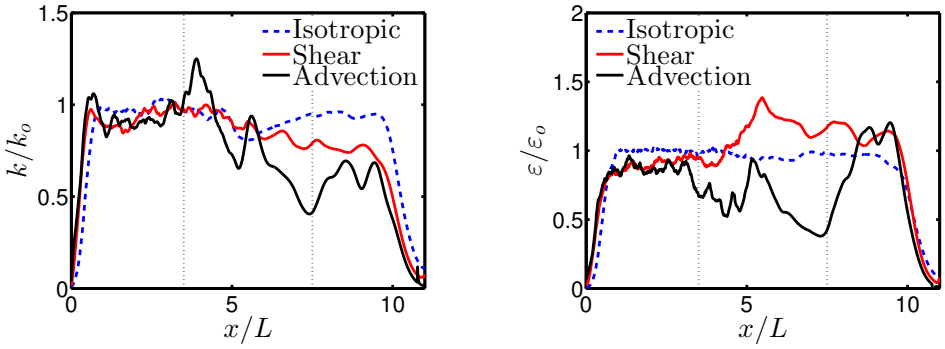

(a) Turbulent kinetic energy

(b) Energy dissipation rate

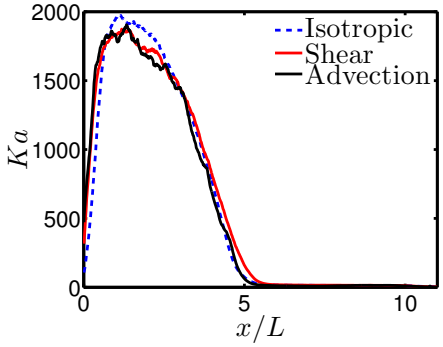

(c) Karlovitz number

Figure 5.11: a) Turbulent kinetic energy profile normalized by the expected value k_o, b) Energy dissipation rate normalized by the expected value ε_o, and c) Karlovitz number profile for isotropic (blue), shear (red), and advection (black) cases.

The turbulent flame speed S_T is plotted in Fig. 5.12a for the shear and advection cases starting from $t = 30\tau$. It can be seen that the speeds diverge from each other soon

after the start of the simulation. The average turbulent flame speeds are calculated between 30τ and 40τ for the two cases and the average values are very close to each other, $\overline{S_T}/S_L \simeq 1.70$ for the shear case and $\overline{S_T}/S_L \simeq 1.65$ for the advection case. The flame surface area evolution is shown in Fig. 5.12b. They have different instantaneous values, but the average values are once again close, $\overline{A_T}/A \simeq 2.3$ for the shear case and $\overline{A_T}/A \simeq 2.1$.

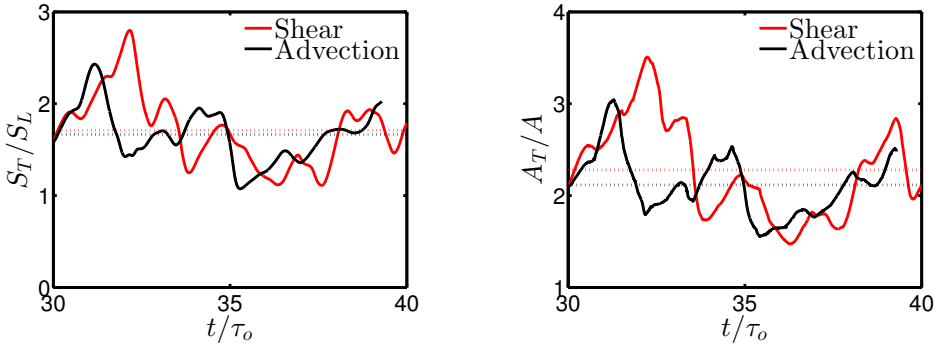

(a) Turbulent flame speed

(b) Turbulent flame surface area

Figure 5.12: Time evolution of the turbulent flame speed normalized by the laminar flame speed (a) and turbulent flame surface area normalized by the cross-section area (b) for shear (red) and advection (black) simulations.

5.3.3 Effects on chemistry

The conditional means of the mass fractions of the fuel and hydrogen normalized by their maximum values are plotted versus temperature in Fig. 5.13a. The conditional mean of the fuel consumption rate $\dot{\omega}_F$ is plotted in Fig. 5.13b, normalized by the laminar flame peak value and compared with results from a corresponding laminar flame. Finally, the probability density function (pdf) of $\dot{\omega}_F$ at peak fuel consumption temperature T_{peak} is plotted in Fig. 5.13c.

In Fig. 5.13a, all the curves agree well with each other, and there are no observed differences between the forcing techniques. In Fig. 5.13b, the maximum fuel consumption, $\dot{\omega}_{F,peak}$ is observed at $T_{peak} = 1230$ K for all three cases. The fuel consumption rates agree perfectly well with each other. Finally, the pdf from the advection case agrees well with that of the shear case and isotropic case, and there are only slight differences in the fuel consumption rate distribution. Despite the small sample size, local chemistry quantities are fully converged, and do not exhibit large fluctuations.

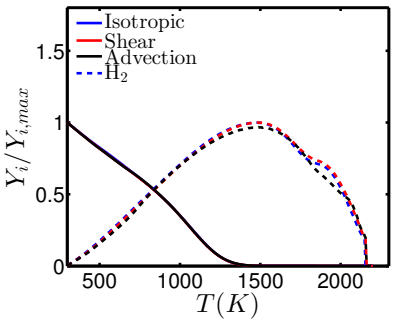

(a) Species mass fractions

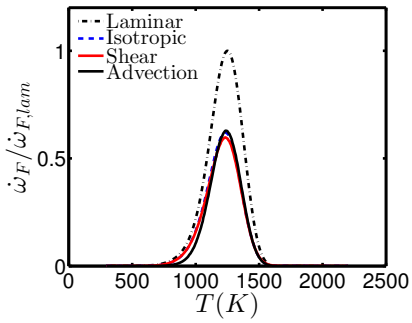

(b) Fuel consumption rate

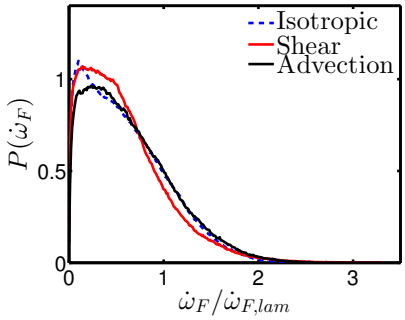

(c) Probability of fuel consumption

Figure 5.13: a) Conditional mean of fuel and hydrogen mass fractions versus temperature, b) Conditional mean of fuel consumption rate versus temperature, c) Probability density function of fuel consumption rate at maximum fuel consumption temperature, T_{peak}.

5.3.4 Effects on flow anisotropy

The anisotropy values of the velocity components, $|u_i'|/|u_{rms}|$, are plotted in Fig. 5.14a for the shear turbulence case and Fig. 5.14b for the advection case. Unlike the shear forcing case, where u_x' and u_z' have different magnitudes throughout the domain, the burnt side of the advection simulation has similar magnitudes for u_x' and u_z', especially in the region with shear convection. Most of the differences between the shear and advection cases are in the region between 3.5 L and 7.5 L.

The anisotropy in the vorticity components along the different directions, $|\omega_i'|/|\omega_{rms}|$, is plotted as a function of x for the shear forcing in Fig. 5.14c and for the shear forcing with shear convection in Fig. 5.14d. The vorticity magnitude in the y direction is much smaller on the burnt side, while ω_x' and ω_z' have similar magnitudes greater than 1 for the shear case. In the advection case, however, ω_x' is the only strongest component in the burnt side with convection applied, and the magnitude of ω_y' drops further where there is no shear convection.

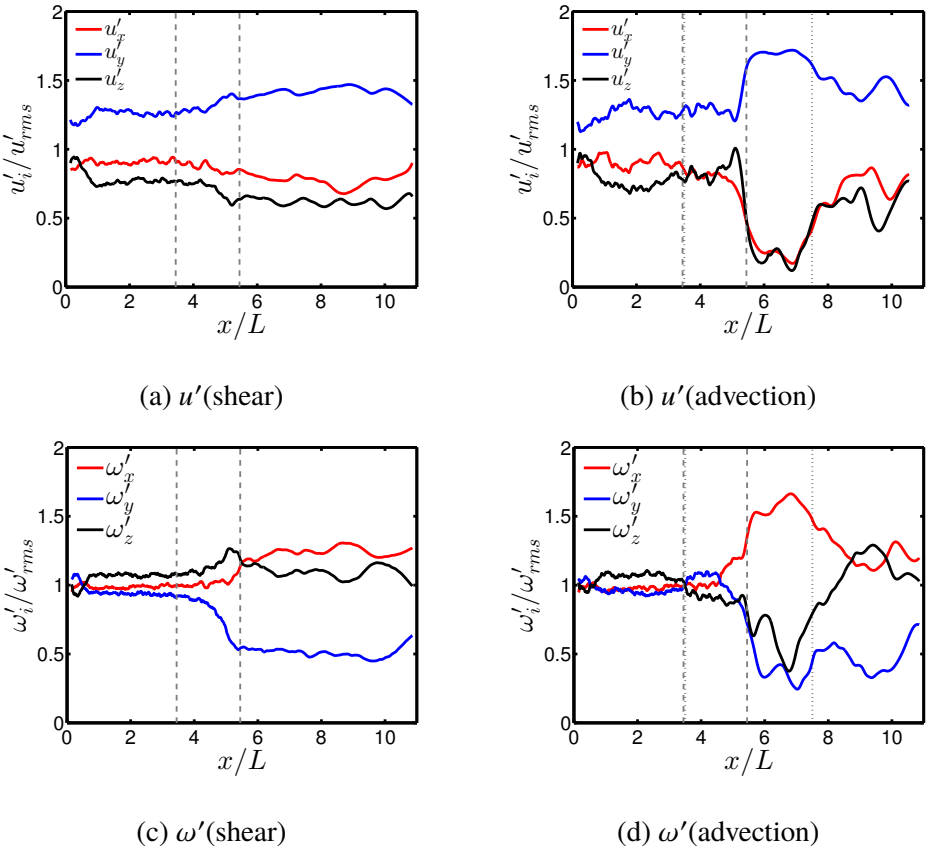

(a) u'(shear) (b) u'(advection)

(c) ω'(shear) (d) ω'(advection)

Figure 5.14: Velocity fluctuation magnitudes for the isotropic forcing (a) and shear forcing (b), normalized by the root mean square velocity, u_{rms}. Vorticity fluctuation magnitudes normalized by the root mean square vorticity, ω_{rms}, for the isotropic forcing (c) and shear forcing (d). Gray dashed lines in these plots correspond to the edges of the turbulent flame brush and dotted lines are the edges of the shear convection region.

5.4 Results - Pressure

A fourth turbulent flame simulation is performed using isotropic forcing (Eq. (5.2)), with the pressure term added. The simulation uses the same initial conditions and inflow velocity fields. The simulation is performed for 50 eddy turnover times, τ, and averages are calculated after a transient period of 10τ. The isolated effects of the mean pressure gradient term on chemistry and turbulence can be observed based on comparisons between the results from the isotropic and pressure simulations, and the results are discussed in the following subsections.

5.4.1 Global quantities

2D contours of temperature in the x-y plane are plotted in Fig. 5.15 for the two different forcing techniques. In both cases, the turbulent flame structure can be observed near the middle of the domain, $5.5L$. The flame brush thickness is much larger for the pressure case, with $l_t = 2.4\,L$ which is much larger than the flame brush thickness of the isotropic case ($1.44\,L$).

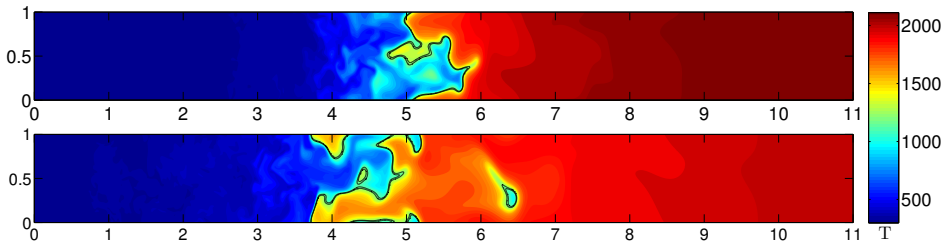

Figure 5.15: Instantaneous temperature contours in the x-y plane for the isotropic case (top) and pressure case (bottom). The black curves locate the edges of the reaction zone, corresponding to $T_{\text{peak}} - 30\,K$ and $T_{\text{peak}} + 30\,K$, where T_{peak} is the maximum fuel consumption temperature.

The planar-averaged kinetic energy and energy dissipation rate are plotted over the domain for the four cases in Fig. 5.16, normalized by the expected values for the isotropic case. The pressure simulations have a largely different kinetic energy and energy dissipation rate profile as seen in Fig. 5.16. The initial values are comparable to the other cases, whereas around the flame, the values are much higher. This is because the density fluctuates near the flame, and the pressure term generates turbulence.

The turbulent kinetic energy equation for the pressure case is given by

$$\widetilde{u}_x \frac{dk}{dx} + \frac{d}{dx}\left(\widetilde{u_x'' \boldsymbol{u}''^2}\right) = -\frac{1}{\overline{\rho}}\frac{d}{dx}\left(\overline{p' u_x''}\right) - \varepsilon + 2Ak_o + \mathcal{P}\frac{\overline{\rho' u''}}{\overline{\rho}}, \tag{5.15}$$

where $\widetilde{u}_x \frac{dk}{dx}$ is the advection, $\frac{d}{dx}\left(\widetilde{u_x'' \boldsymbol{u}''^2}\right)$ and $-\frac{1}{\overline{\rho}}\frac{d}{dx}\left(\overline{p' u_x''}\right)$ are the diffusion due to the turbulence and pressure respectively, ε is the viscous dissipation, $2Ak_o$ is the production from the isotropic forcing, and the contribution from the pressure term is $\mathcal{P}\overline{\rho' u''}/\overline{\rho}$. The turbulent kinetic energy budget profile is plotted in Fig. 5.17a, normalized by the expected dissipation rate for the isotropic case. The production (blue) is constant at a value of 1 throughout the domain, owing to the factor k_o/k added to the forcing term. This results in the production being constant at a value of $2Ak_o$ throughout the domain, instead of $2Ak$, which is not constant for the pressure

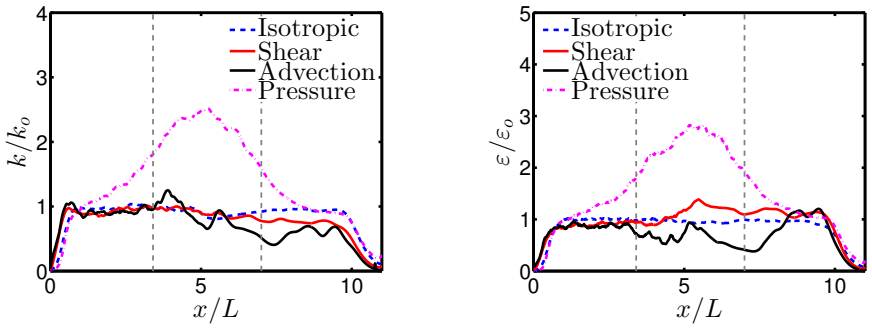

(a) Turbulent kinetic energy (b) Energy dissipation rate

Figure 5.16: a) Turbulent kinetic energy profile normalized by the expected value, k_o, b) Energy dissipation rate normalized by the expected value, ε_o, for isotropic (blue), shear (red), advection (black), and pressure (magenta) cases. The gray dashed lines correspond to the edges of the turbulent flame brush.

case. The contribution from the pressure term (red) is stronger than the production within the flame brush, though it has some small contribution outside the flame brush. The viscous dissipation (magenta) balances the sum of the production and the pressure term, and the advection (green) is near zero. The sum of all these contributions, corresponding to turbulent diffusion and pressure diffusion, is near zero throughout with some fluctuations within the flame brush.

The Karlovitz number is plotted in Fig. 5.17b, and all four simulations have similar Karlovitz number on the unburnt side. The Ka of the pressure simulation drops more quickly across the flame, compared to the other simulations.

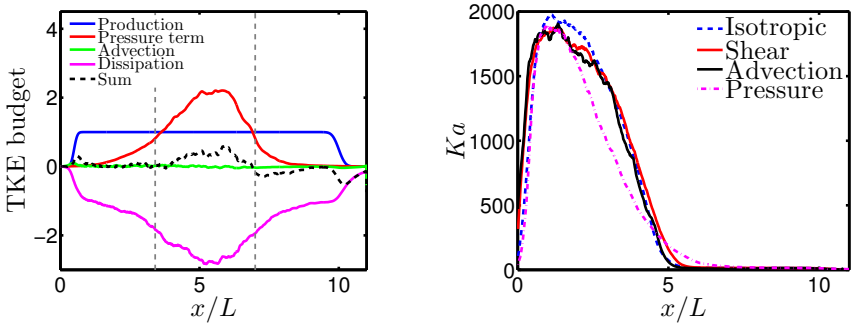

(a) Turbulent kinetic energy budget (b) Karlovitz number

Figure 5.17: a) Turbulent kinetic energy budget profile - Production (blue), pressure term (blue), advection (green), dissipation (magenta), and sum (black). b) Karlovitz number profile for isotropic (blue), shear (red), advection (black), and pressure (magenta) cases.

The turbulent flame speed, S_T, is plotted in Fig. 5.18a for the four cases. The turbulent flame speed is much higher for the case with pressure. The average flame speeds are $\overline{S_T}/S_L \simeq 4.8$ for pressure, $\overline{S_T}/S_L \simeq 2.3$ for isotropic forcing, and $\overline{S_T}/S_L \simeq 2.0$ for shear forcing. The turbulent flame surface areas are plotted in Fig. 5.18b for all three cases. The flame surface area is also much higher for the pressure case, with the average value given by $\overline{A_T}/A \simeq 6.2$, with $\overline{A_T}/A \simeq 3.0$ for isotropic forcing, and $\overline{A_T}/A \simeq 2.6$ for shear forcing. Both metrics for the pressure case are larger by the same factor when compared to the other simulations. The burning efficiency, I_0, defined as $I_0 = (S_T/S_L)/(A_T/A)$, is plotted versus time in Fig. 5.18c for all three cases. The burning efficiency factors for all four cases fluctuate around 0.77. Hence, it is evident that the increase in the flame speed is a result of the increased flame surface area. The burning efficiency value of 0.77 matches well with simulation results of flame B from Lapointe and Blanquart. [10]

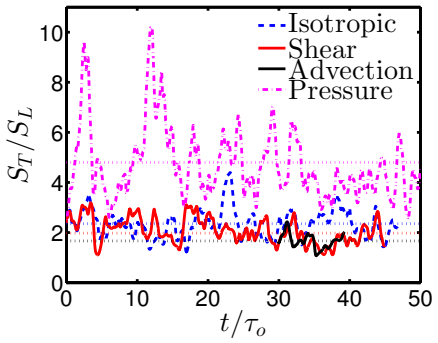

(a) Turbulent flame speed

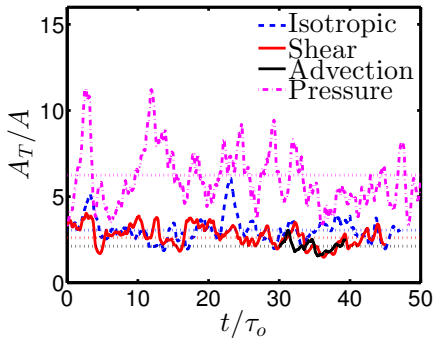

(b) Turbulent flame surface area

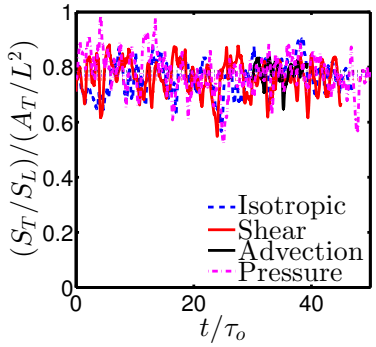

(c) Burning efficiency factor

Figure 5.18: Time evolution of the turbulent flame speed normalized by the laminar flame speed (a), flame surface area normalized by the cross section area (b), and burning efficiency factor (c). Dotted lines correspond to the average values.

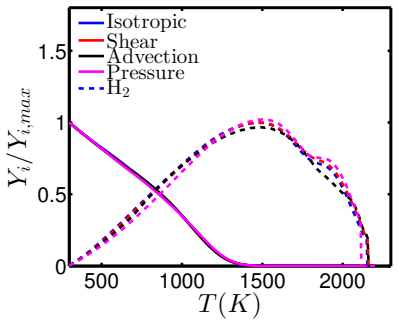

(a) Species mass fractions

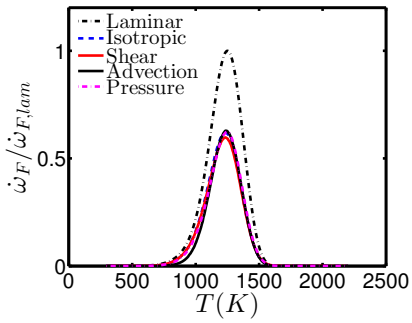

(b) Fuel consumption rate

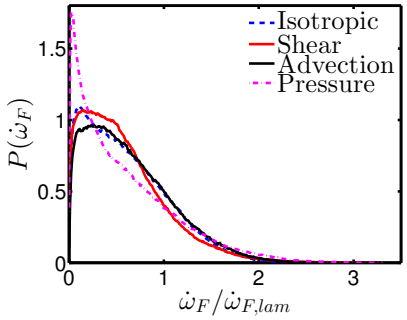

(c) Probability of fuel consumption

Figure 5.19: a) Conditional mean of fuel and hydrogen mass fractions versus temperature, b) Conditional mean of fuel consumption rate versus temperature, c) Probability density function of fuel consumption rate at maximum fuel consumption temperature, T_{peak}.

5.4.2 Effects on chemistry

The conditional means of the mass fractions of the fuel and hydrogen with temperature are plotted in Fig. 5.19a, normalized by their maximum values. The mean of the fuel consumption rate $\dot{\omega}_F$, conditioned on the temperature, is plotted in Fig. 5.19b, normalized by the peak laminar fuel consumption rate. Finally, the probability density function (pdf) of $\dot{\omega}_F$ at peak fuel consumption temperature T_{peak} is plotted in Fig. 5.19c.

In Fig. 5.19a, the four sets of curves agree very well with each other, and there are only very small differences in the hydrogen mass fraction for the pressure case. In Fig. 5.19b, the maximum fuel consumption, $\dot{\omega}_{F,peak}$ is observed at $T_{peak} = 1230$ K. Once again, there is no discernible difference between the pressure case and the isotropic case. Finally, the pdf for the pressure case has a higher peak and variance than the other three cases, but the mean value of fuel consumption rate is similar for all four cases. The Karlovitz number profile is slightly different for the pressure

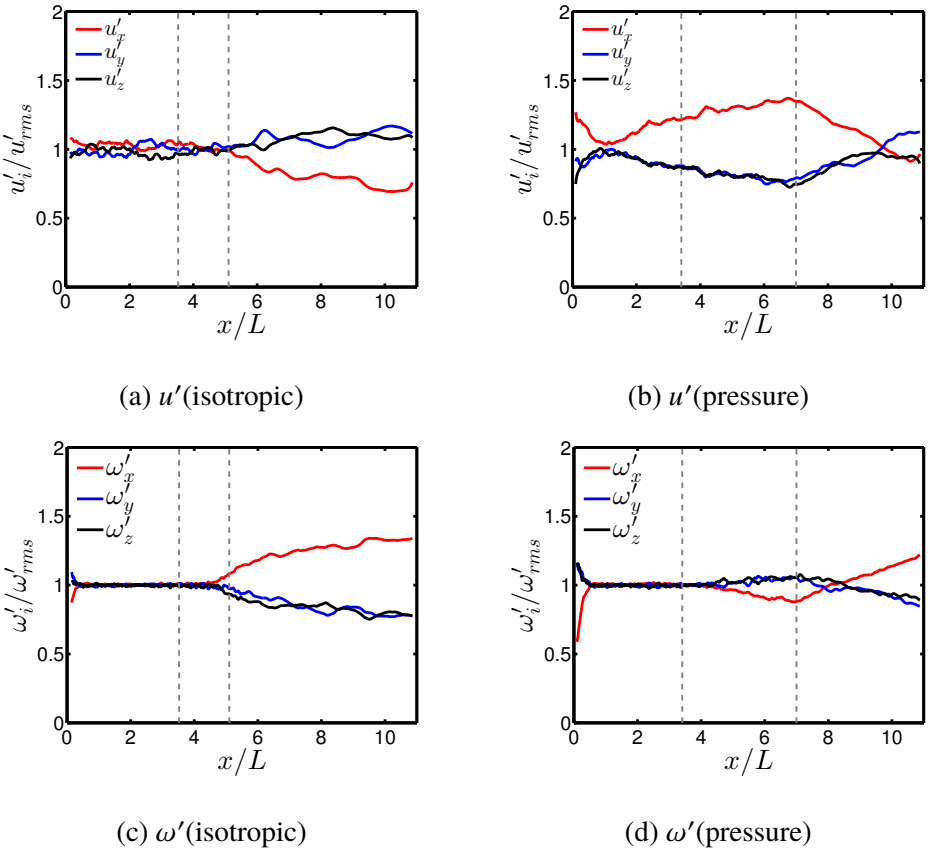

(a) u'(isotropic) (b) u'(pressure)

(c) ω'(isotropic) (d) ω'(pressure)

Figure 5.20: Velocity fluctuation magnitudes for the isotropic simulation (a) and pressure simulation (b), normalized by the root mean square velocity, u_{rms}. Vorticity fluctuation magnitudes normalized by the root mean square vorticity, ω_{rms}, for the isotropic case (c) and pressure case (d). The gray dashed lines correspond to the two edges of the turbulent flame brush.

case, and this could be the cause of the difference in the probability distribution.

5.4.3 Effects on flow anisotropy

The anisotropy due to the pressure term can be characterized by examining the components of the velocity and vorticity vectors, and comparing the results between the isotropic simulation and the pressure simulation.

The magnitudes of the fluctuating velocities, $|u'_i|$, are plotted, normalized by $|u_{rms}|$ in Fig. 5.20a for the isotropic case and Fig. 5.20b for the pressure case. The pressure gradient term is added only in the x direction, and consequently increases the magnitude of the x component of the velocity fluctuations. The impact of the pressure term on the velocity components are observed near the flame brush, and to a smaller extent throughout the domain. The flame however, starts affecting the

velocity anisotropy only after the end of the flame brush as observed in Fig. 5.20a. In the pressure case, the magnitude of u'_x starts decreasing in the burnt region due to the flame, as it does in the isotropic case. In both cases, the components along the two homogeneous directions have similar magnitudes.

The anisotropy in the vorticity components along the different directions, $|\omega'_i|/|\omega_{rms}|$, are presented in Fig. 5.20c for the isotropic case and in Fig. 5.20d for the pressure simulation. The vorticity magnitudes in the x direction decreases around the flame, due to the pressure term, and the flame increases its magnitude, just as in the isotropic case. The vorticity components along y and z are similar for both the cases.

It is clear that the pressure term has a bigger impact on the velocity anisotropy than the flame, and a small impact on the vorticity. The pressure term has the opposite effect of the flame, in both velocity and vorticity components. The Reynolds shear

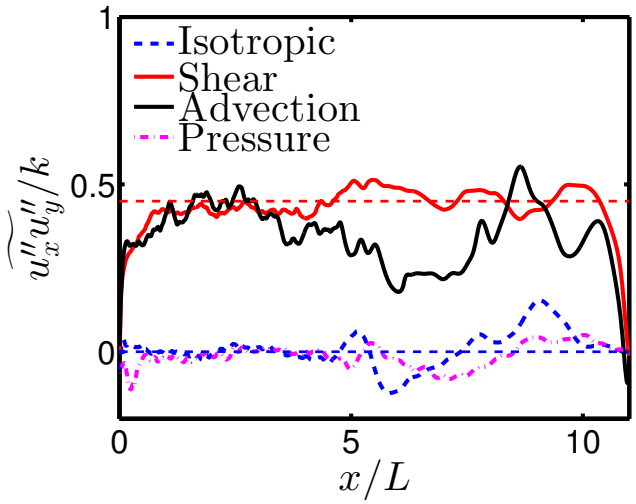

Figure 5.21: Reynolds shear stress normalized by the turbulent kinetic energy for isotropic (blue), shear (red), advection (black), and pressure (magenta) cases.

stress normalized by the kinetic energy is plotted as a function of space in Fig. 5.21. For the pressure case, just like in the isotropic case, the Reynolds shear stress is near zero throughout the domain, with small fluctuations in the burnt region.

5.5 Conclusions

The effects of the forcing matrix, mean pressure gradients, and shear convection term on the turbulent flame simulations are observed. All four simulations have similar Karlovitz numbers in the unburnt side and turbulence intensities.

The turbulent kinetic energy and viscous dissipation profiles are constant throughout the domain for the isotropic, shear, and advection cases, whereas the pressure case creates higher turbulence values around the flame brush.

The turbulent flame speed and the turbulent flame surface area are compared between the four simulations. The average values of the isotropic, shear, and advection cases are similar, while the pressure case exhibits much higher flame speed and area, by a factor of about 2. The burning efficiency of all four cases are very close.

The local chemistry is unaltered by any of these terms. The conditional means on temperature reveal similar turbulent flame structure for all the four cases. The only small difference is in the probability density function of the fuel consumption rate.

The significant differences between the four cases are the anisotropy of the velocity and vorticity vectors. The flame creates anisotropy in both velocity and vorticity, whereas the shear forcing induces high anisotropy in velocity alone. The shear convection creates high anisotropy in velocity and vorticity, especially in the burnt region. The pressure term creates anisotropy in both velocity and vorticity throughout the domain, and has the opposite impact as the flame.

Chapter 6

CONCLUSIONS

The search for alternative fuels for use in aircraft can use up a lot of time and resources. This thesis tackled the problem with efficient computational frameworks to study highly turbulent flames using simple computational domains. The techniques were developed and simulations were performed for both incompressible turbulence and turbulent flames.

6.1 Incompressible turbulence

To provide a physical and mathematical foundation to realistic turbulent flows, the turbulence forcing technique for shear flows was directly computed from the large scales of these flows. Different statistically stationary free shear flows were considered for the calculations of the forcing matrix. The forcing terms did not just arise from the shear strain or the velocity gradients, but also from periodicity corrections in x, y/r, and continuity corrections, which generated both linear and non-linear forcing terms. The additional source terms were calculated by leveraging the self-similarity of velocity fluctuations and their moments.

An *a priori* analysis was performed in order to estimate the effect of the multiple source terms to the turbulence, including the linear diagonal forcing terms, non-linear forcing terms, and the mean advection term. The relation between the forcing constant and the Taylor micro-scale Reynolds number was established, so that turbulence quantities can be predicted prior to selecting the grid resolution for any simulation.

The turbulence generated was anisotropic in nature, consistent with that observed in the middle of shear layers. The Reynolds shear stress values are over predicted, compared to experimental and simulation results. For the same Reynolds number, the anisotropic turbulence has higher integral length scale compared to the domain size, lower turbulent kinetic energy and dissipation rate, and higher eddy turnover time than isotropic turbulence.

Anisotropy was observed both in the components of velocity and vorticity. The anisotropy in the fluctuating velocity agrees reasonably well with results from simulations and experiments of free shear flows. The anisotropy in the fluctuating

velocity showed no clear Re_λ dependence, while the vorticity components become more isotropic with increasing Reynolds number. The spectra for the energy and production agree with the scalings suggested by turbulence theory and past simulations.

Simulations were performed with the additional linear and non-linear source terms, and compared with the pure shear simulations, with a special attention to Reynolds shear stress, turbulent kinetic energy budget, and velocity correlations. There was no significant difference between the two simulations with linear source terms. The simulation with all the linear and non-linear terms showed non-zero turbulent diffusion and skewness in velocity fluctuation distributions, which were not present in the simulation with just the linear terms. In either case, the additional forcing terms did not significantly improve upon the simulation results.

The shear convection due to the mean advection term was applied *a posteriori*, and simulations were performed emulating its effect. It was observed that the effect of this term is not significant and would be negligible especially at high Reynolds number. The results also pointed out the potential role of splitting errors in previously published temporally unbounded numerical simulations.

The impact of aspect ratio of the computational domain on both isotropic and shear turbulence characteristics was studied. The integral length scale was slightly reduced for both cases, however the effect was weaker in the case of shear turbulence. The anisotropy values were unaffected by the change in aspect ratio.

Introducing an inflow/outflow in one direction did not significantly affect the statistics of either isotropic turbulence or shear turbulence. The velocity and vorticity components were isotropic for the isotropic turbulence forcing scheme as expected, and were anisotropic for the shear turbulence, and the shear turbulence anisotropy values were consistent with results from shear turbulence simulations in triply periodic cubic domains.

Finally, shear convection was introduced in a portion of the domain in the shear turbulence simulation. This resulted in statistically stationary shear turbulence, with larger integral length scale, and anisotropy values that match perfectly with that of free shear flows.

6.2 Turbulent flames

A mathematically rigorous numerical turbulence forcing technique was derived for turbulent flame simulations. The turbulence production, advection by the imposed

flow, and pressure gradients were identified to be significant and were chosen to study their impact on the turbulent flame statistics.

Four different turbulent flame simulations were performed in a doubly periodic inflow/outflow configuration: one with isotropic forcing which had been used by other researchers in the past [18, 19, 11, 2, 10], one with shear forcing, one with shear forcing and shear convection, and the fourth with isotropic forcing with the pressure term. Forcing constants were chosen such that the simulations had similar Karlovitz numbers in the unburnt region.

The isotropic and shear simulations were compared to observe the effects of the forcing on global and local quantities in chemistry and turbulence. The turbulent kinetic energy, energy dissipation rate, and the turbulent Reynolds number were comparable between the two cases. It was seen that the turbulent flame speed and the flame brush thickness are comparable between the two cases. Local chemistry quantities were observed by plotting the mass fraction and consumption rate of the fuel as functions of temperature. The local chemistry quantities were indistinguishable for the two different forcing techniques. The pdfs of the fuel consumption rate at T_{peak} also seemed very similar between the two different cases.

Anisotropy in the velocity and vorticity components was observed for the two different forcing methods. For the isotropic forcing method, the flow was isotropic in the unburnt region and was anisotropic in the burnt region both in velocity and vorticity. For the shear forcing method, the flow was already anisotropic in the unburnt side both in the velocity and vorticity, and the flame added slightly to the anisotropy in velocity and significantly to the anisotropy in vorticity. The shear forcing generated more velocity anisotropy than the flame, and the flame generates more vorticity anisotropy.

The effect of shear convection was observed by comparing the advection simulation and the shear simulation. The chemistry properties were mostly unaffected, while the anisotropy values were different where shear convection was applied. The impact of shear convection was much higher in the burnt region, due to the lower Reynolds number.

The effect of mean pressure gradient across the flame was analyzed by comparing the isotropic and pressure simulations. For the pressure simulation, the turbulent kinetic energy and dissipation rate were much higher around the flame, whereas the Reynolds number and Karlovitz number were comparable to the other simulations.

The local chemistry was unaffected, while increased flame surface area caused an increase in flame speed. Anisotropy was produced by the mean pressure gradient throughout the flame and counteracted the anisotropy created by the flame on both velocity and vorticity components.

From these results, if one is interested in the effects of the chemistry on the flow field, the appropriate forcing technique and large scale effects needs to be used, as vorticity and velocity components are affected greatly by the forcing terms. However, if the effects of turbulence on the flame be of interest, then any forcing method and configuration is appropriate for simulating the turbulent flame. As the global chemistry quantities are of interest for engine combustion, one can conclude that the turbulence intensity (u', ℓ), and the pressure term ($\boldsymbol{u^i} \cdot \underline{\nabla \boldsymbol{u^i}}$) are the only relevant turbulence terms that have a profound impact on the global flame behavior. This is illustrated in Fig. 6.1.

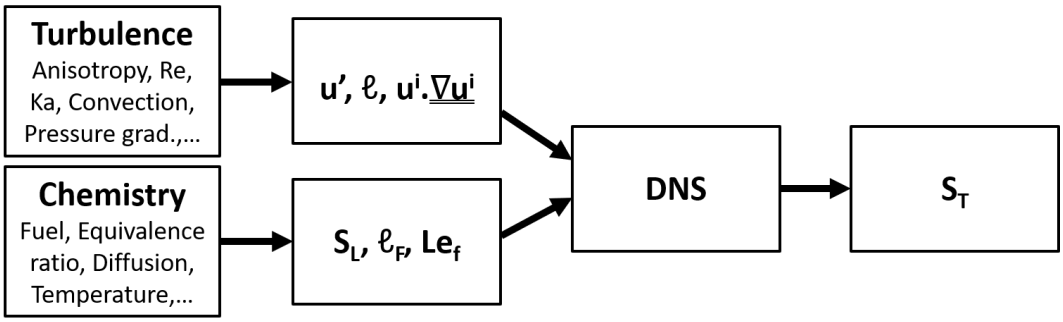

Figure 6.1: Plan of attack for bio-fuel testing.

Lapointe and Blanquart analyzed the impact of various parameters related to the chemistry of the turbulent flame [10] and concluded that the laminar flame speed, flame thickness, and the fuel Lewis number are the most relevant parameters (see Fig. 6.1). A similar study is conducted on the different turbulent flow conditions in this thesis, and the most relevant parameters are the the turbulence intensity and the pressure term. Using this, one needs to only test new fuels for their laminar flame properties, and this can be accomplished using very small amounts of fuel. The turbulence intensity and pressure term are fuel independent and can be measured from engine-probes. These values can then be used to estimate global quantities like the turbulent flame speed.

6.3 Future Work

The forcing matrix calculated from the mean velocity gradients can help create the correct fluctuation magnitudes. So far, simulations of single locations at the

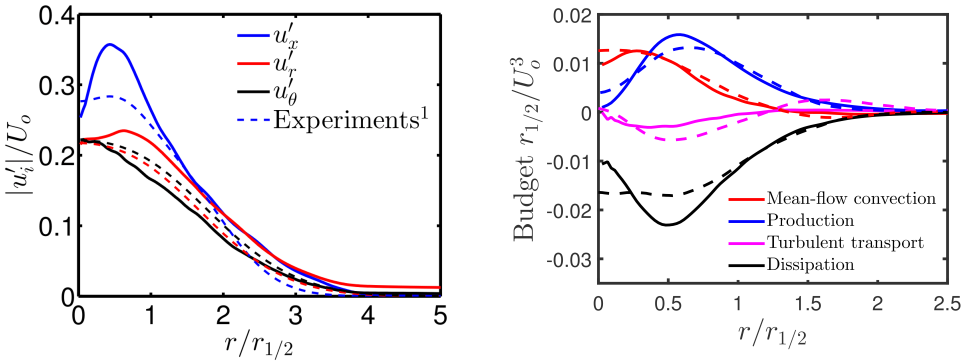

(a) Velocity fluctuation magnitude profile (b) Turbulent kinetic energy budget

Figure 6.2: a) Velocity fluctuation magnitude profiles and b) Turbulent kinetic energy budget as a function of the radial distance, r.

centerline and shear layer of a round jet were captured. One can extend this to recreate whole cross-section of jets. This can be done for both incompressible and reacting jets.

6.3.1 Cross-section of round jet

A new framework for simulating turbulent jets is proposed, wherein a portion of the jet is emulated with a “disk" of finite thickness, that is periodic in the axial direction. The analysis uses the self-similarity of turbulence in jets, and implements corresponding normalizations for velocity components and spatial coordinates.

The resolved velocity is given by $\boldsymbol{u^r} = \{u'_x, u_r, u_\theta\}$, and the imposed velocity is given by $\boldsymbol{u^i} = \{\overline{u_x}, 0, 0\}$. The governing equations for the imposed velocity is given by,

$$\frac{\partial u'_x}{\partial x} + \frac{1}{r}\frac{\partial}{\partial r}(r u_r) + \frac{\partial u_\theta}{\partial \theta} = -\frac{\partial \overline{u_x}}{\partial x} + \frac{u'_x}{x_o}, \tag{6.1}$$

$$\frac{\partial u'_x}{\partial t} + (u'.\nabla)\,u'_x = -\frac{1}{\rho}\frac{\partial p'}{\partial x} + (\nabla.\tau')\,.e_x - \frac{\partial \overline{u_x}}{\partial x}u'_x + \frac{\overline{u_x}}{x_o}u'_x - \frac{\partial \overline{u_x}}{\partial r}u'_r + \overline{u'_r\frac{\partial u'_x}{\partial r}}, \tag{6.2}$$

$$\frac{\partial u_r}{\partial t} + (u'.\nabla)\,u_r = -\frac{1}{\rho}\frac{\partial p}{\partial r} + (\nabla.\tau)\,.e_r + \frac{\overline{u_x}}{x_o}u_r, \tag{6.3}$$

$$\frac{\partial u_\theta}{\partial t} + (u'.\nabla)\,u_\theta = -\frac{1}{\rho r}\frac{\partial p}{\partial \theta} + (\nabla.\tau)\,.e_\theta + \frac{\overline{u_x}}{x_o}u_\theta - \frac{\overline{u_\theta}}{\tau} \tag{6.4}$$

So, in theory, one could recreate the velocity fluctuation profiles and turbulent kinetic energy budget, just from the mean velocity gradients. Initial results are plotted in Fig. 6.2.

6.3.2 Cross-section of reacting jet

A new framework for simulating turbulent flames using cylindrical domains is proposed, with the average flame front positioned at a certain radial location. The analysis would leverage some information about the self-similarity of turbulence and chemistry in reacting jets, and implement corresponding normalizations for velocity components and spatial coordinates, and include radially dependent forcing terms in the momentum and chemistry equations. Mean flame curvature effects are included in the current study, as opposed to the statistically flat flames in previous simulations. Previous simulations with inflow/outflow used constant turbulent intensity for the entire domain. In contrast, in the current study, the turbulent intensity would change with radial distance, which more closely represents experimental setups. As mentioned earlier, the numerical framework should allow for the choice of flame location with respect to the location of the shear layer, and both premixed and non-premixed flames could be simulated with this technique. The effects of the mean flame curvature can be observed by comparing the results to statistically flat flames.

Preliminary results are plotted in Fig. 6.3.

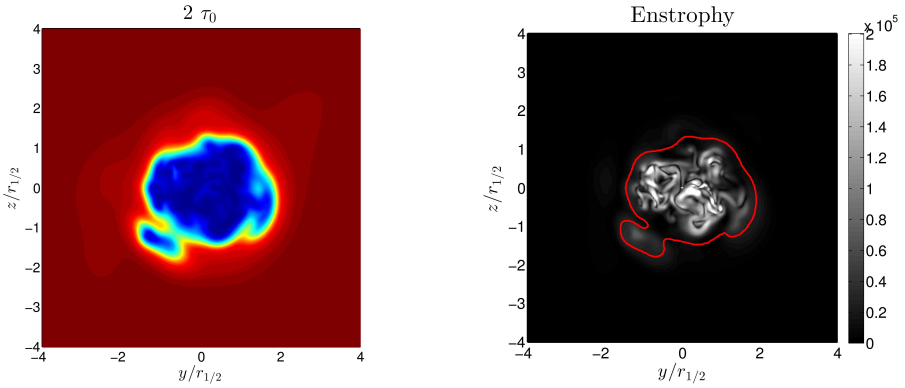

(a) Progress variable contours (b) Enstrophy contours

Figure 6.3: a) Progress variable contours and b) Enstrophy (ω^2) contours.

One does not have to perform simulations over the whole domain, to capture the large scale flow effects. These effects can be emulated by including these forcing terms in the governing equations, and can be used in multiple applications.

Appendix A

NGA

All simulations in this study are performed using NGA [6], a finite difference solver with an energy-conserving scheme on a staggered grid, designed to simulate variable density turbulent flows, using the low Mach number Navier-Stokes equations. A detailed description of NGA and the numerical methods are provided by Desjardins *et al.* [6] and by Savard *et al.* [20]. An overview of NGA and its numerical methods were provided in the theses of Phares Carroll [4] and Jason Schlup [21]. Only a brief summary of NGA is given here, for the sake of completion.

A.1 Governing equations

The low Mach number approximation decouples the energy and momentum equations, and as a consequence, the acoustic waves need not be resolved in the simulation. All the flow quantities are perturbed using a small value of M^2, where M is the Mach number. Assuming low Mach number flows, the leading order term for pressure should be constant in space. This leading order term, p_o, is called the thermodynamic pressure and is not present in the momentum equation, as the momentum equation contains only the gradient of pressure. The second largest term, p, of order M^2, appears in the momentum equation, and is called the hydrodynamic pressure. This term is small under the low Mach number approximation, compared to the thermodynamic pressure, and hence neglected in the equation of state. Under this approximation, the conservation equations are given below.

The conservation of mass is given by

$$\frac{\partial \rho}{\partial t} + \nabla \cdot (\rho \boldsymbol{u}) = 0, \tag{A.1}$$

where ρ is the density, and $\boldsymbol{u} = \{u, v, w\}$ is the velocity field. The conservation of linear momentum equation is

$$\frac{\partial}{\partial t}(\rho \boldsymbol{u}) + \nabla \cdot (\rho \boldsymbol{u} \otimes \boldsymbol{u}) + \nabla p - \nabla \cdot \underline{\underline{\boldsymbol{\tau}}} = 0, \tag{A.2}$$

where p is the hydrodynamic pressure field and $\underline{\underline{\boldsymbol{\tau}}}$ is the viscous stress tensor, given by

$$\underline{\underline{\boldsymbol{\tau}}} = \mu \left(\underline{\underline{\nabla \boldsymbol{u}}} + (\underline{\underline{\nabla \boldsymbol{u}}})^T \right) - \frac{2}{3}\mu(\nabla \cdot \boldsymbol{u})\underline{\underline{\boldsymbol{I}}},$$

where μ is the dynamic viscosity of the mixture and $\underline{\underline{\boldsymbol{I}}}$ is the identity tensor. The species transport equation is expressed as

$$\frac{\partial}{\partial t}(\rho Y_i) + \nabla \cdot (\rho \boldsymbol{u} Y_i) + \nabla \cdot \boldsymbol{j}_i - \dot{\omega}_i = 0\,, \tag{A.3}$$

where Y_i, $\dot{\omega}_i$, and $\boldsymbol{j}_i$ are the mass fraction, production rate, and diffusion flux, respectively, of species i. The diffusion flux is calculated as

$$\boldsymbol{j}_i = -\rho D_i \frac{Y_i}{X_i} \nabla X_i - \rho Y_i \boldsymbol{u_c}\,, \tag{A.4}$$

where D_i is the species diffusivity, calculated as $D_i = \alpha / Le_i$, $\alpha = \lambda/(\rho c_p)$ is the thermal diffusivity of the mixture, λ is the thermal conductivity of the mixture, and Le_i is the Lewis number of species i. X_i is the mole fraction of species i, and $\boldsymbol{u_c}$ is the correction velocity to ensure zero net diffusion flux, $\sum_i \boldsymbol{j}_i = 0$ [5]. The conservation of energy is implemented as a transport equation for temperature, T, using the form

$$\frac{\partial}{\partial t}(\rho T) + \nabla \cdot (\rho \boldsymbol{u} T) - \frac{1}{c_p} \nabla \cdot (\lambda \nabla T) - \dot{\omega}_T + \frac{1}{c_p} \sum_i c_{p,i} \boldsymbol{j}_i \cdot \nabla T = 0\,, \tag{A.5}$$

where $c_{p,i}$ is the heat capacity of species i, $c_p = \sum_i Y_i c_{p,i}$ is the heat capacity of the mixture, and $\dot{\omega}_T = -1/c_p \sum_i h_i \dot{\omega}_i$ is the heat source term, where h_i is the specific enthalpy of species, i. The equation of state used to bring closure to this system of equations is given by

$$p_0 = \rho R T \sum_i \frac{Y_i}{W_i} \tag{A.6}$$

where p_0 is the thermodynamic pressure, R is the universal gas constant, and W_i is the molecular weight of species i. Using the low Mach number assumption, the fluctuations in the hydrodynamic pressure field, p, are small compared to the constant thermodynamic pressure, p_0, used in the equation of state.

These equations are solved to obtain the unknown variables - $(\rho, u, v, w, T, Y_i, p, W)$, while the thermodynamic pressure is taken as an input parameter. The hydrodynamic pressure field is calculated using a Poisson solver, to satisfy conservation of mass, whereas the thermodynamic pressure is known at every time instant. The incompressible simulations use constant density, temperature, viscosity, and a uniform medium, with no chemical reactions.

A.2 Numerical methods

NGA is a finite difference solver with a discretely energy-conserving scheme on a staggered grid, designed to simulate variable density low Mach number turbu-

lent flows. A brief summary of the time integration scheme, chemistry, velocity discretization, and scalar transport method used by NGA is included below.

Time integration: The time advancing of the simulation variables is performed using a second order in time, semi-implicit Crank-Nicolson scheme [16]. The time stepping of the scalars and velocity field is staggered, the scalars are advanced from $t^{n+1/2} = t + \Delta t/2$ to $t^{n+3/2}$, and the velocity fields are integrated from t^n to t^{n+1}. At each time step, 4 subiterations are used. At each subiteration, a sequence of operations are performed in a certain order: The scalar field is advanced, the density field is calculated, the velocity field is calculated (without satisfying mass conservation), a pressure Poisson equation is solved to correct the velocity field so that continuity is satisfied, and finally the solution is updated. A detailed description of this time integration scheme is provided by Savard *et al.* [20]

Semi-implicit time integration for chemistry: The chemical source terms in the reacting flow simulations are preconditioned using a semi-implicit treatment of the chemical source terms [20]. The method treats the scalar transport equation with a simple preconditioner, which is a close approximation of the diagonal of the chemical Jacobian matrix. This helps in increasing the time step of the simulations, while keeping the computational cost for chemistry similar to that of an explicit time integration scheme.

Finite rate chemistry: The production rates of the species and enthalpy are calculated using a reduced n–C_7H_{16} combustion model with 35 species and 217 elementary reactions (which counts for forward and backward reactions separately) [1].

Velocity discretization: The velocity fields are calculated at the cell faces in the respective directions, and second order centered finite difference schemes are used for both the continuity and momentum equations. The density is calculated at the cell centers, and the scalar and velocity fields are interpolated using second-order schemes, when needed, to calculate the convective and diffusive terms. Refer to Fig. A.1 for a two-dimensional representation of the staggered grid. This method discretely conserves mass, momentum, and kinetic energy [6].

Scalar transport: The scalar transport for the species mass fraction and temperature is performed using the bounded quadratic upwind biased interpolative

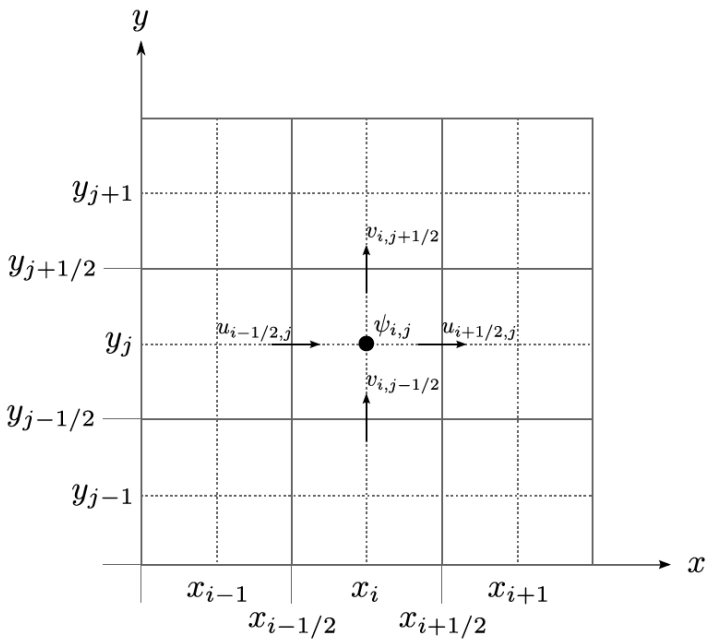

Figure A.1: Two-dimensional representation of the discretization of the computational domain. From Jason Schlup's thesis. [21].

convective scheme (BQUICK) [8]. This method extends the finite volume QUICK scheme [12], by adding a flux correction to ensure that the scalars are within physical bounds. The BQUICK scheme uses QUICK's third order upwind interpolation, to predict the scalar values at an intermediate time step, t^*. At cell locations where the predicted scalar value is out of its physical bounds, a first-order upwind scheme is used instead.

BIBLIOGRAPHY

[1] Genrikh Naumovich Abramovich et al. “The theory of turbulent jets”. In: *Moscow Izdatel Nauka* (1984).

[2] AJ Aspden, MS Day, and JB Bell. “Lewis number effects in distributed flames”. In: *Proc. Combust. Inst.* 33.1 (2011), pp. 1473–1480.

[3] AJ Aspden, MS Day, and JB Bell. “Turbulence–flame interactions in lean premixed hydrogen: transition to the distributed burning regime”. In: *J. Fluid Mech.* 680 (2011), pp. 287–320.

[4] R Balachandran et al. “Experimental investigation of the nonlinear response of turbulent premixed flames to imposed inlet velocity oscillations”. In: *Combustion and Flame* 143.1-2 (2005), pp. 37–55.

[5] RS Barlow et al. “Experiments on the scalar structure of turbulent CO/H2/N2 jet flames”. In: *Combustion and Flame* 120.4 (2000), pp. 549–569.

[6] B Bedat and RK Cheng. “Experimental study of premixed flames in intense isotropic turbulence”. In: *Combustion and Flame* 100.3 (1995), pp. 485–494.

[7] JB Bell et al. “Numerical simulation of a laboratory-scale turbulent V-flame”. In: *Proceedings of the National Academy of Sciences* 102.29 (2005), pp. 10006–10011.

[8] John B Bell et al. “Numerical simulation of a laboratory-scale turbulent slot flame”. In: *Proceedings of the combustion institute* 31.1 (2007), pp. 1299–1307.

[9] Brock Bobbitt, Simon Lapointe, and Guillaume Blanquart. “Vorticity transformation in high Karlovitz number premixed flames”. In: *Phys. Fluids* 28.1 (2016), p. 015101.

[10] BJ Boersma, G Brethouwer, and FTM Nieuwstadt. “A numerical investigation on the effect of the inflow conditions on the self-similar region of a round jet”. In: *Phys. Fluids* 10.4 (1998), pp. 899–909.

[11] M Boger et al. “Direct numerical simulation analysis of flame surface density concept for large eddy simulation of turbulent premixed combustion”. In: *Symposium (International) on Combustion*. Vol. 27. 1. Elsevier. 1998, pp. 917–925.

[12] Guillaume Boudier et al. “Comparison of LES, RANS and experiments in an aeronautical gas turbine combustion chamber”. In: *Proceedings of the Combustion Institute* 31.2 (2007), pp. 3075–3082.

[13] LJS Bradbury. “The structure of a self-preserving turbulent plane jet”. In: *J. Fluid Mech.* 23.1 (1965), pp. 31–64.

[14] Kyle A Brucker et al. “Efficient algorithm for simulating homogeneous turbulent shear flow without remeshing”. In: *Journal of Computational Physics* 225.1 (2007), pp. 20–32.

[15] Paolo Burattini, Robert Anthony Antonia, and L Danaila. “Similarity in the far field of a turbulent round jet”. In: *Phys. Fluids* 17.2 (2005), p. 025101.

[16] P Burattini et al. “PIV and hot wire measurements in the far field of turbulent round jets”. In: *Measurement Science and Technology* 21.12 (2010), p. 125402.

[17] Daniele Carati, Sandip Ghosal, and Parviz Moin. “On the representation of backscatter in dynamic localization models”. In: *Phys. Fluids* 7.3 (1995), pp. 606–616.

[18] Henning Carlsson, Rixin Yu, and Xue-Song Bai. “Direct numerical simulation of lean premixed CH 4/air and H 2/air flames at high Karlovitz numbers”. In: *Int. J. Hydrogen Energy* 39.35 (2014), pp. 20216–20232.

[19] Henning Carlsson, Rixin Yu, and Xue-Song Bai. “Flame structure analysis for categorization of lean premixed CH 4/air and H 2/air flames at high Karlovitz numbers: direct numerical simulation studies”. In: *Proc. Combust. Inst.* 35.2 (2015), pp. 1425–1432.

[20] Phares L Carroll and G Blanquart. “A proposed modification to Lundgren’s physical space velocity forcing method for isotropic turbulence”. In: *Phys. Fluids* 25.10 (2013), p. 105114.

[21] FH Champagne, VG Harris, and S Corrsin. “Experiments on nearly homogeneous turbulent shear flow”. In: *Journal of Fluid Mechanics* 41.1 (1970), pp. 81–139.

[22] FH Champagne, YH Pao, and IJ Wygnanski. “On the two-dimensional mixing region”. In: *J. Fluid Mech.* 74.2 (1976), pp. 209–250.

[23] Jeffrey R Chasnov. “Simulation of the Kolmogorov inertial subrange using an improved subgrid model”. In: *Phys. Fluids A: Fluid Dynamics* 3.1 (1991), pp. 188–200.

[24] Jacqueline H Chen et al. “Terascale direct numerical simulations of turbulent combustion using S3D”. In: *Computational Science & Discovery* 2.1 (2009), p. 015001.

[25] PJ Coelho and N Peters. “Numerical simulation of a mild combustion burner”. In: *Combust. Flame* 124.3 (2001), pp. 503–518.

[26] O Colin et al. “A thickened flame model for large eddy simulations of turbulent premixed combustion”. In: *Physics of fluids* 12.7 (2000), pp. 1843–1863.

[27] Olivier Desjardins et al. “High order conservative finite difference scheme for variable density low Mach number turbulent flows”. In: *J. Comput. Phys.* 227.15 (2008), pp. 7125–7159.

[28] V Eswaran and SB Pope. “An examination of forcing in direct numerical simulations of turbulence”. In: *Computers & Fluids* 16.3 (1988), pp. 257–278.

[29] M Falchi and GP Romano. “Evaluation of the performance of high-speed PIV compared to standard PIV in a turbulent jet”. In: *Experiments in fluids* 47.3 (2009), pp. 509–526.

[30] C Galletti et al. “Numerical and experimental analysis of NO emissions from a lab-scale burner fed with hydrogen-enriched fuels and operating in MILD combustion”. In: *Int. J. Hydrogen Energy* 34.19 (2009), pp. 8339–8351.

[31] Thomas Gerz, Ulrich Schumann, and SE Elghobashi. “Direct numerical simulation of stratified homogeneous turbulent shear flows”. In: *Journal of Fluid Mechanics* 200 (1989), pp. 563–594.

[32] Sandip Ghosal et al. “A dynamic localization model for large-eddy simulation of turbulent flows”. In: *J. Fluid Mech.* 286 (1995), pp. 229–255.

[33] Ponnuthurai Gokulakrishnan et al. “Ignition of Light Hydrocarbon Mixtures Relevant to Thermal Cracking of Jet Fuels”. In: *54th AIAA Aerospace Sciences Meeting*. 2016, p. 0661.

[34] A Gruber et al. “Turbulent flame–wall interaction: a direct numerical simulation study”. In: *Journal of Fluid Mechanics* 658 (2010), pp. 5–32.

[35] E Gutmark and I Wygnanski. “The planar turbulent jet”. In: *J. Fluid Mech.* 73.3 (1976), pp. 465–495.

[36] Peter E Hamlington, Alexei Y Poludnenko, and Elaine S Oran. “Interactions between turbulence and flames in premixed reacting flows”. In: *Phys. Fluids* 23.12 (2011), p. 125111.

[37] Evatt R Hawkes et al. “Scalar mixing in direct numerical simulations of temporally evolving plane jet flames with skeletal CO/H2 kinetics”. In: *Proceedings of the combustion institute* 31.1 (2007), pp. 1633–1640.

[38] Jackson R Herring and Robert M Kerr. “Comparison of direct numerical simulations with predictions of two-point closures for isotropic turbulence convecting a passive scalar”. In: *Journal of Fluid Mechanics* 118 (1982), pp. 205–219.

[39] AT Holley et al. “Ignition and extinction of non-premixed flames of single-component liquid hydrocarbons, jet fuels, and their surrogates”. In: *Proceedings of the Combustion Institute* 31.1 (2007), pp. 1205–1213.

[40] Hussein J Hussein, Steven P Capp, and William K George. “Velocity measurements in a high-Reynolds-number, momentum-conserving, axisymmetric, turbulent jet”. In: *J. Fluid Mech.* 258 (1994), pp. 31–75.

[41] Juan C Isaza and Lance R Collins. "On the asymptotic behaviour of large-scale turbulence in homogeneous shear flow". In: *Journal of Fluid Mechanics* 637 (2009), pp. 213–239.

[42] Chungsheng Ji, Yang L Wang, and Fokion N Egolfopoulos. "Flame studies of conventional and alternative jet fuels". In: *Journal of Propulsion and Power* 27.4 (2011), pp. 856–863.

[43] Yasuhiro Kamotani and Isaac Greber. "Experiments on a turbulent jet in a cross flow". In: *AIAA journal* 10.11 (1972), pp. 1425–1429.

[44] Shahram Karami et al. "Mechanisms of flame stabilisation at low lifted height in a turbulent lifted slot-jet flame". In: *Journal of Fluid Mechanics* 777 (2015), pp. 633–689.

[45] M Houssem Kasbaoui et al. "An algorithm for solving the Navier–Stokes equations with shear-periodic boundary conditions and its application to homogeneously sheared turbulence". In: *Journal of Fluid Mechanics* 833 (2017), pp. 687–716.

[46] Hideaki Kobayashi et al. "Burning velocity of turbulent premixed flames in a high-pressure environment". In: *Symposium (international) on combustion*. Vol. 26. 1. Elsevier. 1996, pp. 389–396.

[47] Simon Lapointe and Guillaume Blanquart. "A priori filtered chemical source term modeling for LES of high Karlovitz number premixed flames". In: *Combustion and Flame* 176 (2017), pp. 500–510.

[48] Simon Lapointe and Guillaume Blanquart. "Fuel and chemistry effects in high Karlovitz premixed turbulent flames". In: *Combust. Flame* 167 (2016), pp. 294–307.

[49] Simon Lapointe, Bruno Savard, and Guillaume Blanquart. "Differential diffusion effects, distributed burning, and local extinctions in high Karlovitz premixed flames". In: *Combust. Flame* 162.9 (2015), pp. 3341–3355.

[50] Moon Joo Lee, John Kim, and Parviz Moin. "Structure of turbulence at high shear rate". In: *Journal of Fluid Mechanics* 216 (1990), pp. 561–583.

[51] AN Lipatnikov and J Chomiak. "Turbulent flame speed and thickness: phenomenology, evaluation, and application in multi-dimensional simulations". In: *Progress in energy and combustion science* 28.1 (2002), pp. 1–74.

[52] JL Lumley. "Similarity and the turbulent energy spectrum". In: *The physics of fluids* 10.4 (1967), pp. 855–858.

[53] TS Lundgren. *Linearly Forces Isotropic Turbulence*. Tech. rep. Minnesota Univ., Minneapolis, 2003.

[54] Kevin M Lyons. "Toward an understanding of the stabilization mechanisms of lifted turbulent jet flames: experiments". In: *Progress in Energy and Combustion Science* 33.2 (2007), pp. 211–231.

[55] Wolfgang Meier et al. “Raman/Rayleigh/LIF measurements in a turbulent CH4/H2/N2 jet diffusion flame: experimental techniques and turbulence–chemistry interaction”. In: *Combustion and Flame* 123.3 (2000), pp. 326–343.

[56] MG Mungal and PE Dimotakis. “Mixing and combustion with low heat release in a turbulent shear layer”. In: *Journal of Fluid Mechanics* 148 (1984), pp. 349–382.

[57] Steven A Orszag and GS Patterson Jr. “Numerical simulation of three-dimensional homogeneous isotropic turbulence”. In: *Physical Review Letters* 28.2 (1972), p. 76.

[58] D Oster and I Wygnanski. “The forced mixing layer between parallel streams”. In: *J. Fluid Mech.* 123 (1982), pp. 91–130.

[59] N. R. Panchapakesan and J. L. Lumley. “Turbulence measurements in axisymmetric jets of air and helium. Part 1. Air jet”. In: *J. Fluid Mech.* 296 (1993), pp. 197–223.

[60] Thierry Passot and Annick Pouquet. “Numerical simulation of compressible homogeneous flows in the turbulent regime”. In: *J. Fluid Mech.* 181 (1987), pp. 441–466.

[61] Norbert Peters and Forman A Williams. “Liftoff characteristics of turbulent jet diffusion flames”. In: *AIAA journal* 21.3 (1983), pp. 423–429.

[62] Charles D Pierce and Parviz Moin. “Progress-variable approach for large-eddy simulation of non-premixed turbulent combustion”. In: *Journal of fluid Mechanics* 504 (2004), pp. 73–97.

[63] Heinz Pitsch and H Steiner. “Large-eddy simulation of a turbulent piloted methane/air diffusion flame (Sandia flame D)”. In: *Physics of fluids* 12.10 (2000), pp. 2541–2554.

[64] Alexei Y Poludnenko and Elaine S Oran. “The interaction of high-speed turbulence with flames: Global properties and internal flame structure”. In: *Combust. Flame* 157.5 (2010), pp. 995–1011.

[65] SB Pope. “Calculations of a plane turbulent jet”. In: *AIAA J* 22.7 (1984), pp. 896–904.

[66] Stephen B Pope. *Turbulent flows*. 2001.

[67] Kyupaeck Jeff Rah, Chandru Dhandapani, and Guillaume Blanquart. “Derivation of a realistic forcing term to reproduce the turbulent characteristics of round jets on the centerline”. In: *Physical Review Fluids* 3.8 (2018), p. 084606.

[68] Robert Sugden Rogallo. “Numerical experiments in homogeneous turbulence”. In: *NASA Technical Memorandum 81315* (1981).

[69] Michael M Rogers and Parviz Moin. “The structure of the vorticity field in homogeneous turbulent flows”. In: *Journal of Fluid Mechanics* 176 (1987), pp. 33–66.

[70] Michael M Rogers and Robert D Moser. “Direct simulation of a self-similar turbulent mixing layer”. In: *Phys. Fluids* 6.2 (1994), pp. 903–923.

[71] MM Rogers, P Moin, and WC Reynolds. *The structure and modeling of the hydrodynamic and passive scalar fields in homogeneous turbulent shear flow. Department of Mechanical Engineering TF-25*. 1986.

[72] Carlos Rosales and Charles Meneveau. “Linear forcing in numerical simulations of isotropic turbulence: Physical space implementations and convergence properties”. In: *Phys. Fluids* 17.9 (2005), p. 095106.

[73] CJ Rutland and A Trouvé. “Direct simulations of premixed turbulent flames with nonunity Lewis numbers”. In: *Combustion and Flame* 94.1-2 (1993), pp. 41–57.

[74] Ramanan Sankaran et al. “Structure of a spatially developing turbulent lean methane–air Bunsen flame”. In: *Proc. Combust. Inst.* 31.1 (2007), pp. 1291–1298.

[75] Bruno Savard and Guillaume Blanquart. “Broken reaction zone and differential diffusion effects in high Karlovitz n-C 7 H 16 premixed turbulent flames”. In: *Combust. Flame* 162.5 (2015), pp. 2020–2033.

[76] Bruno Savard, Brock Bobbitt, and Guillaume Blanquart. “Structure of a high Karlovitz n-C 7 H 16 premixed turbulent flame”. In: *Proc. Combust. Inst.* 35.2 (2015), pp. 1377–1384.

[77] Von H Schlichting. “Laminar beam propagation”. In: *ZAMM-Journal of Applied Mathematics and Mechanics* 13.4 (1933), pp. 260–263.

[78] Jason Schlup and Guillaume Blanquart. “A reduced thermal diffusion model for H and H2”. In: *Combustion and Flame* 191 (2018), pp. 1–8.

[79] Jason Schlup and Guillaume Blanquart. “Validation of a mixture-averaged thermal diffusion model for premixed lean hydrogen flames”. In: *Combustion Theory and Modelling* 22.2 (2018), pp. 264–290.

[80] Jörg Schumacher and Bruno Eckhardt. “On statistically stationary homogeneous shear turbulence”. In: *EPL (Europhysics Letters)* 52.6 (2000), p. 627.

[81] Atsushi Sekimoto, Siwei Dong, and Javier Jiménez. “Direct numerical simulation of statistically stationary and homogeneous shear turbulence and its relation to other shear flows”. In: *Physics of Fluids* 28.3 (2016), p. 035101.

[82] Laurent Selle et al. “Compressible large eddy simulation of turbulent combustion in complex geometry on unstructured meshes”. In: *Combustion and Flame* 137.4 (2004), pp. 489–505.

[83] Jiankun Shao et al. “A shock tube study of jet fuel pyrolysis and ignition at elevated pressures and temperatures”. In: *Fuel* 226 (2018), pp. 338–344.

[84] Thomas M Smith and Suresh Menon. “The structure of premixed flames in a spatially evolving turbulent flow”. In: *Combust. Sci. Technol.* 119.1-6 (1996), pp. 77–106.

[85] Jennifer Smolke et al. “Experimental and numerical studies of fuel and hydrodynamic effects on piloted turbulent premixed jet flames”. In: *Proc. Combust. Inst.* 36.2 (2017), pp. 1877–1884.

[86] SA Stanley, S Sarkar, and JP Mellado. “A study of the flow-field evolution and mixing in a planar turbulent jet using direct numerical simulation”. In: *J. Fluid Mech.* 450 (2002), pp. 377–407.

[87] Luc Vervisch et al. “Three facets of turbulent combustion modelling: DNS of premixed V-flame, LES of lifted nonpremixed flame and RANS of jet-flame”. In: *Journal of turbulence* 5.4 (2004), pp. 1–8.

[88] Zhihua Wang et al. “Direct numerical simulation of subsonic round turbulent jet”. In: *Flow, turbulence and combustion* 84.4 (2010), pp. 669–686.

[89] I Wygnanski and Heinrich E Fiedler. “The two-dimensional mixing region”. In: *J. Fluid Mech.* 41.2 (1970), pp. 327–361.

[90] I Wygnanski and Ho Fiedler. “Some measurements in the self-preserving jet”. In: *J. Fluid Mech.* 38.3 (1969), pp. 577–612.

[91] Rui Xu et al. “A physics-based approach to modeling real-fuel combustion chemistry–II. Reaction kinetic models of jet and rocket fuels”. In: *Combustion and Flame* 193 (2018), pp. 520–537.

[92] Chun Sang Yoo, Ramanan Sankaran, and JH Chen. “Three-dimensional direct numerical simulation of a turbulent lifted hydrogen jet flame in heated coflow: flame stabilization and structure”. In: *Journal of Fluid Mechanics* 640 (2009), pp. 453–481.